THE HONG KONG
POLYTECHNIC UNIVERSITY
香港理工大學
Pao Yue-kong Library
包玉剛圖書館

Copyright Undertaking

This thesis is protected by copyright, with all rights reserved.

By reading and using the thesis, the reader understands and agrees to the following terms:

1. The reader will abide by the rules and legal ordinances governing copyright regarding the use of the thesis.
2. The reader will use the thesis for the purpose of research or private study only and not for distribution or further reproduction or any other purpose.
3. The reader agrees to indemnify and hold the University harmless from and against any loss, damage, cost, liability or expenses arising from copyright infringement or unauthorized usage.

IMPORTANT

If you have reasons to believe that any materials in this thesis are deemed not suitable to be distributed in this form, or a copyright owner having difficulty with the material being included in our database, please contact lbsys@polyu.edu.hk providing details. The Library will look into your claim and consider taking remedial action upon receipt of the written requests.

Pao Yue-kong Library, The Hong Kong Polytechnic University, Hung Hom, Kowloon, Hong Kong

http://www.lib.polyu.edu.hk

TOWARDS RECHARGEABLE CALCIUM-ION BATTERIES: INSERTION CHEMISTRY AND ELECTRODE STABILITY

ZHOU RUI

PhD

The Hong Kong Polytechnic University

2024

The Hong Kong Polytechnic University

Department of Applied Physics

Towards rechargeable calcium-ion batteries: insertion chemistry and electrode stability

ZHOU Rui

A thesis submitted in partial fulfilment of the requirements for
the degree of Doctor of Philosophy

August 2023

CERTIFICATE OF ORIGINALITY

I hereby declare that this thesis is my own work and that, to the best of my knowledge and belief, it reproduces no material previously published or written, nor material that has been accepted for the award of any other degree or diploma, except where due acknowledgement has been made in the text.

(Signed)

ZHOU Rui (Name of student)

Abstract

Calcium-ion batteries (CIBs) have been considered promising multivalent ion battery systems due to the natural abundance and low redox potential of calcium (Ca). However, their practical realization is largely hampered by the lack of reliable electrode materials. The large radius and high charge density of Ca^{2+} commonly lead to sluggish diffusion kinetics, resulting in an inferior capacity and rate capability. This thesis aims to design high-performance electrodes and probe their reaction mechanisms for rechargeable CIBs.

We first explore selenium as a new conversion-type electrode for both non-aqueous and aqueous CIBs. It provides a high specific capacity of 476 mAh g^{-1} with an average voltage of 2.2 V vs. Ca/Ca^{2+}, offering a higher energy density than other reported cathode materials. The spectroscopy analysis and density functional theory calculations suggest multi-step conversion processes involving $CaSe_4$ and Ca_2Se_5 polyselenides intermediates before reaching the final CaSe phase, exhibiting a distinct reaction pathway from those in other metal-Se batteries.

Besides the inorganic Se electrode, the organic compound is explored due to its advantages of structure flexibility and unique ion coordination mechanism. Specifically, polytriphenylamine (PTPAn) material is developed as an ultra-stable and high-rate cathode, residing in the reversible combination/release of anions with a C-N bond. As a result, the graphite|PTPAn full cell exhibits superior stability of over 2000 cycles with extremely fast kinetics up to 50 C rate in non-aqueous electrolyte. Interestingly, PTPAn is also highly compatible with aqueous electrolytes, allowing the construction of an all-organic aqueous calcium-based dual ion battery by coupling with a 3,4,9,10-perylenetetracarboxylic-diimide (PTCDI) anode.

We further investigate organic PTCDI anode's reaction mechanisms since PTCDI as a counter electrode shows a distinct electrochemical behavior in non-aqueous and aqueous electrolytes. It delivers an attractive specific capacity of 113 mAh g^{-1} at 0.2 A g^{-1} and capacity retention of 92% at 2 A g^{-1} in aqueous electrolyte, compared to 68 mAh g^{-1} and 74% in non-aqueous counterpart. The combined spectroscopic analysis and theoretical simulations reveal that such difference originates from the synergistic proton and Ca^{2+} insertion in the former. The co-storage strategy is also observed in the Mg-ion system, thus allowing the stable cycling of 1.1 V-class aqueous Mg-/Ca-ion full cells for over 2000 cycles.

List of publications

$^{\#}$Equal contribution first author; *Corresponding author.

1. **Rui Zhou**, Hong Tan, Yao Gao, Zhen Hou, Xiaoqiong Du, Biao Zhang*, Constructing resilient solid electrolyte interphases on carbon nanofiber film for advanced potassium metal anodes, Carbon, 2022, 186, 141-149.

2. **Rui Zhou**$^{\#}$, Zhen Hou$^{\#}$, Qun Liu, Xiaoqiong Du, Jiaqiang Huang*, Biao Zhang*, Unlocking the reversible selenium electrode for non-aqueous and aqueous calcium-ion batteries, Advanced Functional Materials, 2022, 32, 2200929.

3. **Rui Zhou**$^{\#}$, Zhen Hou$^{\#}$, Ke Fan$^{\#}$, Ching Kit Wun, Qun Liu, Tsz Woon Benedict Lo, Haitao Huang*, Biao Zhang*, An advanced organic cathode for non-aqueous and aqueous calcium-based dual ion batteries, Journal of Power Sources, 2023, 569, 232995.

4. **Rui Zhou**$^{\#}$, Ke Fan$^{\#}$, Zhen Hou, Qun Liu, Haitao Huang*, Biao Zhang*, Synergistic proton and Mg^{2+}/Ca^{2+} insertion boosting aqueous divalent ion batteries, Energy Storage Materials, 2023, 63, 103012.

5. Zhen. Hou, **Rui Zhou**, Yunduo Yao, Zhiwen Min, Ziheng Lu, Ye Zhu, Jean-Marie Tarascon, Biao Zhang*, Correlation between electrolyte chemistry and solid electrolyte interphase for reversible Ca metal anodes, Angewandte Chemie International Edition, 2022, 61, e202214796.

6. Zhen Hou, **Rui Zhou**, Zhiwen Min, Ziheng Lu, Biao Zhang, Realizing wide-temperature reversible Ca metal anodes through a Ca^{2+}-conducting artificial layer, ACS Energy Letters, 2022, 8, 274-279.

7. Hong Tan, **Rui Zhou**, and Biao Zhang*. Understanding potassium ion storage

mechanism in pitch-derived soft carbon and the consequence on cyclic stability. Journal of Power Sources, 2021, 506, 230179.

8. Yao Gao, Zhen Hou, **Rui Zhou**, Danni Wang, Xuyun Guo, Ye Zhu, Biao Zhang*, Critical roles of mechanical properties of solid electrolyte interphase for potassium metal anodes, Advanced Functional Materials, 2022, 32, 2112399.

9. Zhen Hou, Yao Gao, **Rui Zhou**, Biao Zhang*, Unraveling the rate-dependent stability of metal anodes and its implication in designing cycling protocol. Advanced Functional Materials, 2022, 32, 2107584.

10. Qun Liu, Zhenlu Yu, **Rui Zhou**, Biao Zhang*, A semi-liquid electrode toward stable Zn powder anode, Advanced Functional Materials, 2023, 33, 2210290.

11. Hong Tan, Xiaoqiong Du, **Rui Zhou**, Zhen Hou, Biao Zhang*, Rational design of microstructure and interphase enables high-capacity and long-life carbon anodes for potassium ion batteries, Carbon, 176, 2021, 383-389.

12. Qun Liu, Yu Wang, Xiaodan Hong, **Rui Zhou**, Zhen Hou, Biao Zhang*, Elastomer-alginate interface for high-power and high-energy Zn metal anodes, Advanced Energy Materials, 2022, 12, 2200318.

Acknowledgments

Upon this thesis is finished, I want to sincerely thank everyone who has supported me throughout my Ph.D. study.

Firstly, I would like to convey my profound thanks to my supervisor Prof. Biao Zhang. He provides me with invaluable guidance, in-depth discussion, helpful suggestions, continuing support and encouragement. He not only teaches me the right way to search for and conduct a research project, but also helps me to become a better person. I also want to thank my co-supervisor Prof. Shu Ping Lau for his helping.

Besides, I would like to thank Dr. Jiaqiang Huang and Dr. Ke Fan for their contribution in theoretical simulation.

I also would like to give my heartfelt gratitude to my colleagues, Dr. Yao, Gao, Dr. Hong Tan, Dr. Xiaoqiong, Du, Dr. Zhijie Wang, Mr. Qun Liu, Ms. Danni Wang, Ms. Zhenlu Yu, Ms. Jie Shi for their help. Especially thanks to my best friends Dr. Zhen Hou, Ms. Fengjia Xie and Ms. Chenhao Wang for their accompany, support and help.

In addition, I want to thank all the technicians in the Department of Applied Physics and UMF for their help on the experiments.

Lastly, I am very appreciative of my family, my parents, grandparents, and brother for their constant love, understanding and support.

ZHOU Rui
The Hong Kong Polytechnic University
2023 August

Table of Contents

List of figures

List of tables

Chapter 1. Introduction

This chapter summarizes the advantages of CIBs and provides a brief discussion of the anodes, cathodes, and electrolytes for non-aqueous and aqueous CIBs.

1.1 Calcium-ion batteries

The increasing energy crisis and environmental pollution worldwide make it essential to develop sustainable energy sources like solar and wind power. However, their wide-scale application is largely hindered by their intermittent and uneven-distributed nature. Efficient and accessible energy storage systems (ESSs) are thought to be promising solutions to stabilize the power supply from renewable energies. Among various ESSs, lithium-ion batteries (LIBs) are emerged as the dominate technology in the market and are extensively utilized in portable electronics, aerospace, electric vehicles and other fields. Nonetheless, the energy density of LIBs is now reaching its inherent limit.[1-4] In addition, lithium, nickel and cobalt, which are essential components of LIBs, also face problems like insufficient reserves and high costs. These issues have prompted the research shift towards new advanced ESS based on earth-abundant metals.

Multivalent metal-ion batteries (Zn^{2+}, Mg^{2+}, Ca^{2+} and Al^{3+}) have drawn rising interest because of the coupled or tripled electron transfer with one ion stored, resulting in the increased energy density.[5-8] Among these multivalent metal-ions, Ca possesses the lowest redox potential (-2.87 V vs. the standard hydrogen electrode (SHE)), potentially leads to higher energy density of full cell (Figure 1.1a).[9, 10] Besides, calcium ranks fifth in terms of reserves in the Earth's crust (4.2%), making it a promising and reliable battery system.[7, 11, 12]

In typical CIBs, calcium ions transfer between the cathode and anode to achieve energy storage and release (Figure 1.1b). The development of CIBs suffers from several long-standing obstacles: i) In common organic electrolyte systems, passivated solid electrolyte interfaces (SEIs) formed on Ca metal anode, leading to irreversible Ca metal plating/stripping, which blocks the application of high-capacity Ca metal anodes.[11, 13, 14] ii) Turning to cathode aspect, most materials suffer from slow Ca^{2+} migration and severe structural distortion during insertion/extraction owing to the Ca^{2+}'s divalent characteristic and large ionic radius.[7, 12] This causes poor charge/discharge capability and capacity retention.

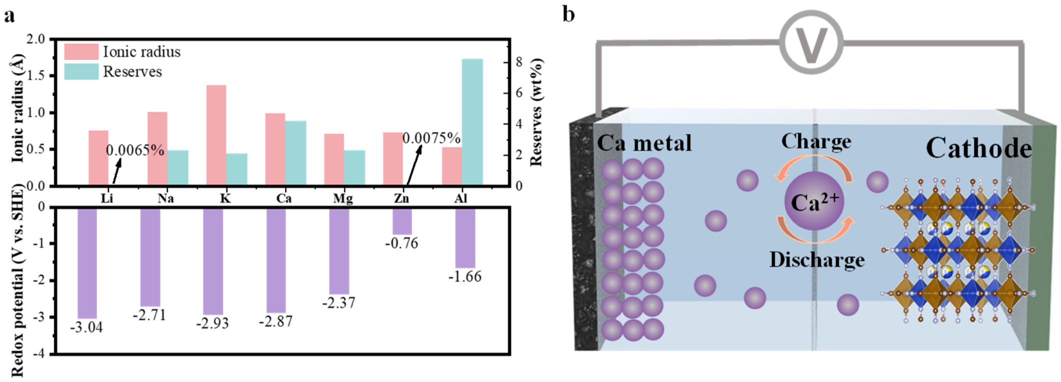

Figure 1.1 a) The comparison of metal ions in terms of ionic radius, oxidation-reduction potential, and crustal reserves. b) A schematic diagram of a CIB.

1.2 Electrolytes for non-aqueous CIBs

The solvation structures and ion interactions in electrolytes show significant influence on the interphase formation and cation migration, which mainly determines the deposition/stripping behavior of Ca metal anode. Thus, optimization of electrolyte composition is effective in achieving reversible Ca metal anodes. There are many commercially available salts for non-aqueous CIBs, such as calcium bis(trifluoromethanesulfonyl)imide ($Ca(TFSI)_2$), calcium tetrafluoroborate ($Ca(BF_4)_2$), calcium borohydride ($Ca(BH_4)_2$), calcium perchlorate ($Ca(ClO_4)_2$) and calcium bis(fluorosulfonyl)imide ($Ca(FSI)_2$). Among them, only $Ca(BH_4)_2$-based electrolyte can achieve reversible electrodeposition of Ca metal at room temperature.[15] Nevertheless, the construction of high-voltage full cells was hampered by the limited electrochemical stability window (ESW) (< 3 V). Therefore, extensive efforts have been conducted on the design of new salts and regulation of electrolyte/anode interphases. Because the efforts on electrolytes mainly focus on Ca metal anode, we will systematically review these progresses in Section 1.3.1.

1.3 Anodes for non-aqueous CIBs

There are a variety of anodes for CIBs, including Ca metal anodes, alloys, intercalation anodes and other counterparts.

1.3.1 Calcium metal anodes

Among all anodes, calcium metal serves as the most ideal one because of its large capacity of 1337 mAh g^{-1} and the lowest operating voltage, attracting the growing research interest.[14, 16, 17] However, reversible Ca deposition/stripping has been proved challenging because of the formation of Ca^{2+}-insulating SEIs in conventional electrolytes. Many attempts to regulate electrolyte formulations and SEIs chemistry have been conducted to resolve this issue.[16, 18] In 2016, Palacín's group demonstrated a reversible Ca metal anode at 75-100 ^{o}C using 0.45 M $Ca(BF_4)_2$-ethylene carbonate (EC)/propylene carbonate (PC) electrolyte for the first time, whereas the $Ca(ClO_4)_2$ and

$Ca(TFSI)_2$ ones show poor reversibility (Figure 1.2a).[19] The reason is the formation of Ca^{2+}-conductive boron SEI for the former. However, its practical implementation is hampered by the high operating temperature concerns with high cost and severe side reactions.

Encouraged by the success of $Mg(BH_4)_2$-THF electrolyte in Mg metal batteries, $Ca(BH_4)_2$-based one has been employed to investigate the deposition behavior of Ca metal anode.[15] It achieved a Coulombic efficiency (CE) of 94.8% at a current density of 1 mA cm^{-2} for 1 h under room temperature (Figure 1.2b). Although it made a significant stride for Ca metal anodes, the relatively narrow ESW of this electrolyte (~3 V) restricts the selection of high-voltage cathodes. To further improve the anodic stability, a new boron-based $Ca[B(hfip)_4]_2$ salt was synthesized by two groups simultaneously (Figure 1.2c).[20, 21] In 1,2-dimethoxyethane (DME) solvent, it provided high CE (~92%) for over 35 cycles (Figure 1.2e). More importantly, this electrolyte delivered an outstanding stability of over 4.5 V vs. Ca/Ca^{2+}, allowing the examination of high-voltage cathodes.

To enhance the reversibility of $Ca[B(hfip)_4]_2$ electrolyte, many approaches have been reported. For example, Bu_4NCl additive is introduced due to its positive effect on the diffusion coefficient and formation of a chloride-based sacrificial interphase in Mg metal anode, although the precise role in Ca metal anode needs to be further investigated (Figure 1.2g).[21] Besides, the current collectors (e.g., Cu, Al, Pt and glassy carbon) and solvents (i.e., THF, DME and diglyme (DGM)) are also optimized.[22] Among them, glassy carbon and DGM show improved CE and cycle stability. Although the above electrolyte systems enable reversible Ca metal anode, the inevitable formation of CaF_2-containing interphase blocks Ca^{2+} diffusion and leads to large polarizations.[23]

To prevent the undesired formation of CaF_2, Orimo's group proposed a fluorine-free salt-$Ca[CB_{11}H_{12}]_2$ salt, which supported a reversible Ca metal anode and provided an exceptional oxidation stability of 4 V (Figure 1.2d, f).[24] Apart from the reduction of CaF_2 species through using fluorine-free salts, high-donor number solvents were used to generate CaF_2-poor/organics-rich SEIs. Such solvents, which possessed a high solvating capability, resulted in solvent-occupied solvation structures and prevented anion decomposition.[25] Therefore, with the help of high-solvating solvents, reversible Ca deposition/stripping was realized using $Ca(TFSI)_2$ salt for the first time at room temperature (Figure 1.2h). However, slightly large polarization in such a system was still observed. An artificial layer on Ca metal was then constructed to solve this problem by the same group.[26]

The ionic liquid-based electrolyte has also been investigated due to their low vapor pressures, outstanding ionic conductivity and superior stability over ester and ether ones.[27] For example, Biria et al. demonstrated a 1-ethyl-3-methylimidazolium trifluoromethanesulfonate-based electrolyte, which achieved a reversible Ca metal anode.[28]

Up to now, only a few electrolytes can achieve reversible Ca metal anodes, focusing on boron-based electrolytes (Table 1.1). In addition, some progress in building artificial SEIs has also been made. However, most of them suffer from complicated synthesis processes or large polarization, impeding the application of Ca metal anode in CIBs.

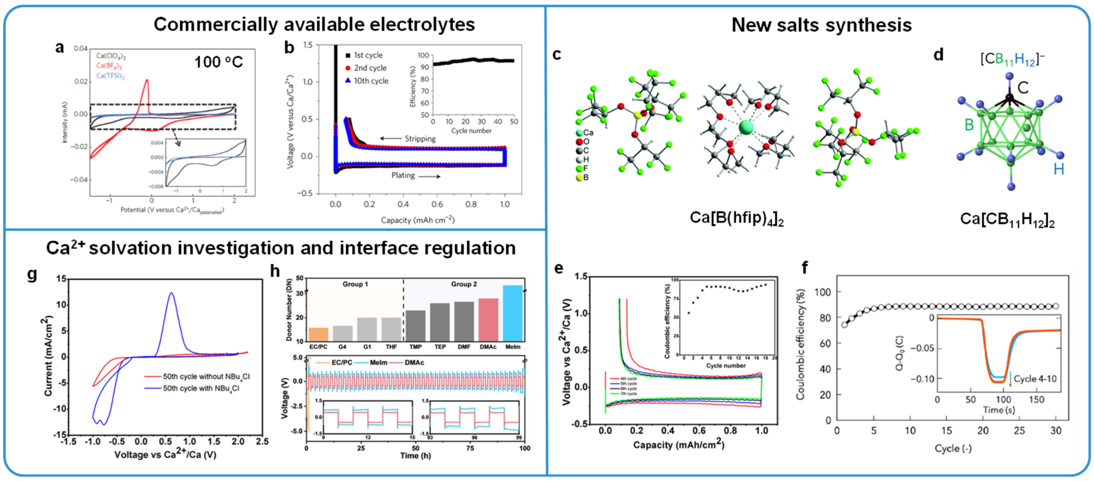

Figure 1.2 a) Cyclic voltammograms (CV) curves of Cu|Ca cells in EC/PC-based electrolytes at 100 °C.[19] b) Voltage profiles at 1 mA cm^{-2} of a three-electrode system in 1.5 M $Ca(BH_4)_2$-THF where Au as working electrode, two Ca metal as the counter and reference electrodes, respectively.[15] c) Structure of $Ca[B(hfip)_4]_2·4DME$ salt.[20] d) Structure of $[CB_{11}H_{12}]^-$ anion.[24] e) Galvanostatic deposition and stripping of a Au|Ca half-battery in 0.5 M $Ca[B(hfip)_4]_2$ electrolyte with a rate of 0.2 mA·cm^{-2} for 5 h.[21] f) CEs of Au|Ca cell in 0.5 M $Ca[CB_{11}H_{12}]_2$-DME/THF electrolyte.[24] g) CV curves in 0.5 M $Ca[B(hfip)_4]_2$ electrolyte with (blue) and without (red) Bu4NCl additive.[21] h) Donor number of different solvents and cyclic performance of Ca|Ca system in various $Ca(TFSI)_2$-based electrolytes.[25]

Table 1.1 The performance comparison of reported Ca metal anodes.

Anode	Electrolyte	Polarization (mV)/current density (mA cm^{-2})	Anodic stability (V vs. Ca/Ca^{2+})	CE (%)	Cycle life (cycles)	Reference
Ca metal	$Ca(BF_4)_2$-EC/PC	100 (obtained by CV)	3.5(Al)	/	30	29
	$Ca(BH_4)_2$-THF	~100/1	3(Au)	94.8	50	15
	$Ca(BH_4)_2$+$LiBH_4$-THF	200/1	/	99.1	200	16
	$Ca[B(hfip)_4]_2$-DME	200/0.2	3.9 (Pt) 4.5 (Al)	80	22	20
	$Ca[B(hfip)_4]_2$-DME	480/0.2	4.1 (Al) 3.8 (Au)	92-95	35	21
	$Ca[CB_{11}H_{12}]_2$-DME/THF	300 (obtained by CV)	4 (Au)	88	35	24
	$Ca(TFSI)_2$-DMAc (with artificial layer)	250/0.02	/	/	350	26

1.3.2 Alloy anodes

Alloy anodes, which are extensively adopted in alkali metal ion batteries, exhibit great potential for CIBs due to their high theoretical capacity at low alloying/dealloying voltage. Ponrouch et al. explored the alloying process between Ca and Si by density functional theory (DFT) calculation, forming Ca_xSi ($0.5 \leqslant x \leqslant 2$) at about 0.37 V vs. Ca/Ca^{2+}. In addition, the decalciation of $CaSi_2$ was achieved at 100 ^{o}C, but the large voltage hysteresis up to 2.3 V limited the capacity (Figure 1.3a).[30] Compared to the poor reversibility of Si, Sn seemed to be more promising for CIBs. Yao et al. revealed the electrochemical calciation pathway of Sn and the correlation between the reaction driving force and Ca content using DFT simulations. Formation voltages of various intermediate phases containing $CaSn_3$, CaSn, Ca_7Sn_6, $Ca_{31}Sn_{20}$, $Ca_{36}Sn_{23}$ and Ca_2Sn were determined by the Sn-Ca convex hull (Figure 1.3b).[31] An early experimental attempt was made by Tang's group in 2018, a Sn|graphite dual ion battery was constructed in $Ca(PF_6)_2$-based electrolyte. XRD patterns confirmed the reversible calciation/decalciation of Sn and generation of Ca_7Sn_6 product (Figure 1.3c).[32] Soon after, a calcium-ion hybrid energy storage device consisting of Sn anode and activated carbon (AC) cathode was also demonstrated.[33] Recently, Zhao's group prepared a Ca_xSn alloy by solid-phase reaction at high temperatures.[34] A CIB was achieved by combining with an organic polymer cathode (Figure 1.3d, e). However, half-cell test has not been conducted in the above reports, leaving the working potential and capacity of Sn anode unclear.

1.3.3 Intercalation anodes

Graphite is a typical intercalation anode in commercial LIBs owing to its low working voltage, low cost and superior chemical stability. In 2005, Lagrange et al. for the first time synthesized the first stage calcium graphite intercalation compound (GIC) using a pyrographite and Li-Ca alloy under high temperature.[35] The as prepared CaC_6 showed a unique rhombohedral structure, while other MC_6 compounds were hexagonal. Ca GIC was also obtained by a mild one-pot method using Ca metal and graphite under Ar atmosphere.[36] Park et al. demonstrated reversible co-intercalation of Ca^{2+} with solvent into graphite in dimethylacetamide (DMAc) electrolyte to form a $[Ca\text{-}(DMAc)_4]C_{50}$ ternary GIC (Figure 1.3f).[37] ACN, diethylene glycol dimethyl ether (DEGDME), THF and ethylene carbonate/dimethyl carbonate (EC/DMC)-based electrolytes were also employed to test the Ca^{2+} intercalation behavior. However, graphite delivered negligible capacities in these electrolytes, revealing that the Ca^{2+} intercalation highly depends on the solvent's properties. Various spectroscopic analysis revealed the co-intercalation structure, where four DMAc molecules are coupled with one Ca^{2+} (Figure 1.3g). Benefiting from the co-intercalation mechanism, graphite provided a specific capacity with a cycle life of 200 cycles. However, poor anodic stability of DMAc solvent hindered the construction of high-voltage CIBs.

Another simultaneous report demonstrated that the Ca^{2+}-tetraglyme ($Ca\text{-}G_4$) can co-intercalate into graphite and form a ternary intercalation compound.[38] Mechanistic study suggested a stage IV→III→II intercalation pathway, resulting in a $Ca\text{-}G_4{\cdot}C_{72}$ final compound with a 210% volume change (Figure 1.3h). Inspired by this work, Pyo's group proposed a Ca^{2+}-based dual-carbon battery in a $Ca(TFSI)_2\text{-}G_4$ in $Pyr_{14}TFSI$ ionic liquid electrolyte, where the MCMB anode accommodated solvated Ca^{2+} and KS6L cathode stored anions.[39] Similarly, graphene has been suggested to be a promising material for Ca^{2+} storage by DFT simulations.[40]

Despite the successful demonstration of Ca^{2+}-specific solvents co-storage into graphite anode, there still exist some basic issues. First, the large radius of solvated Ca^{2+} limits the intercalation of the graphite layer, leading to unsatisfactory specific capacities. It also brings about large volume expansion/shrink during discharge/charge. More perplexingly, it is still unclear what properties of solvents are key factors in the achievement of Ca^{2+} intercalation. The underlying mechanism should be further investigated to develop more suitable electrolytes for achieving the high-capacity Ca^{2+} storage in graphite.

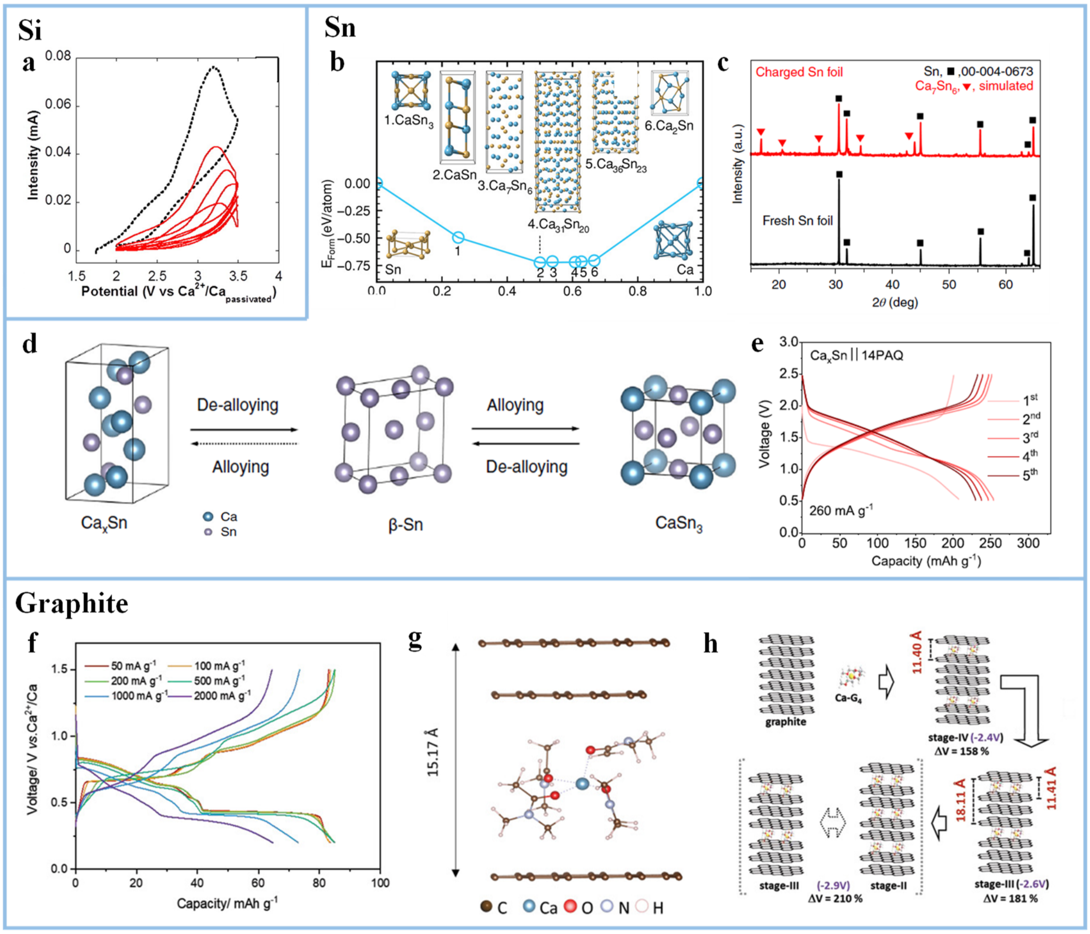

Figure 1.3 a) CV curves of $CaSi_2$ under 0.05 mV s^{-1} at 100 °C.[30] b) Sn-Ca convex hull with all predicted phases. Inset: structures of all intermediate compounds.[31] c) XRD spectra of Sn anode before and after charging.[32] d) The structure transformation of Ca_xSn anode during charge/discharge.[34] e) Voltage profiles of Ca_xSn|1,4-polyanthraquinone full cell at 0.26 A g^{-1}.[34] f) Galvanostatic charge-discharge (GCD) curves of graphite anode at different current densities in $Ca(BH_4)_2$-DMAc electrolyte.[37] g) The Ca^{2+}-DMAc intercalation structure in graphite.[37] h) The Ca^{2+}-G_4 co-intercalation process with different stages.[38]

1.4 Cathodes for non-aqueous CIBs

Developing advanced cathodes with high voltage, large theoretical capacity and superior electrochemical stability is a crucial task. The intercalation of equivalent amount of Ca ions as Li ions into the cathode would lead to doubled capacity due to the divalent nature of Ca ions. However, this property also causes lower diffusion kinetics of Ca^{2+} than Li^+. In addition, the infeasibility of Ca metal anode in common electrolytes makes it challenging to serve as counter electrode to examine the electrochemical activity of cathodes. This problem would be partially resolved by using an AC or Ag/Ag^+ electrodes as counter electrodes. Up to date, although several kinds of materials like Prussian blue analogues (PBAs), layer compounds, conversion-type species, polyanion compounds, metal oxides, sulfides and organic materials have been reported, most of them delivered unsatisfactory performance. Table 1.2 depicted the comparison of reported cathodes considering voltage, capacity, cycle life and rate performance.

Table 1.2 Electrochemical performance comparison of cathode materials.

Charge storage mechanism	Materials	Counter electrode	Capacity (mAh/g @mA/g)	Cycle number (capacity retention)	Voltage (V)	Highest rate	Capacity retention
Conversion	Sulfur/CNF[41]	Ca	800 @C/10	20 (300 mAh/g)	~1.3	0.05	/
	Sulfur/C[42]	Ca	760 @C/20	15 (120 mAh/g)	2.1	/	/
	ACC/S[43]	Ca	900@167	15(200 mAh/g)	~2.2	0.1 C	/
	CuS[44]	AC	200@100	30 (100 mAh/g)	~0.85	/	/

Metal oxides	$Ca_{0.13}MoO_3\cdot(H_2O)_{0.4}$[45]	AC	192@86	50 (85 mAh/g)	2.4	2 C	56% vs. 0.5 C
	$Mg_{0.25}V_2O_5\cdot H_2O$[46]	AC	120@20 70@100	500 (87%)	/	/	/
	α-MoO_3[47]	AC	< 116	/	/	/	/
	$NH_4V_4O_{10}$[48]	Ag/Ag^+	150@100	100	/	0.8 C	40% vs. 0.08 C
	Ca_xMoO_3[49]	AC	140@2	12	1.4	0.05	/
	$Ca_{0.28}V_2O_5\cdot H_2O$[50]	AC	142@10	50 (74%)	3.0	/	/
	β-$Ag_{0.33}V_2O_5$[51]	AC	179@0.1 C	50 (47%)	2.8	1 C	16% vs.0.1 C
	VOx/PC[52]	Ag	465@7.58	35	/	/	/
	$CaV_6O_{16}\cdot 2.8H_2O$[53]	AC	131.7@50	1000 (90%)	~2.2	1000 mA g^{-1}	24% vs. 50 mA g-1
	K0.25V2O5[54]	AC	100@13.3	100 (92%)	3.0	133.3 mA g^{-1}	50% vs. 13.3 mA g-1
	Zr-$NH_4V_4O_{10}$[55]	AC	77@50	500 (89%)	3.0	500 mA g^{-1}	65% vs. 50 mA g^{-1}
	$Ca_{0.14}V_2O_5$[56]	AC	247@20	400	~3.2	100 mA g^{-1}	27% vs. 20 mA g^{-1}
	δ-MnO_2[57]	AC	125@100	50 (53%)		1000 mA g^{-1}	69% vs.100 mA g^{-1}
Prussian blue analogues (PBAs)	$K_2BaFe(CN)_6$[58]	Ag/Ag^+	60	30 (55.8 mAh/g)	/	/	/
	$KFe^{3+}(Fe^{2+}(CN)_6)$[59]	Ag/Ag^+	150@23	80 (85%)	/	72 mA g^{-1}	71% vs. 18 mA g^{-1}

	$KxNiFe(CN)_6\cdot nH_2O$[60]	Ag/Ag^+	50	12 (45 mAh/g)	/	/	/
	$NiFe(CN)_6$	BP2000	60@10	50	/	/	/
	MFCN[61]	AC	80@10	35 (50%)	3.4	/	/
Polyanion compounds	$NaV_2(PO_4)_3$[62]	AC	70@5.8	30 (70 mAh/g)	3.2	1 C	82.4% vs. 0.1 C
	$NaV_2(PO_4)_3$[63]	AC	81@3.5	40 (80 mAh/g)	3.2	/	/
	$VOPO_4\cdot 2H_2O$[64]	AC	100@20	35(86 mAh/g)	2.8	2 C	33% vs. 0.1 C
	FePO4[63]	AC	72@7.5	25 (28%)	2.9	/	/
	Na_2FePO_4F[65]	AC	60@10	50	2.6	/	/
	$Ti_2O(PO_4)_2(H_2O)$[66]	AC	85@20	1500	2.6	2 C	20% vs. 0.2 C
	$Na_{1.5}VPO_{4.8}F_{0.7}$[67]	AC	78@25	500 (90%)	3.2	5 C	50% vs. 0.1 C
	N_1VPF_3[68]	AC	110@10	2000	3.5	0.9 C	59% vs. 0.1 C
Intercalation	VS_4[69]	Ca	315	/	1.7	/	/
Organic cathode	PAQS/CNT[70]	Ag/Ag^+	116@50	500	~2.2	34 C	51% vs. 0.5 C
Anion-storage cathode	Graphite[71]	AC	60@100	400 (66%)	~ 4.4	4 C	/
	Graphite[32]	Sn	72@100	350 (95%)	~ 4.3	5 C	55% vs. 1 C

1.4.1 Prussian blue analogues

PBAs have received tremendous interest as appealing cathodes for batteries.[72] The molecular formula is $A_xMFe(CN)_6\cdot yH_2O$, where A represents Li, Na, Mg, Ca, etc., M represents Ni, Ba, Ti, Co, Mn, Fe, etc., which shows a cubic structure (Figure 1.4a).[73] The initial investigation was conducted by two independent groups. J. Ingram's group demonstrated the reversible Ca-ion intercalation/extraction in a manganese hexacyanoferrate (MFCN) in non-aqueous electrolyte and assembled a Sn|MFCN CIB for the first time. Although the full cell capacity rapidly declined, this work showed the practical potential of PBAs in CIBs.[61] Sakurai's group reported a $K_xNiFe(CN)_6$ showing a discharge capacity of 50 mAh g^{-1} with CE of 91% (Figure 1.4b).[60] Apart from Mn and Ni-based PBA, Fe-based $KFe^{3+}(Fe^{2+}(CN)_6)$) was synthesized to improve the Ca^{2+} storage capacity (Figure 1.4c).[59, 74, 75]

Padigi's group investigated the effect of water content in electrolytes on the Ca^{2+} storage capability of $K_2BaFe(CN)_6$ cathode. In the $Ca(ClO_4)_2$-ACN electrolyte, no redox peaks were observed. Surprisingly, after introducing 17% deionized water into the electrolyte, two distinct peaks at 0.11 and 0.28 V emerged, providing a capacity of 55.8 mAh g^{-1}.[58] It was revealed that water molecules reduced the size of Ca ion solvation sheath and enhanced the hydration of the $K_2BaFe(CN)_6$ lattice, which led to a weaker interaction between Ca^{2+} and CN^- in the host. Similarly, another work also demonstrated the Ca^{2+} storage capacity was influenced by the water content in organic electrolytes, where a molar ratio of Ca salts and H_2O of 1:6 leads to the highest capacity of CuHCF.[76] Reaction temperature also influences the behavior of PBAs. Shiga et al. observed a pair of peaks in the CV curves of $MnFe(CN)_6$ at 60 ^oC, corresponding to the reversible intercalation/extraction of Ca^{2+}, while the peaks are negligible at 25 ^oC (Figure 1.4d).[77]

Furthermore, the ability of divalent ions (Mg^{2+}, Ca^{2+} and Zn^{2+}) insertion into nickel hexacyanoferrate (NFCN) was further confirmed by electrochemical and spectroscopic analysis. The NFCN provided capacities of 40, 60 and 50 in Mg, Ca and Zn-based systems, respectively (Figure 1.4e).[78]

1.4.2 Polyanion compounds

Polyanion compounds contain X_mO_{3m+1} (X = Si, S, Mo, P, or W) tetrahedral polyanion structures and MO_x (M=transition metal) polyhedra, which form an open framework polyanionic structure with fast ionic diffusion, excellent thermal and oxidative stabilities.[79] Moreover, the inductive effects generated from polyanions lead to high reaction voltage of transition metal; the working potential would be regulated by modifying the environment of polyanions.[80, 81] These attractive features make polyanion compounds a hot topic in cathode materials for rechargeable Ca batteries.

A desodiated Na_2FePO_4F was first demonstrated to be a Ca^{2+} host material by Ingram's group.[65] However, the illegible platform in GCD curves and broad oxidation/ reduction peaks indicated a slow Ca^{2+} diffusion kinetics. $FePO_4$ and $NaV_2(PO_4)_3$ were synthesized by extracting Li^+/Na^+ from $LiFePO_4$ and $Na_3V_2(PO_4)_3$ to investigate their Ca storage abilities. $FePO_4$ suffered from a rapid capacity decay possibly because the surface degradation reaction trapped some Ca ions (Figure 1.4f).[63] In contrast, $NaV_2(PO_4)_3$ delivered a stable capacity of 79 mAh g^{-1} for 40 cycles (Figure 1.4g). Hong's group also demonstrated the potential of $NaV_2(PO_4)_3$ for advanced cathode of CIBs simultaneously.[62] To increase the operation voltage and specific capacity of $NaV_2(PO_4)_3$ cathode, Xu et al. developed a F-doping $Na_{1.5}VPO_{4.8}F_{0.7}$ to increase the conductivity and structural integrity. It delivered a specific capacity of 88 mAh g^{-1} at 25 mA g^{-1} and a superior cyclic stability up to 500 cycles.[67, 68]

Wang et al. proposed a flake $VOPO_4 \cdot 2H_2O$ as an advanced cathode candidate for CIBs. It showed an initial capacity of 100.6 mAh g^{-1} but declined rapidly.[82] A polyanionic $Ti_2O(PO_4)_2(H_2O)$ was synthesized as an ultra-stable Ca^{2+} storage cathode due to its small volume change during calciation/decalciation (3.2%). The reversible Ca^{2+} insertion accompanied by Ti^{4+}/Ti^{3+} transformation leaded to a capacity of 85 mAh g^{-1} with a decent cyle life of 1500 cycles.[66]

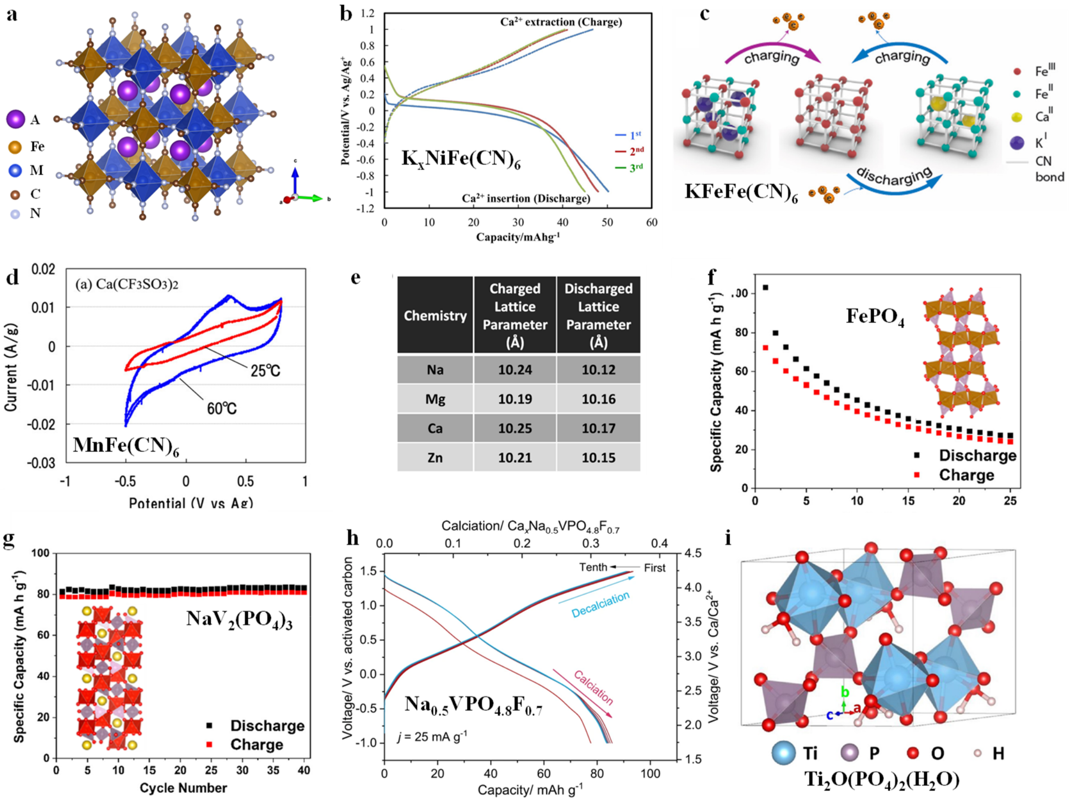

Chemistry	Charged Lattice Parameter (Å)	Discharged Lattice Parameter (Å)
Na	10.24	10.12
Mg	10.19	10.16
Ca	10.25	10.17
Zn	10.21	10.15

Figure 1.4 a) Structure of PBA. b) GCD profiles of dehydrated $K_xNiFe(CN)_6$ in $Ca(TFSI)_2$-ACN electrolyte at 25 µA cm^{-2}.[60] c) Illustration diagram of the working mechanism of $KFeFe(CN)_6$.[74] d) CV curves of $MnFe(CN)_6$ framework in $Ca(CF_3SO_3)_2$-$DEME^+TFSA^-$ electrolyte under 0.2 mV s^{-1}.[77] e) The lattice parameters of NFCN cathode under charge and discharge states in different systems.[78] Cycling performance

of f) $FePO_4$ at 7.5 mA g^{-1} and g) $NaV_2(PO_4)_3$ at 3.5 mA g^{-1}.[63] h) Voltage profiles of $Na_{1.5}VPO_{4.8}F_{0.7}$ in $Ca(PF_6)_2$-EC/PC electrolyte.[67] i) Unit cell of $Ti_2O(PO_4)_2(H_2O)$.[66]

1.4.3 Metal oxides

Metal oxides draw arising interest as cathodes for non-aqueous CIBs because of high theoretical capacity, simple synthesis process and excellent chemical stability.

Vanadium oxides

In 2003, Sakurai's group explored the Ca^{2+} storage in the c-V_2O_5, which delivered an initial capacity of 450 mAh g^{-1} at 50 μA cm^{-2}, but substantially declined with the current density raised owing to Ca^{2+} sluggish diffusion in V_2O_5 lattice.[52, 83] In 2018, Kim's group reported a nanorod Na-doped $NH_4V_4O_{10}$ (NVO) using a sodium dodecylbenzene sulfonate (SDBS) surfactant-assisted hydrothermal method.[48] The morphology of the electrode remained its rod shape without any cracks after 100 cycles, suggesting the superior stability of NVO@SDBS (Figure 1.5a). In addition, metal doping, such as Zr element, which can increase the interlayer space, improve electronic conductivity and build lattice distortion, has also been employed to enhance the performance of $NH_4V_4O_{10}$.[55]

Metal ions, including K, Mg, Ca and Sr ions, have also been introduced to V_2O_5 to enhance the Ca^{2+} insertion capability.[54] A bi-layered $Mg_{0.25}V_2O_5{\cdot}H_2O$ (MVOH) was synthesized by Mai's group and provided 120 mAh g^{-1} at 20 mA g^{-1} (Figure 1.5d).[46] Furthermore, the Ca^{2+} insertion performance of several layered vanadium oxides ($A_xV_2O_5{\cdot}nH_2O$, A=Mg, Ca, Sr) were systematically probed by the same group.[84] Other

Ca^{2+} pillared phases like $CaV_6O_{16}\cdot 2.8H_2O$,[53] $Ca_{0.28}V_2O_5\cdot H_2O$ (Figure 1.5b, c),[50] CaV_2O_4[85] and β-phase $Ca_{0.14}V_2O_5$[56] were also reported for non-aqueous CIBs.

Manganese oxides

The potential of six MnO_2 polymorphs for Ca^{2+} storage was predicted using DFT calculations by Juran et al.[86] They proposed that all studied phases can accommodate at least one Ca^{2+} and α-phase MnO_2 was the most promising one in view of working voltage, ion diffusion and stability. However, experimental investigations were not well consistent with the above theoretical calculations. A series of MnO_2 polymorphs (α, β, γ and δ-phase) were examined in $Ca(TFSI)_2$-ACN electrolyte by Zuo et al. (Figure 1.5 g, h). Specific capacities of 60, 40, 86 and 125 mAh g^{-1} were obtained by α, β, γ and δ-phase MnO_2, respectively. The δ-MnO_2 underwent an order-disorder crystal transformation while the other three phases delivered solid solution reaction without the formation of new phase.[57, 87]

In addition, $CaMn_2O_4$ was identified as a potential cathode for CIBs by combined theoretical simulations and experimental explorations. It was predicted that marokite-$CaMn_2O_4$ can store Ca^{2+}. However, the calculated diffusion energy barrier is relatively large (1 eV), suggesting reversible Ca^{2+} uptake/release in $CaMn_2O_4$ a great challenge.[88] Palacín's group explored the Ca^{2+}-storage behavior of an oxygen-deficient $Ca_2MnO_{3.5}$ cathode.[85] The operando characterizations indicated that the capacity was contributed by fluoride ions (generated from the electrolyte decomposition) intercalation instead of Ca^{2+}. These results both demonstrated the difficult Ca^{2+} migration in calcium manganate species.[89]

Other oxides

As a typical molybdenum oxide, α-MoO_3 was first explored in non-aqueous CIBs owing to its chemical stability and unique layer structure, consisting of two octahedral MoO_6 sheets. This allowed the metal ions intercalation during the reduction process. MoO_3 offered a capacity of 186 mAh g^{-1} during discharging but only 116 mAh g^{-1} during charging. Such a low CE was caused by the structural damage of MoO_3 and electrolyte decomposition during discharging (Figure 1.5i).[47] To enhance the structure stability of MoO_3, molybdenum bronze $A_xMoO_3\cdot(H_2O)_y$ (A=cations, 0<x<1, 0<y<1) was reported due to its larger interlayer spaces, originating from the pre-interlayered cations and water molecules.[45] For example, $Ca_{0.13}MoO_3\cdot(H_2O)_{0.41}$ was synthesized and provided a capacity of 192 mAh g^{-1} and enhanced cycle stability (Figure 1.5j, k). Co-based cathode, such as $CaCo_2O_4$, was also compatible with CIBs. A full cell containing $CaCo_2O_4$ cathode and V_2O_5 anode was demonstrated (Figure 1.5l, m).[90] The detailed Ca^{2+} diffusion characteristics in $CaCo_2O_4$ were explored using Ab initio molecular dynamics (AIMD) simulation.[91] The diffusion coefficient of Ca^{2+} was $>10^{-10}$ cm^2s^{-1}, which was equivalent to that of Li^+ in common cathodes, further proving $CaCo_2O_4$ a potential cathode for CIBs (Figure 1.5n).

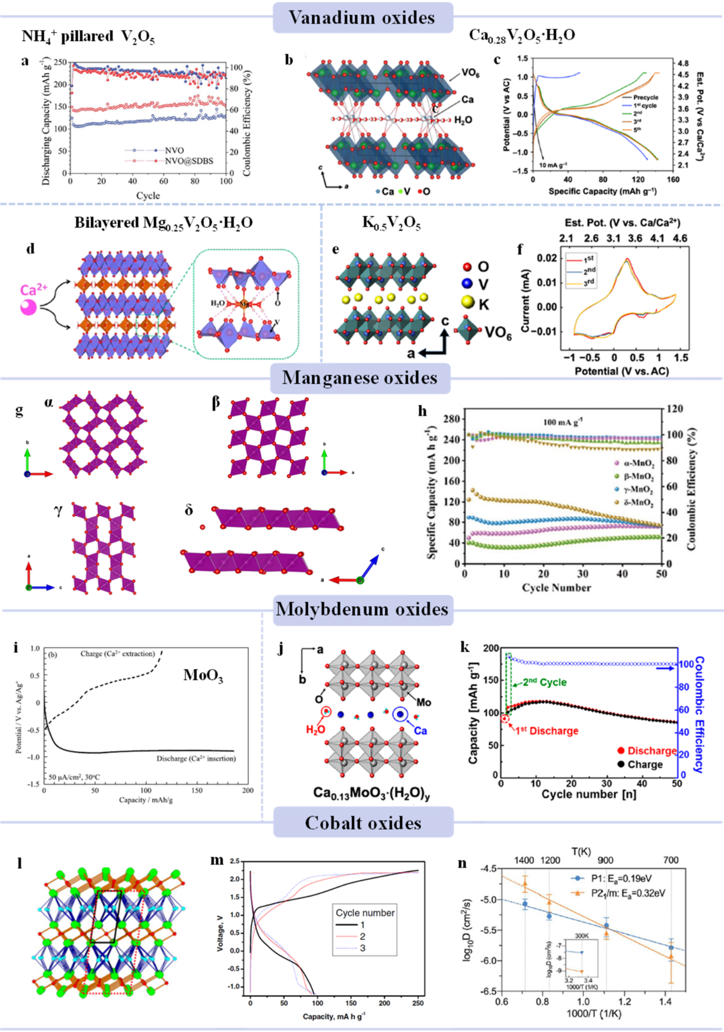

Figure 1.5 a) Cyclic stability of NVO and NVO@SDBS at 0.1 A g^{-1}.[48] b) Crystal structure and c) GCD curves of the initial 10 cycles at 10 mA g^{-1} of $Ca_{0.28}V_2O_5 \cdot H_2O$.[50] d) Crystal structure of $Mg_{0.25}V_2O_5 \cdot H_2O$.[50] e) Lattice structure and f) CV curves at 0.05 mV s^{-1} of $K_{0.5}V_2O_5$.[54] g) Crystal structures and h) cyclic stability of α, β, γ and δ-phase MnO_2.[57] i) Voltage profiles of α-MoO_3 in Ca(TFSI)$_2$-ACN electrolyte at 50 μA cm^{-2}.[47] j) Crystal structure and k) cycling performance of $Ca_{0.13}MoO_3 \cdot (H_2O)_{0.41}$.[45] l) Crystal structure of $CaCo_2O_4$. O, Co and Ca are represented in green, red and light blue, respectively.[90] m) Voltage profiles of the $CaCo_2O_4|V_2O_5$ full cell.[90] n) Calculated Ca^{2+} diffusion coefficients in $CaCo_2O_4$ by extrapolation.[91]

1.4.4 Conversion-type cathodes

Conversion-type cathodes have been thoroughly investigated in ESSs owing to their outstanding theoretical capacities, with sulfur as the most promising one.[43] The initial exploration of the sulfur cathode in non-aqueous CIBs demonstrated a S|Ca primary cell (Figure 1.6a).[92] Then, Manthiram's group presented a rechargeable Ca-S system in Ca-Li mixed electrolyte.[41] The introduction of $LiCF_3SO_3$ boosted the ionic transport of the $Ca(CF_3SO_3)_2$/tetraglyme electrolyte. Furthermore, the coordination between Li and S partially undermined the strong Ca-S ionic bond formed during discharging, promoting the subsequent conversion back to S during charging. This Ca-S battery exhibited a high capacity of 800 mAh g^{-1} but declined quickly to 300 mAh g^{-1} within 20 cycles (Figure 1.6b, c). Soluble polysulfides were detected on the cycled anode, indicating the shuttle effect of polysulfides. A similar assisting phenomenon was also observed in a Ca/Na-S hybrid battery.[93] Zhao's group developed a rechargeable Ca-S system using a new-developed $Ca[B(hfip)_4]_2$ salt.[42] CV curves and spectroscopic characterizations revealed a multistep conversion process from S to CaS final product, involving polysulfides intermediates. Nonetheless, the severe dissolution of polysulfides in electrolyte caused limited cycle life of only 15 cycles (Figure 1.6d, e).

Some metal sulfides like CuS and FeS_2 also underwent conversion reactions during the reduction/oxidation process. Ren et al. fabricated CuS nanocages and evaluated the electrochemical behavior as cathode for Mg, Zn, Fe and Ca ion batteries (Figure 1.6f).[44] According to the ex-situ XRD spectra, CuS stored calcium ions by the following two-step conversion reactions:

$$2CuS + Ca^{2+} + 2e^{-} \leftrightarrow Cu_2S + CaS \quad (1)$$

$$2Cu_2S + Ca^{2+} + 2e^{-} \leftrightarrow 2Cu + CaS \quad (2)$$

Most recently, Orimo's group developed a CuS/C-Ca full cell by employing CuS nanoparticles dispersed in carbon matrix as cathode in feasible $Ca(CB_{11}H_{12})_2$-DME/THF electrolyte (Figure 1.6g).[94] In addition, FeS_2 was also proposed as a potential conversion cathode for CIBs by using a Li-Ca bi-salts electrolyte (Figure 1.6h-j).[95]

Although S cathode has shown advantages in specific capacities, there are still some challenges, such as severe capacity decay and large voltage hysteresis. More attempts should be made to investigate advanced conversion materials and develop smart electrolytes to further boost cyclic performance and reversibility.

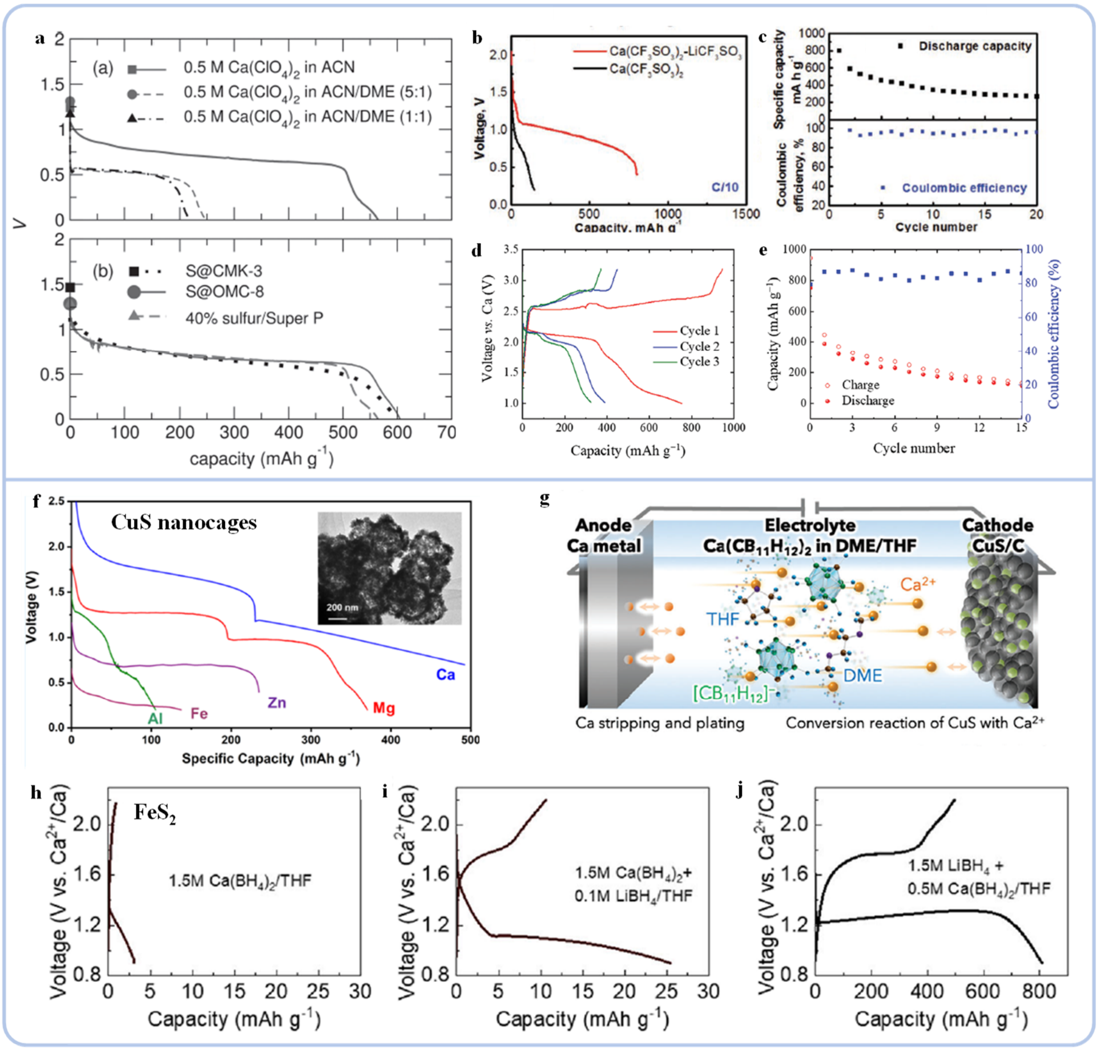

Figure 1.6 a) Discharge curves of S cathode in the primary battery.[92] b) The first discharge curve of S/CNF cathode in electrolytes with and without Li salt at C/10.[41] c) Cyclic stability of S/C cathode in Ca/Li bi-salts electrolytes at C/10.[41] d) The first three GCD curves and e) cycling performance of S/C cathode.[42] f) Discharge curves of CuS in different systems.[44] g) Schematic illustration of the CuS/C-Ca battery.[94] Voltage profiles of FeS_2 in h) 1.5 M $Ca(BH_4)_2$-THF i) 1.5 M $Ca(BH_4)_2$ + 0.1 M $LiBH_4$-THF and j) 0.5 M $Ca(BH_4)_2$ + 1.5 M $LiBH_4$-THF elelctrolytes.[95]

1.4.5 Organic cathodes

Organic materials with flexible frameworks draw increasing attention because of their potential of rapid reaction kinetics and superior stability. Furthermore, organic materials also have merits in structural designability, affordability and eco-friendliness. According to the ion storage mechanism, organic material was categorized into three groups: p-type, n-type and bipolar-type compounds.[96] N-type materials are more likely to be reduced during redox process and form negatively charged centers to absorb cations at a lower voltage. P-type compounds prefer to be oxidized and produced positively charged centers to store anions at a higher voltage. Bipolar-type organics deliver the ability to accommodate both anions and cations. Up to now, the exploration of organic electrodes is still in its infancy. Zhang et al. proposed a quinone polymer-poly(anthraquinonyl sulfide) (PAQS)/CNT as a high-capacity cathode for CIBs, which provided a capacity of 116 mAh g^{-1} (Figure 1.7a, b).[70] Besides, an aromatic compound perylene-3,4,9,10-tetracarboxylic dianhydride (PTCDA) was explored in both non-aqueous and aqueous electrolyte by Aurbach's group. It underwent similar behaviors in saturated $Ca(ClO_4)_2$-based organic and aqueous electrolytes, providing comparable capacities of about 158 mAh g^{-1}. Although the dissolution of PTCDA was partially suppressed by the saturated electrolyte, the cyclic stability could not meet the requirement of practical applications.[97]

Despite the advantages of organic compounds, the research centered on organic materials for CIBs is still limited. Thus, more attempts should be conducted to explore high-rate and ultra-stable organic cathodes.

1.4.6 Anion-storage cathode

Apart from Ca^{2+} storage cathodes, anion-storage materials are promising candidates for non-aqueous CIBs due to good reversibility, fast kinetics and high operating voltages. Nevertheless, graphite is the only anion-intercalation investigated in CIBs. A dual-carbon battery was constructed by Tang's group, where the extended graphite cathode underwent a PF_6^- intercalation/extraction mechanism.[98] They subsequently constructed a stable full cell by employing the graphite cathode and Sn anode, which stably ran for 350 cycles without significant capacity fading (Figure 1.7c, d).[32] Moreover, they also explored the impact of electrolyte concentration on the intercalation capacity of FSI^- in graphite. In a low-concentration electrolyte (0.9 M), graphite delivered a negligible discharge capacity of 10 mAh g^{-1} with a low CE of 0.8%. In comparison, a discharge capacity of 43.9 mAh g^{-1} and an improved CE of 84.6% were achieved over 400 cycles when the concentration raised to 3.5 M (Figure 1.7e-g).[71]

The development of anion-storage cathodes brings new opportunities to the CIBs, enabling the construction of high-voltage full cells. However, the high operating voltage (up to 5 V) of anion intercalation in graphite brings about inevitable electrolyte decomposition. Further investigations should focus on developing an anion-insertion cathode at moderate voltage and constructing stable cathode-electrolyte interphase to ensure high-CE dual ion batteries.

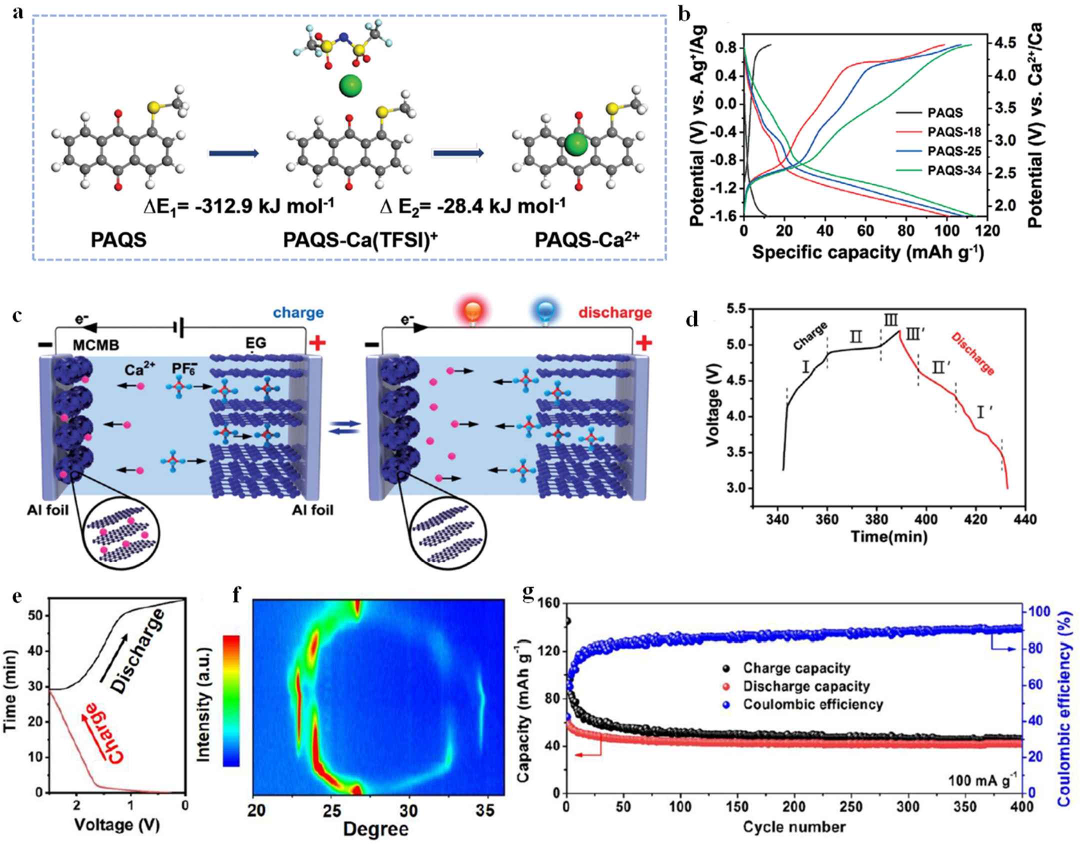

Figure 1.7 a) The optimized configuration of PAQS, PAQS-Ca(TFSI)$^-$ and PAQS-Ca^{2+}.[70] b) Voltage profiles of PAQS at 0.1 A g^{-1}.[70] c) Working principle and d) voltage profiles at 1 C of the dual ion battery.[39] e) GCD curve of the graphite in 3.5 M Ca(FSI)$_2$ electrolyte and f) corresponding in-situ XRD pattern.[71] g) Cycling performance of graphite cathode.[71]

1.5 Aqueous calcium ion batteries

Aqueous CIBs are also appealing candidates because of their benefits: a) The employment of non-toxic and non-flammable H_2O-based electrolyte brings about high safety and sustainability; b) H_2O media are highly ionic conductive, which is beneficial to construct high-power batteries; c) Cost effective and simple manufacturing process. Therefore, increasing research attention has turned to aqueous CIBs recently.

Nevertheless, the limited ESW of aqueous electrolytes caused unsatisfactory energy density, which hindered the development of aqueous CIBs.

1.5.1 Cathodes for aqueous CIBs

PBAs have attracted extensive attention in aqueous CIBs. Copper hexacyanoferrate (CuHCF) showed a Ca^{2+} storage ability of 58 mAh g^{-1}.[99] The electrolyte concentration's influence on the performance of CuHCF was further explored.[100] The hydration number of Ca^{2+} and activation energy gradually declined as the salt concentration rose, which was beneficial to the performance of CuHCF. The structural and cyclic stability of CuHCF was further improved by introducing Fe^{2+} in the CuHCF framework.[101] Despite the superior stability and high working voltage of CuHCF, the limited capacity encourages researchers to investigate high-capacity cathodes to improve the energy density of aqueous CIBs. Transition metal oxides such as $V_2O_5 \cdot 0.63H_2O$,[102] $K_{0.31}MnO_2 \cdot 0.25H_2O$,[103] $Ca_{0.16}MnO_2$,[104] $K_2V_6O_{16}$[105] and $CaV_6O_{16} \cdot 7H_2O$[106] have been reported as high-capacity cathodes, but most of them delivered unsatisfactory cycle life.

1.5.2 Anodes for aqueous CIBs

The investigations in anode materials mainly focus on organic compounds. For example, Zhi's group examined a series of organic materials in $CaCl_2$-based electrolyte, 5,7,12,14-pentacenetetrone (PT) stood out among them, considering the lower working voltage and higher specific capacity.[107] To resolve the dissolution issue of most organic monomers, an insoluble polyimide poly[N,N′-(ethane-1,2-diyl)-1,4,5,8-naphthalenetetracarboxiimide] (PNDIE) was synthesized and delivered a highly improved stability (80% retention after 4000 cycles) in $Ca(NO_3)_2$-H_2O electrolyte.[99]

Covalent organic frameworks (COFs) were also explored due to their porous structure and designable active groups.[108] Conversion-type S anode was also investigated for aqueous CIBs, which generally functioned as a cathode in organic systems. Wang's group proposed a room-temperature aqueous CIB with S/C anode and $Ca_{0.4}MnO_2$ cathode in a high-concentration gel electrolyte.[109] Besides, Liu's group reported that electrodeposited MoO_x delivered a capacity of 106 mAh g^{-1} at a small current density but an inadequate rate performance.[110]

1.5.3 Electrolytes for aqueous CIBs

The options of electrodes and output voltage of CIBs are constrained by the limited ESW of aqueous electrolytes. Xu's group proposed water-in-salt electrolytes to expand the ESW of aqueous electrolyte.[111] Recently, Adil et al. developed a $Ca(NO_3)_2$-based water-in-salt electrolyte delivering an improved stability above 2.12 V, which enabled a high-energy density and stable full cell.[111] A $Ca(OTF)_2$-based water-in-salt electrolyte with enhanced Ca^{2+} desolvation kinetics and reduced water activity was also proposed.[112] The ESW was further increased to 2.6 V by using a saturated aqueous gel electrolyte containing 10% PVA, enabling a high-voltage aqueous full cell.[109]

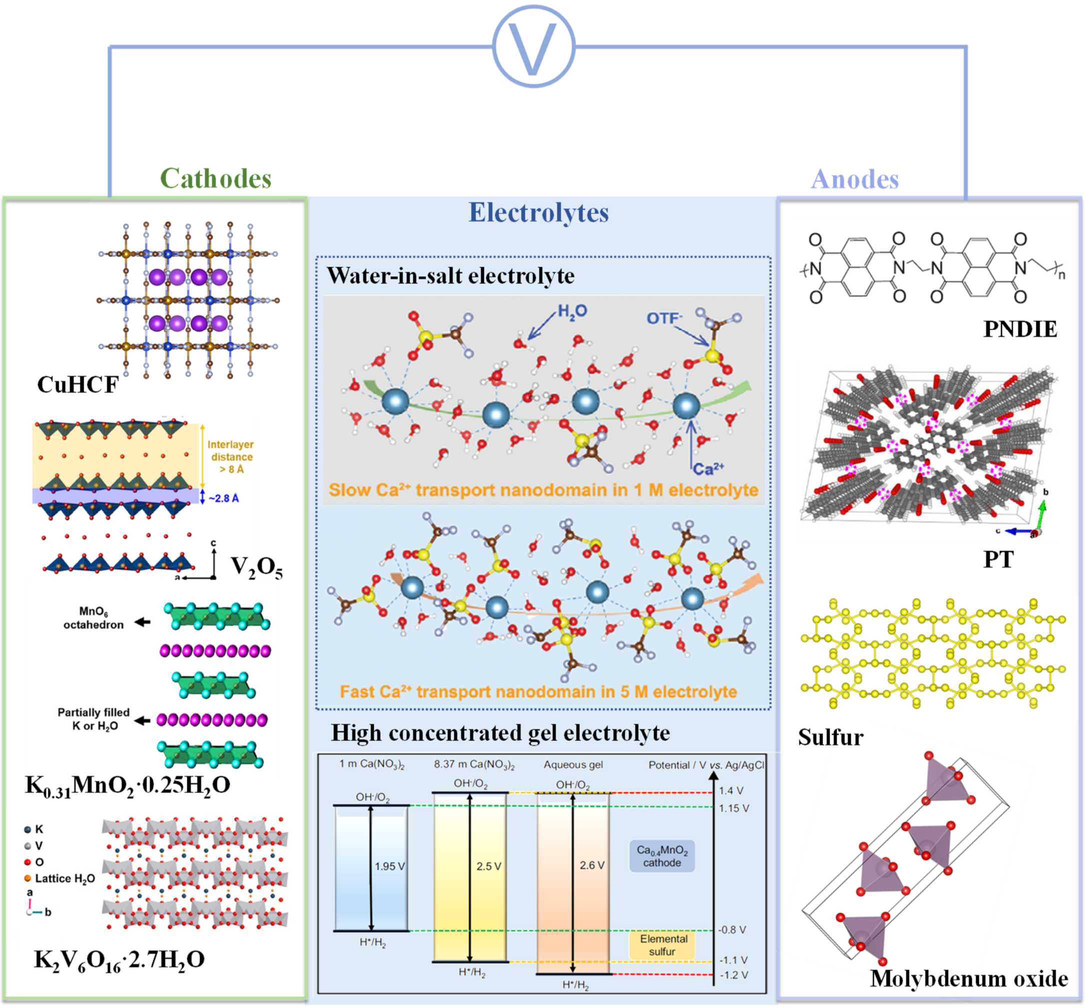

Figure 1.8 Recent development of aqueous CIBs on the cathode, anode and electrolyte optimizations.[99, 102, 103, 105, 107, 109, 112]

1.6 Objective and outline

Based on the above discussion of previous progress in non-aqueous and aqueous CIBs, the development of CIBs is largely hampered by the scarcity of advanced electrodes. Most reported electrodes delivered unsatisfactory performance considering working voltage, specific capacity, rate performance and cyclability. Furthermore, the correlation between electrolyte chemistry and electrochemical performance has rarely been investigated. In this thesis, we aim to explore high-capacity and ultra-stable electrodes for CIBs and probe their charge storage pathways. Further efforts are also devoted to understanding the influence of electrolyte chemistry on performance. The main objectives are as follows:

(1) Developing a high-capacity conversion-type electrode and understanding the underlying reaction pathway.

(2) Exploiting ultra-stable organic electrodes and unveiling the effect of electrolyte chemistry on their electrochemical behavior and performance.

Accordingly, the thesis is arranged as follows. Chapter 1 summarizes the previous works in CIBs. In Chapter 2, the experimental details are reported. Chapter 3 discusses the electrochemical behavior and reaction pathway of conversion-type electrode Se in CIBs. In Chapter 4, a high-voltage organic cathode is developed and the anion effect on its behavior is investigated. An ultra-stable and high-rate Ca-ion full cell is also demonstrated. In Chapter 5, by employing an organic anode as a model material, a synergistic proton and Ca^{2+}/Mg^{2+} co-insertion and its effects on the charge storage kinetics is probed. Coupling with a PBA cathode, an aqueous CIB with high-safety and superior rate capability is constructed. Chapter 6 offers a summary of the main results and proposes the outlook for future work.

Chapter 2. Experimental

This chapter presents the experimental settings of materials synthesis, characterizations, electrochemical measurements and theoretical simulation.

2.1 Materials synthesis

2.1.1 Se/CMK-3 composites

In a typical synthesis, wet ball-milling in acetone for 2 h was used to combine commercial Se powder and ordered mesoporous carbon (CMK-3). After evaporating acetone at room temperature, the obtained sample was pressed into a pellet and kept at 260 °C for 12 h in a sealed quartz tube to obtain Se/CMK-3 composite.

2.1.2 CuHCF

A typical co-precipitation method was employed to synthesize CuHCF particles. Dropwise addition of A solution (20 ml of 0.1 M $Cu(NO_3)_2 \cdot 3H_2O$) and B solution (20 ml of 0.05 M $K_3Fe(CN)_6$) into 60 ml H_2O were conducted with constant stirring at 25 °C. After a reaction for 6 h, the resulting product was filtered, washed with H_2O and ethanol several times, and dried for 24 h.

2.1.3 PTPAn

PTPAn powders were synthesized by polymerizing triphenylamine (TPA) under an Ar atmosphere. Specifically, a total of 0.1 mol $FeCl_3$ (0.025 mol for every hour) was added into 100 mL 0.25 M of TPA-chloroform ($CHCl_3$) dispersed solution. After 4 h reaction, 50 mL of methanol was introduced into the mixture to deposit the PTPAn powders, followed by filtration and washing with methanol three times. The resultant products were further purified through re-dissolving in $CHCl_3$ to filtrate impurities. The final

PTPAn powders were obtained by adding a mixture of acetone and 5% aqueous ammonia into the remaining filtrate, filtrating and drying the precipitation at 40 °C under vacuum.

2.2 Preparation of electrodes and electrolytes

2.2.1 Electrodes

The slurry, consisting of Se/CMK-3, acetylene blacks, and sodium alginate binder (mass ratio of 8:1:1) in deionized water, was cast onto a stainless-steel foil and dried at 80 °C overnight to fabricate Se/CMK-3 electrodes. A slurry containing 60% PTPAn powder, 30% acetylene blacks and 10% poly(1,1-difluoroethylene) (PVDF) in N-methyl pyrrolidone (NMP) was cast onto Al foil and dried at 80 °C under vacuum for 12 h. Graphite (KS6 from Timrex) and PTCDI (Aldrich) were mixed with acetylene blacks and PVDF in the mass ratio of 90:5:5 and 5:3:2, dispersed in NMP to form slurries for preparing the corresponding electrodes. The mass loading of PTPAn and PTCDI electrodes is about 1 mg. The graphite slurry was then cast onto Cu foil, while PTCDI was cast onto a stainless-steel foil and both dried at 80 °C under vacuum. The PTCDI film was peeled from stainless-steel foil to form a freestanding electrode.

2.2.2 Electrolytes

Ethylene carbonate (EC), propylene carbonate (PC), dimethyl carbonate (DMC), tetraglyme (G_4), lithium bis(trifluoromethylsulphonyl)imide (LiTFSI), magnesium bis(trifluoromethylsulphonyl)imide ($Mg(TFSI)_2$), calcium bis(trifluoromethylsulphonyl)imide ($Ca(TFSI)_2$), calcium bis(fluorosulfonyl)imide ($Ca(FSI)_2$), calcium tetrafluoroborate ($Ca(BF_4)_2$) were purchased from DoDo Chem.

0.25 M $Ca(TFSI)_2$-EC/DMC (v(EC)/v(DMC)=1:1), 1 M $Ca(TFSI)_2$-EC/PC (v(EC)/v(PC)=1:1), 1 M $Mg(TFSI)_2$-EC/PC (v(EC)/v(PC)=1:1), 1 M $Ca(FSI)_2$-G_4, 1 M $Ca(BF_4)_2$-G_4 and 1 M $Ca(TFSI)_2$-G_4 were prepared as non-aqueous electrolytes. The electrolytes were treated with a molecular sieve (4 Å). 1, 3 and 6.25 M $Ca(TFSI)_2$-H_2O were prepared as aqueous electrolytes.

2.3 Characterizations

2.3.1 Morphology

Scanning electron microscopy (SEM, TESCAN MAIA3) and transmission electron microscopy (TEM, JEOL 2010F) were used to analyze the morphologies of materials and electrodes.

2.3.2 Structure and compositional analysis

Raman and UV-vis spectra were carried out on a Witec-Confocal Raman system (UHTS 600 SMFC VIS) using an excitation wavelength of 532 nm and a UV-vis-NIR spectrophotometer (Perkin Elmer), respectively. The X-ray diffraction (XRD) patterns were recorded on the Rigaku Smartlab X-ray diffractometer. Attenuated total reflection-Fourier transform infrared spectroscopy (ATR-FTIR) spectra were conducted using the Nicolet IS50 FTIR spectrometer. The Se content in Se/CMK-3 composite was analyzed by a thermogravimetric analyzer (NETZSCH, TGA, Q50). X-ray photoelectron spectrometry (XPS) was performed by a Nexsa X-ray Photoelectron Spectrometer system. For the ex-situ Raman, XPS and ATR-FTIR test in non-aqueous system, electrodes were obtained from disassembled coin cells in a glovebox after charging/discharging to specific states, which were washed by the corresponding solvent. The solid-state ^{1}H and ^{19}F NMR were measured on a Bruker 600 MHz spectrometer (AVANCE NEO). Inductively coupled plasma optical emission spectroscopy (ICP-OES) was carried out by Agilent 720 ES.

2.4 Electrochemical measurements

CR2032 coin cells were assembled employing the active materials as working electrodes, the commercial AC as a counter/reference electrode, and glass fiber membranes (GF, Whatman) as separators. GCD process was conducted on a Neware battery testing system (CT-4008T). CV curves were measured using the BioLogic electrochemical workstation (VSP). To obtain the AC potential vs. Mg/Mg^{2+} and Ca/Ca^{2+}, its open-circuit voltage was measured versus an Ag/Ag^+ reference electrode,[54, 113] which is calibrated by a ferrocene/ferrocenium (Fc/Fc^+) couple. The electrochemical performance of batteries were conducted in environmental chambers at different temperatures (60, 50, 25, 0, -15, -25 °C). The temperature variation during the test was controlled to be less than 1 °C. Linear sweep voltammetry (LSV) was used to examine the ESW of aqueous electrolytes in a three-electrode system where stainless steel was the working electrode, Pt foil as the counter electrode and saturated calomel electrode (SCE) or Ag/AgCl as the reference electrode. Electrochemical impedance spectroscopy (EIS) of stainless-steel/stainless-steel cells was employed to examine the ionic conductivities of electrolytes, where the frequency ranged from 10^5 to 10^{-1} Hz and the potential amplitude was 5 mV. The ionic conductivities were calculated according to $\delta = L/A*R$, where R represents the obtained resistance, L represents the distance between cathode and anode and A is the area of the working electrodes.

2.5 Computational details

2.5.1 Reaction pathway of the Se/CMK-3

DFT calculations of Se/CMK-3 were conducted by applying a projected augmented wave method[114] using generalized gradient approximation (GGA) modeled by Perdew–Burke–Ernzerhof (PBE)[115] conducted in the Vienna Ab initio Simulation Package (VASP).[116] We chose a 500 eV energy cut-off, and the k-point was chosen by limiting the spacings <0.05 Å^{-1}. We set the energy convergence criterion as 10^{-6} eV and the force one as 0.02 eV Å^{-1}. We considered spin polarization. The reaction voltages were determined by this equation:

$$U=\frac{E_{Ca_xSe}-xE_{Ca}-E_{Se}}{-2xe} \qquad \text{(Equation 2.1)}$$

where U is the reaction potential, E_{Ca_xSe}, E_{Ca}, and E_{Se} are the calculated total energies of Ca_xSe, Ca, and Se, respectively, x is the intercalation number of Ca into Se, and e is the elementary charge. Note that we selected the hexagonal phase of Se as the reference rather than the monoclinic one, because of its minor energy (0.01 eV atom^{-1}) above the hull and the observed hexagonal structure of the bulk Se in Figure 3.2b.

2.5.2 Charge storage mechanism of the PTPAn

Periodic DFT calculations were performed in VASP code.[117, 118] GGA with the PBE flavor[119] was used. A 500 eV plane-wave cut-off energy was used for geometry optimization. The Brillouin-zone was sampled by 3×2×1 k-points grid. We set the energy convergence criterion as 10^{-5} eV and the force one as 0.01 eV Å^{-1}. The DFT-D3 method was used to account for the van der Waals interaction.[120] The diffusion energy barriers were determined utilizing the climbing image nudged elastic band (CI-NEB) method.[121] For AIMD simulations[122] with NVT ensemble, the temperature was set as 300 K and the time step as 2 fs.

The binding energy of anion X^- incorporated into PTPAn was defined as:

$$E_b = E(PTPAn[X_m])-E(PTPAn[X_{m-1}])-E(X^-) \qquad \text{(Equation 2.2)}$$

Desolvation energies E_{desolv} were calculated in ORCA package.[123] The geometric optimization, single-point energies and solvation energies were calculated under the B3LYP-D3BJ/6-311G*, B2PLYP-D3BJ/def2-TZVP and M06-2X/6-31G* levels, respectively.[124-129] Implicit solvent model was included in the calculations.[130]

The inserted voltage of anion X^- versus Ca/Ca^{2+} was calculated by:

$$V_{ins} = \frac{E\left(PTPAn[X]_m\right)-E(PTPAn[X]_{m-1})-[E_{gas}(CaX_2)-E(Ca)]/2+E_{desolv}(X^-)}{e} \qquad \text{(Equation 2.3)}$$

where m is the number of inserted anions, $E(PTPAn[X]_m)$, $E_{gas}(CaX_2)$ and E(Ca) represent the energies of PTPAn with anions inserted, gas-phase CaX_2, Ca atom in the most stable bulk phase, respectively, and e represents elementary charge.

2.5.3 Reaction pathway and diffusion kinetics of the PTCDI

The GGA utilized the exchange-correlation function with the PBE flavor.[115, 131, 132] To optimize the geometry, a 450 eV plane-wave cut-off energy was used and the Brillouin-zone was sampled utilizing 5×2×2 Monkhorst-Pack grid for unit cell calculations. The convergence criterion was determined as 10^{-5} eV for energy and 0.02 eV $Å^{-1}$ for force. To consider the van der Waals interaction, DFT-D3[120] approach was used. CI-NEB method[121] was employed to determine the minimum diffusion barriers, where the k-point grid of 3×2×1 was set for the 2×1×1 supercell during CI-NEB calculations.

The binding energy was calculated by:

$$\Delta E = E_{PTCDI+ion} - E_{PTCDI} - E_{ion} \qquad \text{(Equation 2.4)}$$

where $E_{PTCDI+ion}$, E_{PTCDI} and E_{ion} are the total energies of PTCDI coordinated with ions, pure PTCDI and Mg^{2+}/Ca^{2+}/H^{+}, respectively.

Chapter 3. Unlocking the reversible selenium electrode for non-aqueous and aqueous calcium-ion batteries

3.1 Introduction

Recently, significant attempts have been made to the discovery of cathodes.[42, 45, 49, 133, 134] Various materials have been reported, including layer compounds (V_2O_5,[135] α-MoO_3,[47] $VOPO_4·2H_2O$,[64] $K_{0.5}V_2O_5$[54]), PBAs ($KNiFe(CN)_6$,[60] $KFe[Fe(CN)_6]$,[59] $MnFe(CN)_6$),[58, 61, 77] transition metal oxide compounds ($Ca_3Co_2O_6$,[90] $CaMn_2O_4$[88]), polyanion compounds (NASICON-type $NaV_2(PO_4)_3$,[62] $Na_{1.5}VPO_{4.8}F_{0.7}$,[67] $NaFePO_4F$[65]) and graphite cathode which can store anions with high intercalation potential.[71] Besides, some exciting progress has also been made toward aqueous CIBs for reducing the fabrication cost and elevating the battery safety.[99, 103, 107, 109, 136, 137]

Aiming at further improving the energy densities, conversion-type cathodes have also been explored, with sulfur (S) as the most representative one.[138-141] Although the Li-S reaction shows excellent reversibility, the direct extrapolation to the Ca-S system is not successful. The initial attempt leads to a primary Ca-S battery because of poor reversibility.[92] Assisted by the lithium-ion mediation strategy, Manthiram's group recently presented a reversible Ca-S battery for the first time.[41] Furthermore, Zhao's group reports an extraordinary rechargeable Ca-S batteries in the absence of lithium salt, assisted by the newly developed $Ca[B(hfip)_4]_2$-based electrolyte.[42] It delivers a superior initial capacity of 760 mAh g^{-1}, but the long-term stability remains unsatisfactory, showing quick decay in 15 cycles. The inferior stability compared to Li-S system may lie in the distinct reaction pathway that has not been fully understood.

Selenium (Se) in the same group as S would be a promising alternative, which shows potential advantages in the cyclic stability over S, and has been widely adopted in lithium-selenium (Li-Se), sodium-selenium (Na-Se), potassium-selenium (K-Se) and magnesium-selenium (Mg-Se) battery systems.[142-148] Nevertheless, to date, there is no investigation on the Se electrode for CIBs, leaving the reversibility and reaction pathway of Ca-Se elusive.

Despite the extensive studies in metal-Se reactions, a direct extrapolation would not be sufficient as the metal properties substantially affect the phase transition pathways and the associated stability. For instance, the Li-Se system undergoes a direct conversion between Se and Li_2Se without any intermediate product in carbonate electrolytes, while multi-step reaction routes are observed in Na-Se, K-Se and Mg-Se systems but showing discrete reaction pathways (Figure 3.1).[148-151] We firstly explore the reversibility and reaction mechanism of Se in CIBs by utilizing a Se/CMK-3 (ordered mesoporous carbon) composite, which is prepared via a melt-diffusion method for stabilizing the Se electrode. The Se delivers a high specific capacity of 476 mAh g^{-1} with an average potential of 2.2 V vs. Ca/Ca^{2+} in the non-aqueous electrolyte, significantly outperforming the intercalation compounds in energy density. Then, we probe the Ca-Se reaction mechanism through both experimental studies and DFT calculations, identifying several intermediate phases and the corresponding reaction potentials. Furthermore, we investigate the possibility of employing the Se electrode in an aqueous CIB. Since the reaction potential of Ca-Se is out of the electrochemical window in a normal concentration electrolyte, we effectively expand the window to 2.3

V by exploiting 6.25 M Ca(TFSI)$_2$ for the successful demonstration of a revisable aqueous CIB.

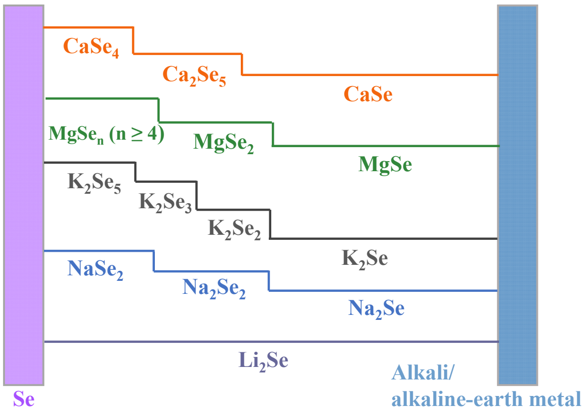

Figure 3.1 The reaction pathways of Se in different systems.

3.2 Results and discussion

3.2.1 Preparation of Se electrode

We use a classic mesoporous CMK-3 carbon to accommodate Se for producing Se/CMK-3 composite electrodes to explore the intrinsic reversibility and stability of Ca-Se reactions. A facile melt-diffusion strategy is employed for the synthesis, where Se and CMK-3 are mixed and pressed into pellets before sealing in a quartz tube under a vacuum. The sample is heat-treated at 260 °C for 12 h to allow the diffusion of Se into the pores of CMK-3 host (Figure 3.2a). As shown in Figure 3.2b, the pristine bulk Se has a well-crystallized structure (JCDPS No. 06-0362). All characteristic peaks disappear after infiltrating Se into the CMK-3 matrix, indicating the amorphous nature of Se in the composite. The presence of Se is confirmed by XPS analysis, presenting two peaks at 56.6 eV (Se 3d$_{3/2}$) and 55.7 eV (Se 3d$_{5/2}$) (Figure 3.2c). The thermogravimetric analysis (TGA) shows a Se content of 48 wt% (Figure 3.2d). The morphologies are examined by SEM and TEM. There is an absence of any bulk Se species on the surface of micrometer-sized rod-like CMK-3 (Figure 3.2e and 3.3), suggesting that Se is well infiltrated in the CMK-3 matrix. The corresponding elemental mappings substantiate that Se is uniformly distributed in the CMK-3 matrix (Figure 3.2f). No crystal lattice of Se is detected in TEM images of the composite, further verifying the amorphous Se phase (Figure 3.2g).

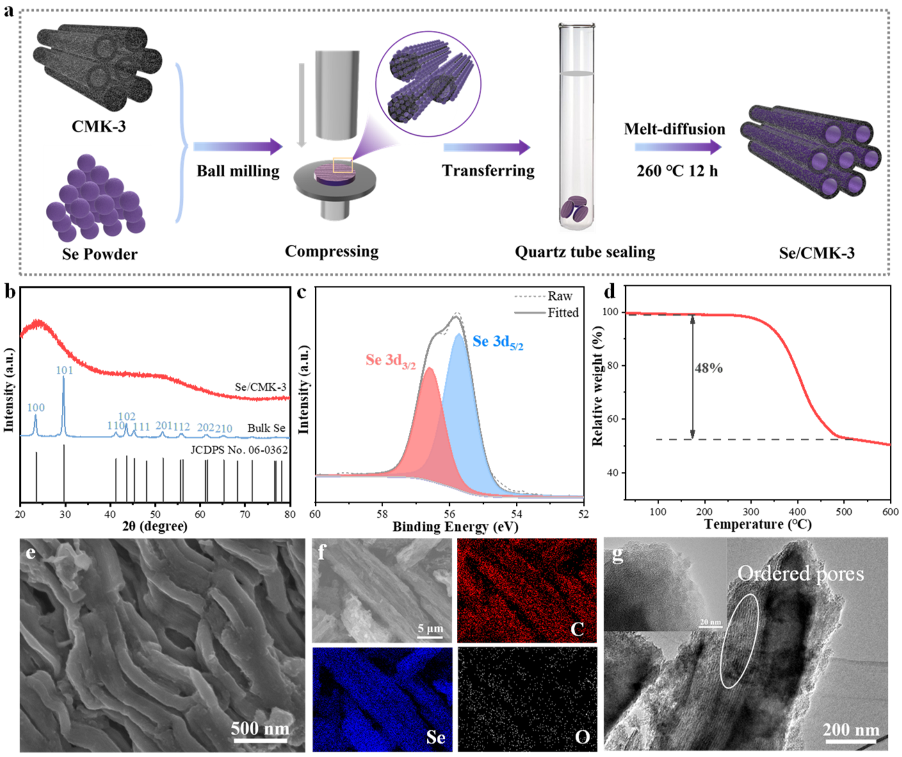

Figure 3.2 Synthesis process and structural characterization of Se/CMK-3 composite. a) Flow diagram of synthesis process. b) XRD patterns of bulk Se and Se/CMK-3 composite. c) XPS spectrum of Se 3d, d) TGA curve and e, f) SEM images and elemental mappings for C, Se and O. g) TEM image and the corresponding high resolution transmission electron microscope (HRTEM) image (inset).

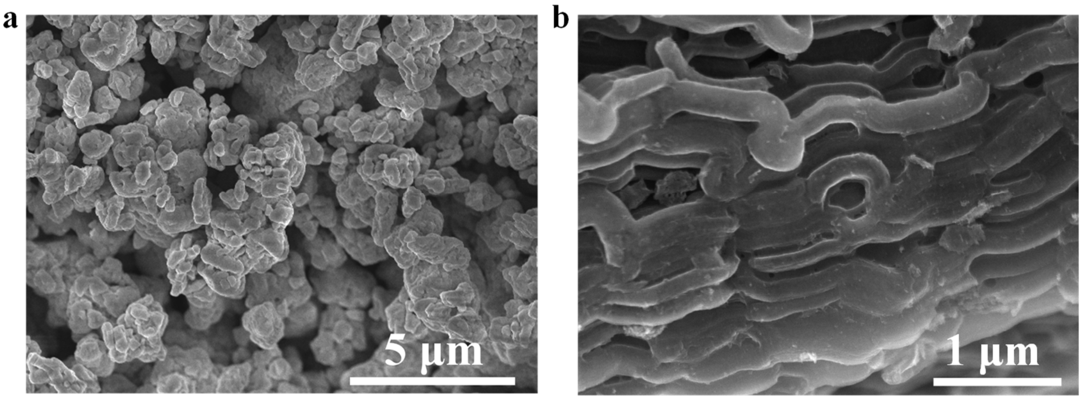

Figure 3.3 SEM images of a) bulk Se particles b) CMK-3.

3.2.2 Reversibility of Ca-Se in organic electrolyte

To investigate the redox behavior and electrochemical performance of Ca-Se reactions in the organic electrolyte, AC is employed as a counter/reference electrode owing to the nearly inhibited Ca anode plating/stripping process in most electrolytes. A classic 0.25 M $Ca(TFSI)_2$ in EC/DMC electrolyte is used to explore the reversibility in general systems. To better comprehend the electrochemical performance of Se in CIBs, the specific capacity is calculated based on the mass of Se in the electrode. We calibrate the redox potential of the AC reference electrode by a Fc/Fc^+ redox couple to determine the potential of Ca-Se reactions vs. Ca/Ca^{2+} (Figure 3.4).

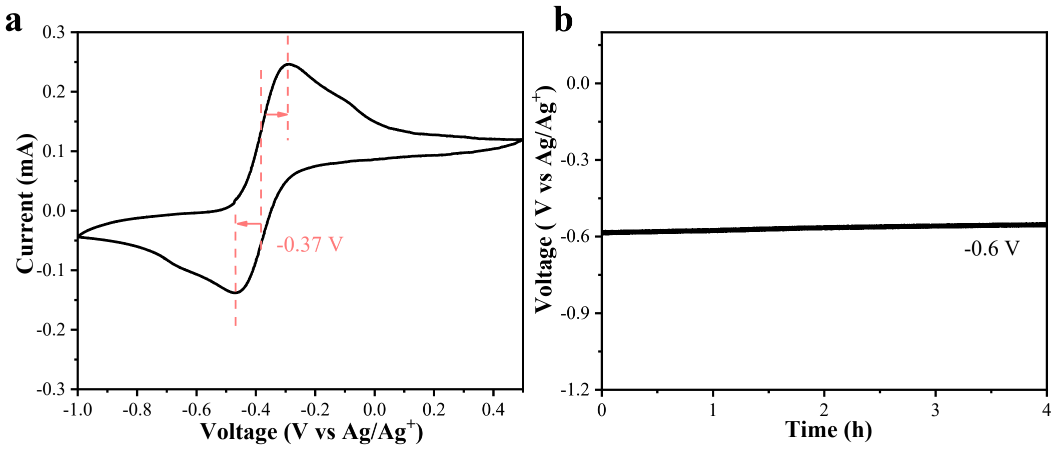

Figure 3.4 a) CV test of 5 mM ferrocene dissolved in 0.25M $Ca(TFSI)_2$ EC/DMC electrolyte (the working and reference electrodes are Pt and Ag/Ag$^+$ (0.01M $AgNO_3$ in 0.25M $Ca(TFSI)_2$ EC/DMC) electrode, respectively). The scan rate is 1 mV s^{-1}. The Fc/Fc$^+$ redox couple was measured at about -0.37 V vs. Ag/Ag$^+$, and the value of internal reference Fc/Fc$^+$ against standard hydrogen electrode is 0.4 V. Thus, the Ag/Ag$^+$ reference voltage can be estimated to be 3.64 V vs. Ca/Ca^{2+}. b) Open circuit voltage (OCV) of AC vs. Ag/Ag$^+$ reference electrode. The OCV is -0.6 V vs. Ag/Ag$^+$, thus, the AC voltage can be estimated to be approximately 3.04 V vs. Ca/Ca^{2+}.

As shown in Figure 3.5a and b, the discharge profiles exhibit three voltage plateaus at about -0.2, -0.75, and -1.3 V while there are also three voltage platforms at about -0.6, 0, and 0.55 V during the charging process. We also assemble a three-electrode Swagelok cell to simultaneously monitor the potential of working and counter electrode (Figure 3.6a). Because of the large excess of the AC, the potential of the counter electrode only slightly deviates (< 0.1V) during the charge/discharge process (Figure 3.6b-d). The average discharge voltage of Se/CMK-3 electrode is calculated to be 2.2 V vs. Ca/Ca^{2+}, which surpasses the value in the alike sustainable Na-Se (≈ 1.5 V) and

K-Se (≈ 1.4 V) batteries[145, 151-153] The specific capacity of Se/CMK-3 electrode suffers from a rapid decay and drops to only 96 mAh g^{-1} after 20 cycles at 100 mA g^{-1} (Figure 3.7a). Such deterioration should be caused by the large volume expansion of Se and loss of active materials attributed to the dissolution of polyselenides during discharging/charging, which has been widely observed in other metal-Se batteries.[154-159] To enhance the cyclic stability of Se/CMK-3 electrode, a free-standing carbon nanotube (CNT) interlayer is introduced between the Se/CMK-3 electrode and the separator for preventing the shuttle of dissolved species.[160, 161] Note the neat CNTs do not directly contribute much to the capacity (Figure 3.8). With the assistance of CNT interlayer, a high specific capacity of 223 mAh g^{-1} is realized after 50 cycles at 100 mA g^{-1} with significantly reduced polarization (Figure 3.7). The voltage profiles at various cycles do not vary significantly (Figure 3.9), demonstrating the similar reaction paths and decent reversibility of the Se electrode for the long-term cycles.

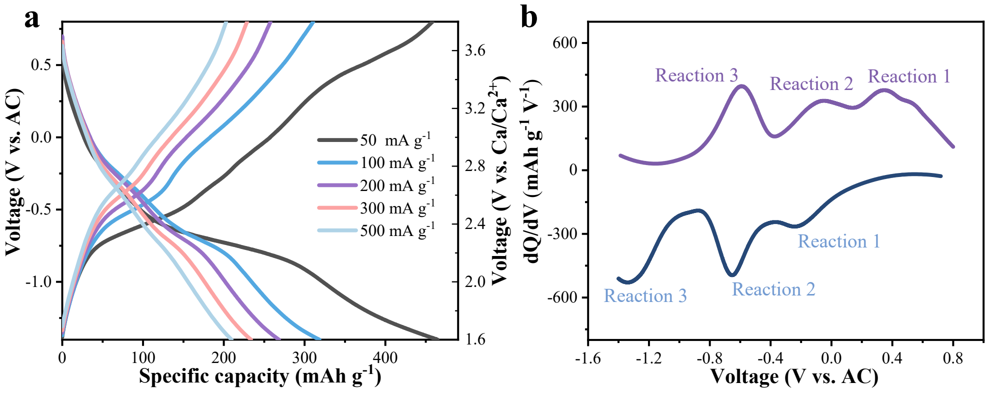

Figure 3.5 a) Voltage profiles under different current densities. b) dQ/dV curves at 30 mA g^{-1}.

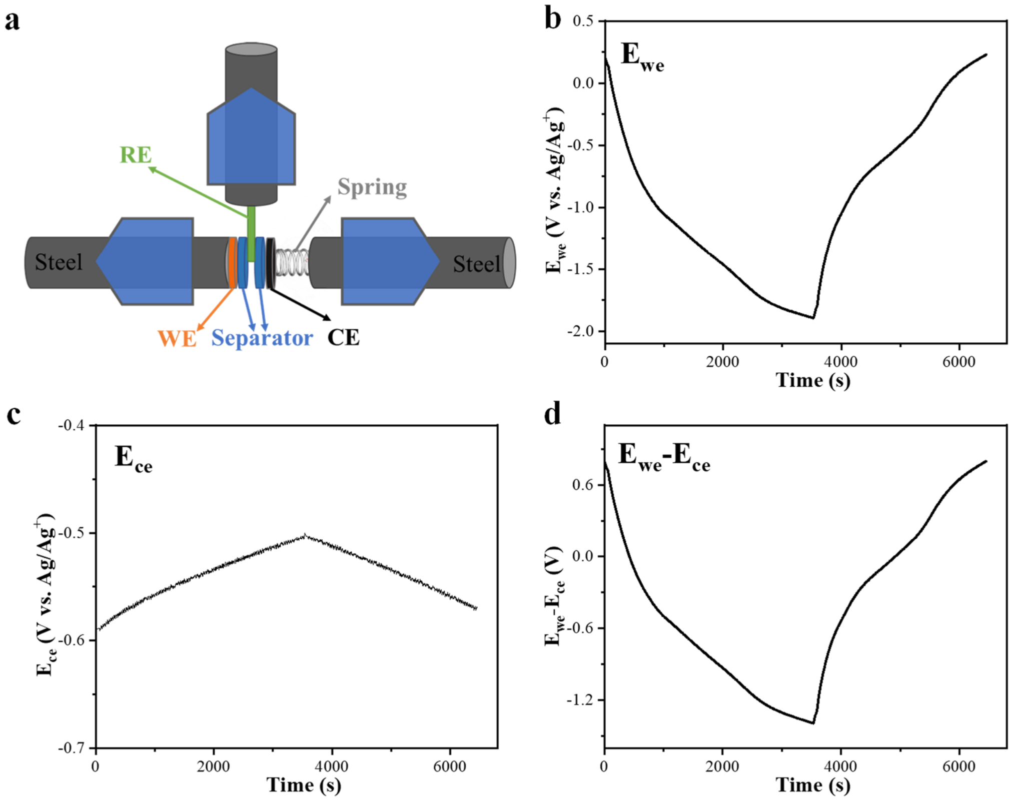

Figure 3.6 a) Schematic diagram of the three-electrode Swagelok cell. The curves of b) E_{we}, c) E_{ce} and d) E_{we}-E_{ce} in a three-electrode Swagelok cell.

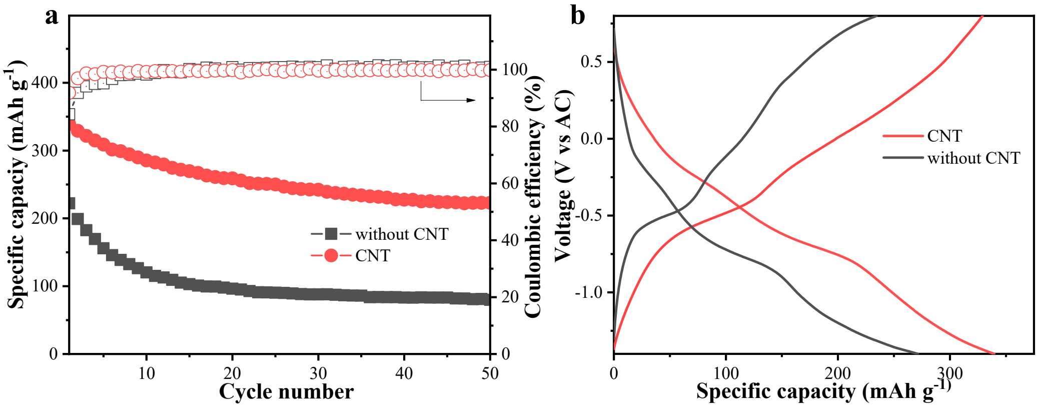

Figure 3.7 a) Cycling performance, b) voltage profiles of Se/CMK-3 electrode with/without CNT interlayer at 100 mA g^{-1}.

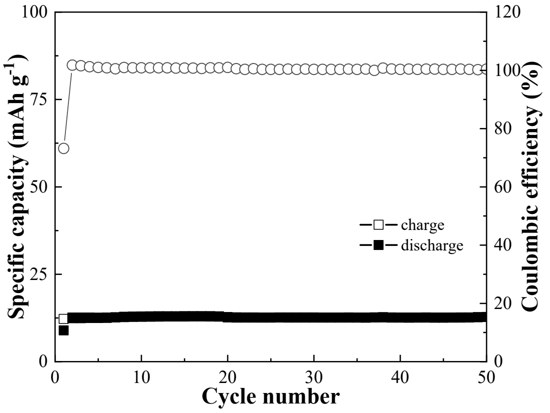

Figure 3.8 The specific capacity of CNT layer in CIBs. The CNT delivers a specific capacity of 12.5 mAh g^{-1} at 50 mA g^{-1}.

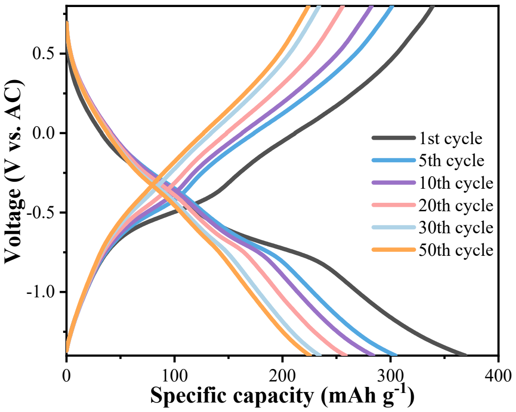

Figure 3.9 Voltage profiles of Se/CMK-3 electrode with CNT at 100 mA g^{-1}.

To further explore the impact of the CNT interlayer on the reaction kinetics, electrochemical impedance spectroscopy is carried out at fresh cells and after 3 cycles (Figure 3.10). The Nyquist plots of the cells before cycling present one semicircle followed by a slope line. An equivalent circuit model in Figure 3.10c is employed to fit the curves, where R_e represents the electrolyte resistance, R_{ct} represents charge transfer resistance between the electrode/electrolyte interface. The cell with a CNT interlayer shows a lower R_{ct} before cycling. After cycling, a new semicircle appears in the Nyquist plots of the cells, attributed to interface contact resistance (R_p) between the cathode and polyselenides.[162] The cell with a CNT interlayer shows a greatly reduced R_p compared with that without CNT, indicating a solid capability for trapping polyselenides (Table 3.1).

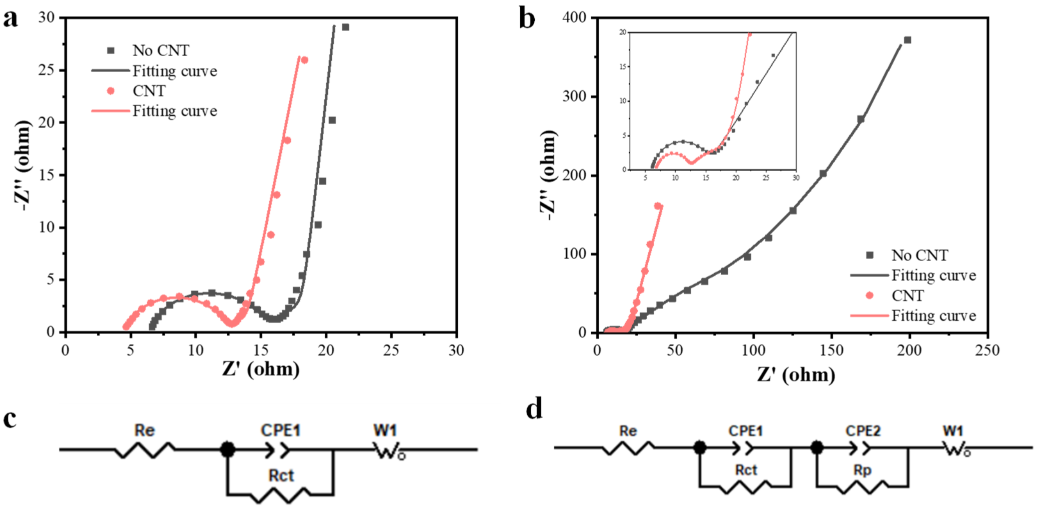

Figure 3.10 Nyquist plots of the cells with CNT interlayer and without interlayer: a) fresh cells and b) after 3 cycles. c, d) The corresponding equivalent circuits.

Table 3.1 Impedance parameters of the cells with CNT interlayer and without interlayer.

	Before cycle		After 3 cycles		
	R_e	R_{ct}	R_e	R_{ct}	R_p
No CNT	6.5	8.4	6.9	8.9	443.2
CNT	4.6	7.4	5.7	5.2	6.9

The cell also shows attractive rate performance (Figure 3.11a), suggesting the di-valence and large size (100 pm compared to 76 pm for Li^+) of Ca^{2+} is not an obstacle for designing high-power CIBs. Figure 3.11c displays long-term cycling at a higher current density of 500 mA g^{-1}: the Se/CMK-3 electrode could deliver a reversible capacity of 150 mAh g^{-1} with nearly 100% CE for 300 cycles. In addition, CVs at various scan rates are carried out to evaluate the reaction kinetics of Ca-Se reaction (Figure 3.12). The charge is stored through the combined diffusion-controlled and pseudo-capacitive behavior. The ratio of pseudo-capacitive contribution is de-coupled,[163] which increases with the growing scan rates, from 44% at 0.3 mV s^{-1} to 60% at 1 mV s^{-1}.

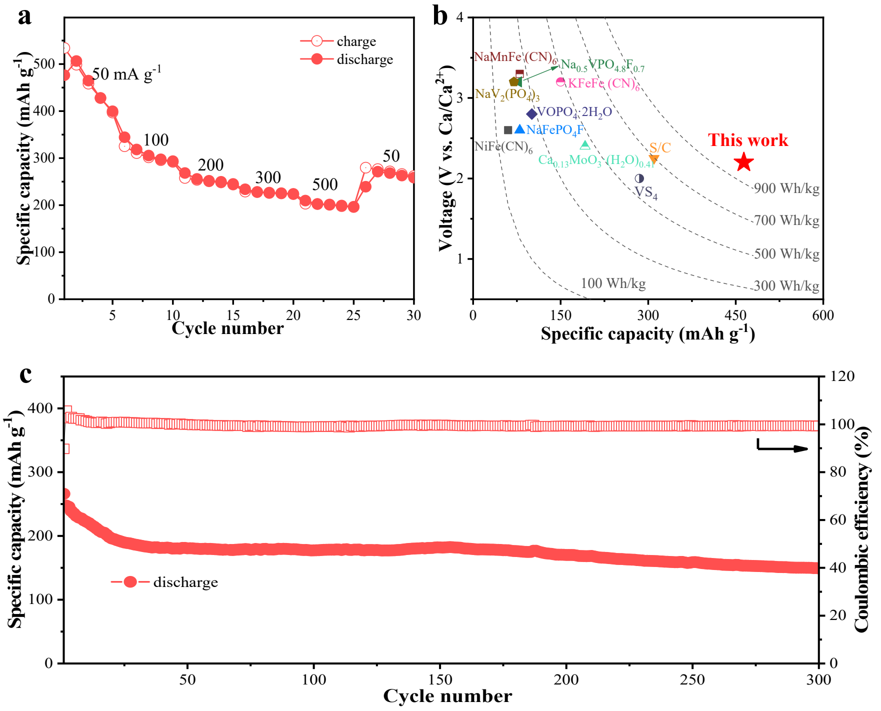

Figure 3.11 a) Rate performance under various current densities. b) Comparison of specific capacity and average voltage for reported cathodes in CIBs. The value in the 3rd cycle is adopted for all the materials to show the practically available performance. c) Cyclic stability at 500 mA g^{-1}.

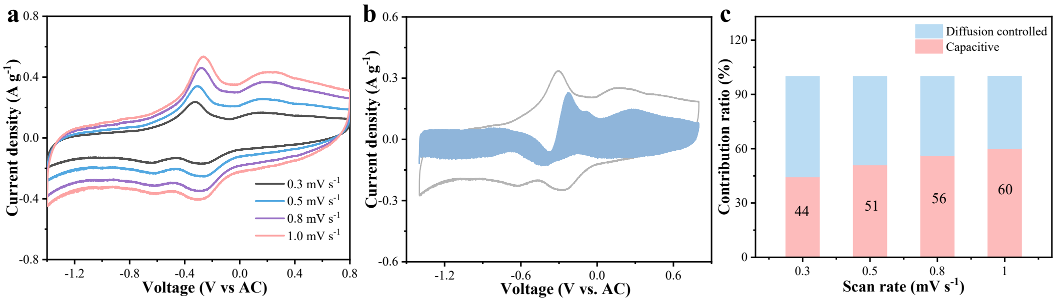

Figure 3.12 a) CV curves of Se/CMK-3 at a series of scan rates of 0.3, 0.5, 0.8 and 1 mV s^{-1}. b) Capacitive contribution at 0.5 mV s^{-1}. c) The calculated pseudo-capacitive and diffusion-controlled contributions at a series of scan rates.

Compared to other reported cathodes for CIBs, Se/CMK-3 electrode attains an exceptional energy density thanks to the extraordinary capacity in Ca^{2+} uptake at a decent potential (Figure 3.11b). These results indicate the Ca-Se reaction exhibits superior reversibility and stability with appropriate electrode design. A high-energy Ca-Se battery would be possible if a reversible Ca metal anode could be realized, which is intensively explored in the community. Furthermore, a sample with ~75% Se is also prepared to examine the effect of active mass loading. It is a delight to observe that the cyclic capacity and stability are well maintained (Figure 3.13). Lastly, the cyclic performance could be further boosted by the optimization of the interlayer. Enlightened by the studies in Li-S batteries,[164] we adopt a reduced graphene oxide/CNT hybrid interlayer, which greatly alleviates the early capacity degradation (Figure 3.14).

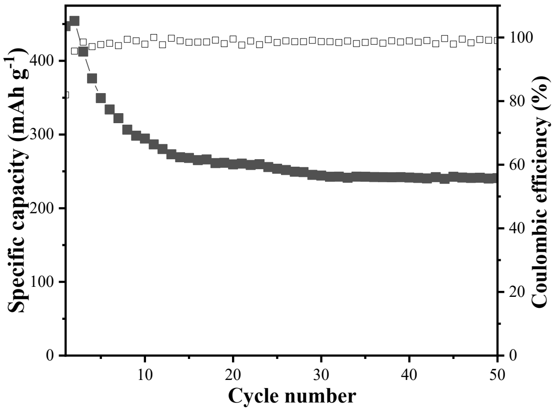

Figure 3.13 The cycling performance of Se/C composite with a Se content of 75%.

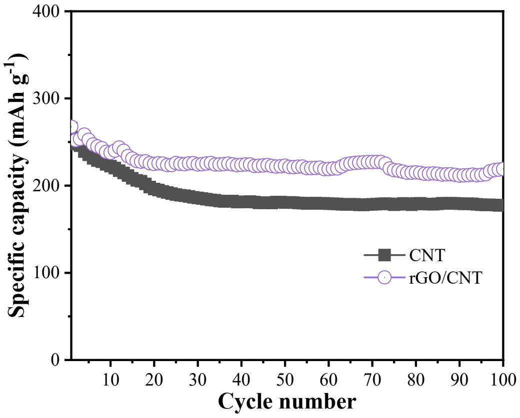

Figure 3.14 Cycling performance of Se/CMK-3 electrode with different protective interlayer.

The phase change after discharge is studied by XRD using the crystalline bulk Se considering its higher crystallinity compared to Se/CMK-3. As shown in Figure 3.15a, the fully discharged electrode shows an amorphous structure without evident XRD peaks, which should be ascribed to the large radius of Ca^{2+} and its divalency, similar to those observed in Ca-S system.[41] To further understand the reaction mechanism of Se electrode, ex-situ Raman test for bulk Se electrode at different discharge and charge states are carried out. As shown in Figure 3.15b, the pristine Se shows a peak at 236 cm^{-1}. During discharge, this peak becomes weaker. Another peak at about 252 cm^{-1} appears and the intensity increases as the reaction progresses, corresponding to the gradual formation of CaSe similar to the phenomenon in the Mg-Se system.[165, 166] In addition, a weak peak presents at about 285 cm^{-1}, which could be assigned to Se_x^{2-}. Upon charging, the CaSe and Se_x^{2-} peaks gradually fade out, accompanied by the recovery of Se peak at 236 cm^{-1}, indicating the reversible Ca-Se reactions.

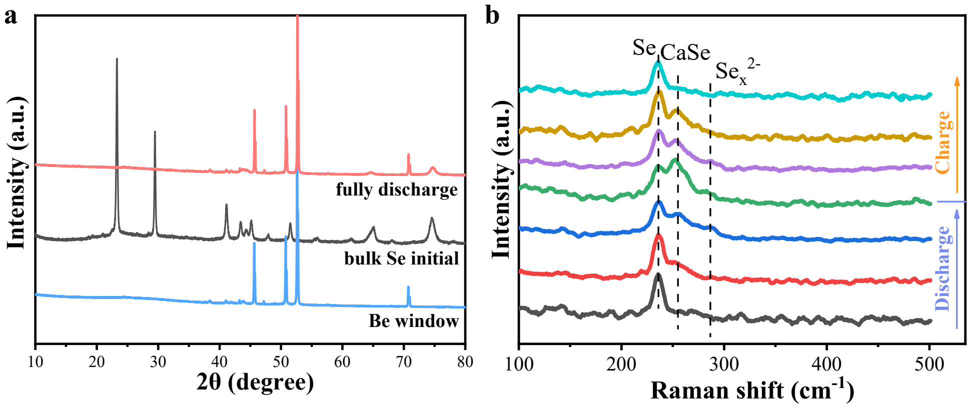

Figure 3.15 a) XRD patterns of the battery case with a beryllium foil window, initial bulk Se, and fully discharged bulk Se. b) Ex-situ Raman test of the bulk Se electrode at selected discharge/charge states.

We semi-quantitatively probe the chemical composition of Ca-Se reaction products by energy dispersive spectroscope (EDS) elemental mapping of Se/CMK-3 electrode at various alloying/de-alloying stages. Ca element is uniformly distributed on the fully discharged electrode (Figure 3.16a-c). The atomic ratio of Ca and Se is 0.7 (Table 3.2), agreeing well with the obtained discharge capacity of 476 mAh g^{-1}. Upon charging, the electrode could be reversibly transformed back to Se, as confirmed by the almost disappeared Ca element signals (Figure 3.16d-f). The 3rd discharge/charge mapping also presents a similar phenomenon (Figure 3.17), revealing its decent reversibility of alloying/de-alloying behavior during continuous cycling. TEM image and the corresponding EDS elemental mappings indicate the Se remains uniform distribution in CMK-3 host without apparent segregation after discharge (Figure 3.16g, h).

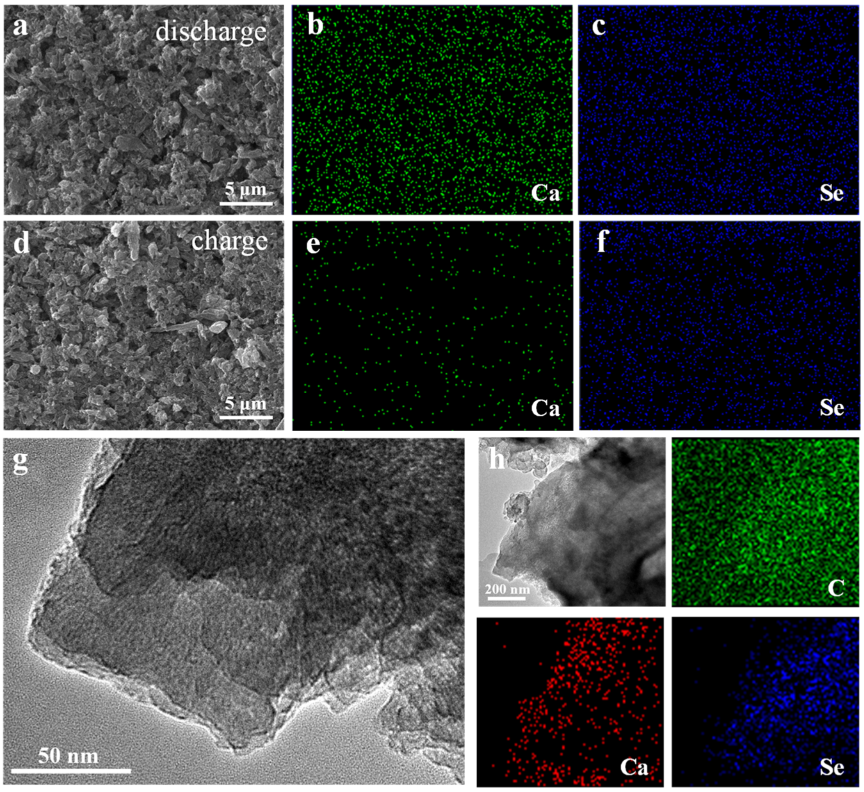

Figure 3.16 Analysis for the reaction mechanism of Se/CMK-3 electrode. SEM images and corresponding Ca and Se mappings a-c) after discharge and d-f) after charge. g, h) TEM images and corresponding C, Ca, and Se mappings after discharge.

Table 3.2 The atomic content of elements in the Se/CMK-3 electrode after discharge.

Element	Weight%	Atomic%
C K	67.22	82.78
O K	13.80	12.76
Ca K	4.99	1.84
Se L	13.99	2.62
Totals	100.00	100.00

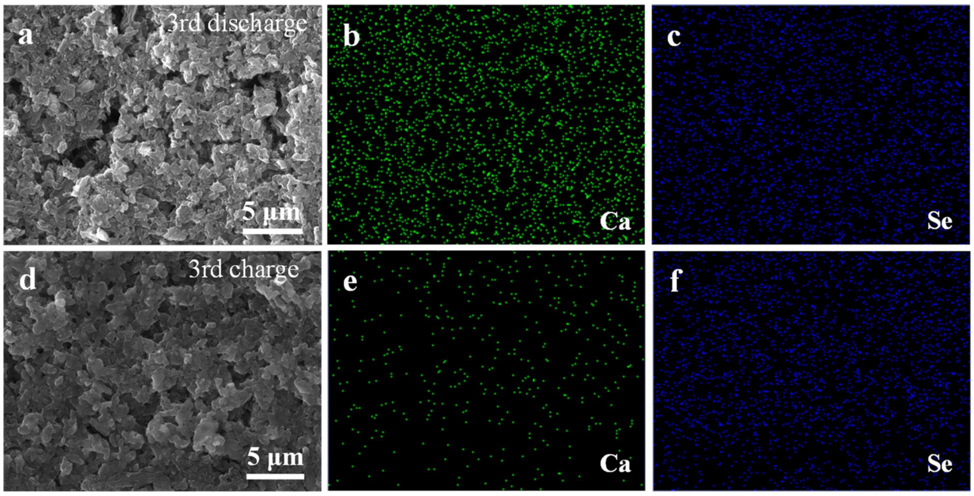

Figure 3.17 SEM images and elemental mapping of a-c) Se/CMK-3 electrode after the 3rd discharge, d-f) after the 3rd charge.

XPS analysis is carried out to unravel the discharge/charge reaction pathway of Se/CMK-3 electrode (Figure 3.18). Pristine Se/CMK-3 electrode displays Se $3d_{5/2}$ and $3d_{3/2}$ peaks located respectively at 55.7 and 56.6 eV. After full discharge, the Se 3d spectrum moves towards lower binding energy and could be split into three doublet peaks. The peaks at 53.5/54.4 eV can be attributed to CaSe, and the doublet at 55.1/56.0 eV corresponds to polyselenides $CaSe_x$ ($2 \leq x \leq 8$), which indicates the Se is converted into CaSe through multi-step reactions. These findings are consistent with the results of voltage profiles. Residue Se signal could still be detected due to the uncompleted reaction, the reason why only 0.7 Ca^{2+} per Se is uptake as inferred from the EDS mapping and reversible capacity (Table 3.2). The existence of polyselenides is further verified by the UV-vis spectrum with an absorption peak at around 320 nm (Figure 3.19).[166, 167]

Upon charging, the Se 3d peaks return to the binding energy position of pristine Se. The XPS spectra of Se/CMK-3 electrode after the 3rd cycle at discharge and charge states show a similar trend (Figure 3.20), proving the subsequent cycles follow the same pathway and the remarkable reversibility of Se/CMK-3 electrode. In short, the above-detailed analysis demonstrates the Se could be reversibly converted into CaSe, and its reaction path is multi-step redox transformation with the generation of intermediate $CaSe_x$ ($2 \leq x \leq 8$) products.

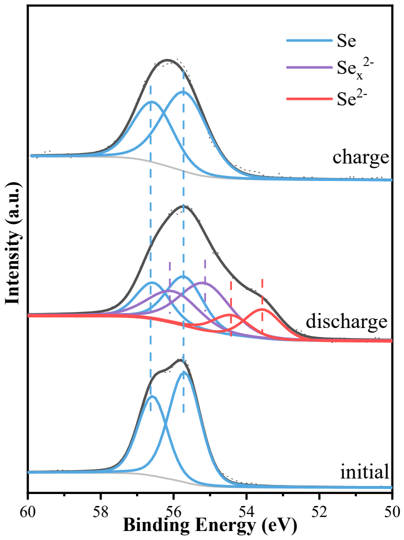

Figure 3.18 XPS Se 3d spectra at different electrochemical states.

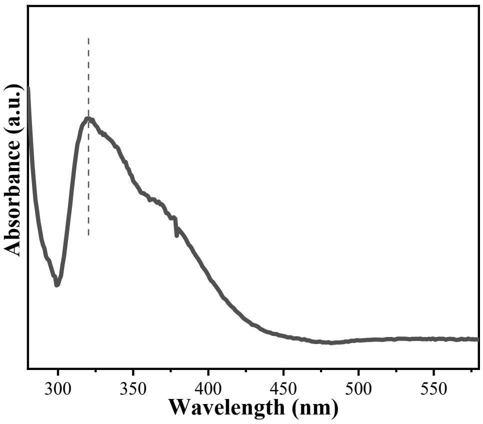

Figure 3.19 The UV-vis spectrum at the half discharge state.

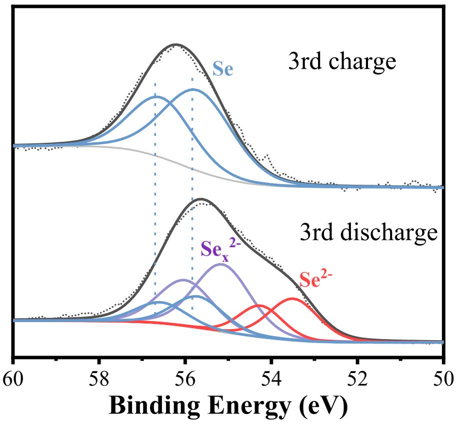

Figure 3.20 XPS Se 3d spectra of Se/CMK-3 electrode after the 3rd discharge and charge process.

3.2.3 Theoretical calculation of the reaction pathway

The experimental exploration of the detailed Ca-Se reaction pathway is restricted by the poor crystallinity of $CaSe_x$ intermediate phases. Thus, we adopt the DFT method to screen all the possible phases, including those derived from the analogies in metal (Li, Na, K, Mg, and Ca)-non-metal (S, Se, and P) systems.[168] Figure 3.21a shows the formation energies of different calcium selenium compounds with varying Ca molar ratios. Among the over 50 candidates, only an intermediate phase of $CaSe_4$ is thermodynamically stable before reaching CaSe, the end-discharge product with the lowest formation energy per atom. Note that the stability of these phases is evaluated at 0 K in the DFT calculations, which may differ from the experimental observations at room temperature (298 K). Therefore, we compare the theoretical prediction with the experimental results in Figure 3.21b. A good agreement of $CaSe_4$ and CaSe in the composition and reaction voltage is observed. An additional plateau at around 2.2 V appears in the experimental data but is not predicted by the convex-hull plot in Figure 3.21a. The most possible phase would be Ca_2Se_5 as inferred from Ca/Se atomic ratio (calculated based on the reversible capacity), and the reaction potential (vs. Ca/Ca^{2+}). The three-step conversion reaction could be further confirmed in the dQ/dV curve (Figure 3.5b). It shows three pairs of peaks, corresponding to the transformation of Se to triclinic $CaSe_4$ and further to orthorhombic Ca_2Se_5 until cubic CaSe during Ca ion uptake, as illustrated in Figure 3.21c. The detailed crystallographic structures of these three Ca-Se phases are depicted in Table 3.3-3.5.

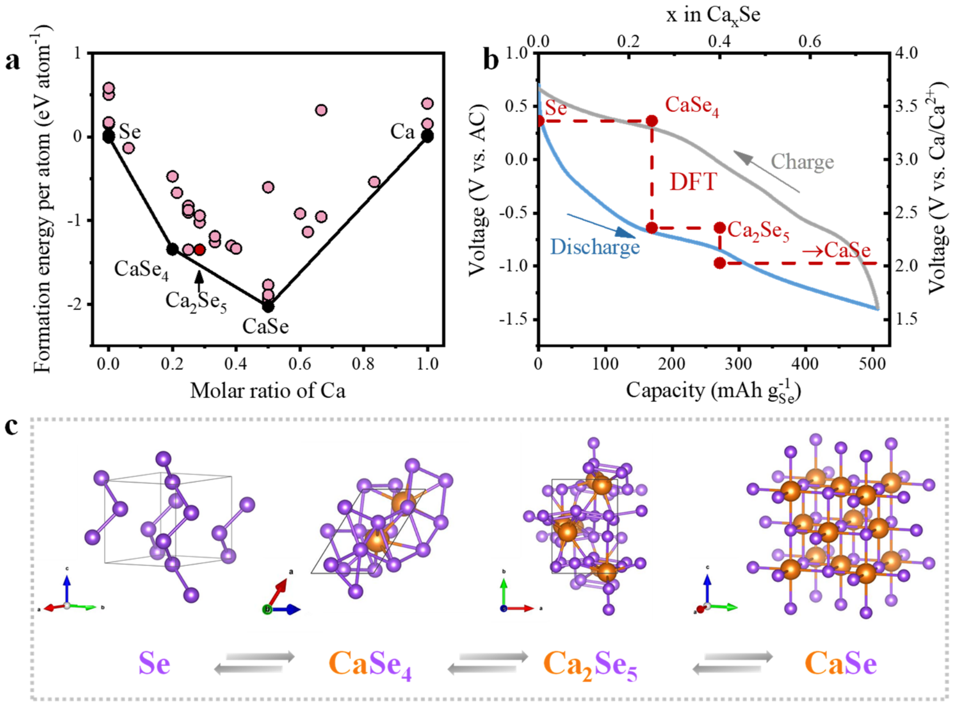

Figure 3.21 DFT calculations of the reaction pathway of Se cathode. a) Formation energies of predicted calcium selenides by theoretical calculations. The black points in the hull represent thermodynamically stable phases, while in the convex the red points represent the unstable phases with the purple point for the metastable Ca_2Se_5 phase. b) Computed equilibrium voltage curves and experimental curves of Se electrode. c) Computed electrochemical conversion path of Se electrode for CIBs.

Table 3.3 Structural parameters of $CaSe_4$ computed by DFT.

Atom	Wyckoff position	Atomic position			Occupancy
		x/a	y/b	z/c	
Ca (1)	1a	0.825	0.504	0.799	1
Ca (2)	1a	0.398	0.504	0.725	1
Se (1)	1a	0.503	0.227	0.349	1
Se (2)	1a	0.505	0.227	0.849	1
Se (3)	1a	0.045	0.324	0.481	1
Se (4)	1a	0.039	0.325	-0.011	1
Se (5)	1a	0.280	0.704	0.558	1
Se (6)	1a	0.605	0.716	0.572	1
Se (7)	1a	0.785	0.715	0.892	1
Se (8)	1a	0.102	0.705	0.236	1

Space group: P1 [1]; $a = 7.455$ Å, $b = 14.545$ Å, $c = 5.159$ Å; $\alpha = 130.452^o$; $\beta = 46.220^o$; $\gamma = 123.649^o$; $V = 301.681$ Å^3.

Table 3.4 Structural parameters of Ca_2Se_5 computed by DFT.

Atom	Wyckoff position	Atomic position			Occupancy
		x/a	y/b	z/c	
Ca (1)	4a	0.663	-0.010	0.447	1
Ca (2)	4a	0.263	0.563	0.299	1
Se (1)	4a	0.561	0.430	0.186	1
Se (2)	4a	0.365	-0.113	0.093	1
Se (3)	4a	0.865	0.835	0.093	1
Se (4)	4a	0.440	0.622	0.683	1
Se (5)	4a	0.652	0.607	0.490	1

Space group: $P2_12_12_1$ [19]; a = 5.223 Å, b = 7.487 Å, c = 19.928 Å; $\alpha = \beta = \gamma = 90^o$; V = 779.292 $Å^3$.

Table 3.5 Structural parameters of CaSe computed by DFT.

Atom	Wyckoff position	Atomic position			Occupancy
		x/a	y/b	z/c	
Ca (1)	4a	0	0	0	1
Se (1)	4b	0.5	0	0	1

Space group: Fm-3m [225]; a = b = c = 5.965 Å; $\alpha = \beta = \gamma = 90^o$; V = 212.210 $Å^3$.

3.2.4 Exploration in aqueous system

Considering the superior reversibility of Ca-Se reaction, we extend the research to the aqueous electrolytes for building high-safety aqueous CIBs. We first explore the electrochemical window of 1 M Ca(TFSI)$_2$ in H_2O electrolyte (Figure 3.22a), which is too narrow to sustain the Ca-Se conversion reactions. Therefore, we expand the ESW of the aqueous electrolyte by increasing the Ca(TFSI)$_2$ salt concentration. It is found that the electrolyte with 6.25 M Ca(TFSI)$_2$ in H_2O would fulfill the stability requirement. The electrolyte has a wide ESW of 2.3 V, allowing the construction of high-voltage CIBs. We first evaluate the electrochemical behavior of Se/CMK-3 electrode in the cell with AC as the counter/reference electrode. The open-circuit voltage of AC is ~0.17 V vs. SCE (Figure 3.23). Thus, the voltage of AC vs. Ca/Ca^{2+} is ~3.28 V in an aqueous electrolyte. The CV curve of Se/CMK-3 electrode shows two pairs of cathodic/anodic peaks (inset of Figure 3.22b), differing from the observations in organic system. It may be related to the kinetics differences in the two electrolytes, which significantly affect the reaction pathway, as widely observed in the conversion reaction under aqueous battery.[151] A reversible capacity of 190 mAh g^{-1} is retained after 50 cycles at 300 mA g^{-1} in the aqueous electrolyte (Figure 3.22b). The capacity fading is likely to arise from the soluble short-chain CaSe$_x$ and CaSe in aqueous electrolyte, similar to the aqueous metal-S systems.[169, 170] The reaction mechanism in the aqueous electrolyte is further investigated by XPS analysis (Figure 3.22c). It shows similar multi-step conversions between Se and CaSe involving the intermediate products of CaSe$_x$. SEM images and corresponding elemental mappings of Se/CMK-3 electrode after discharge and charge further prove the reversibility of the electrochemical reaction (Figure 3.24).

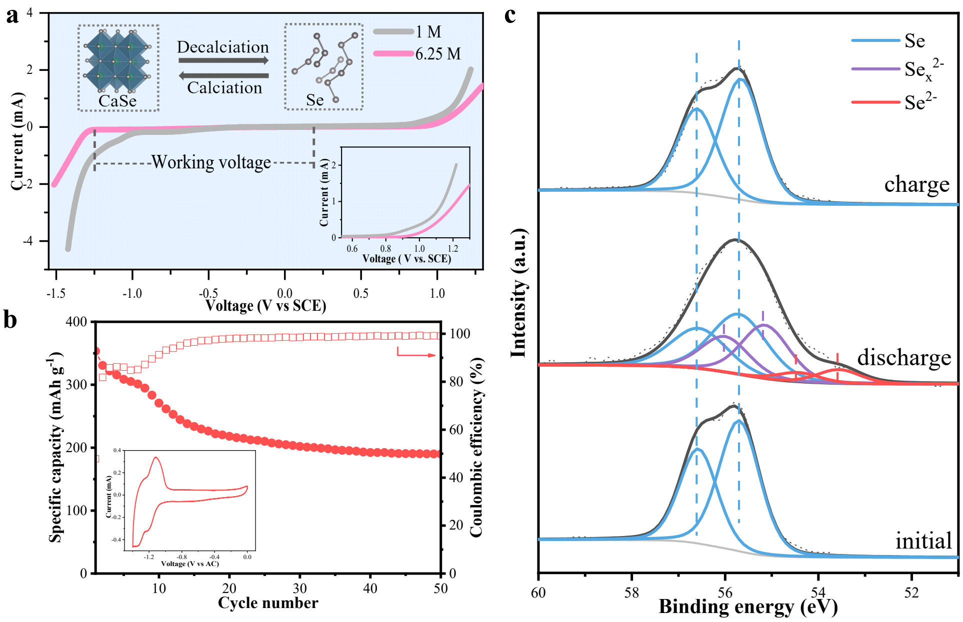

Figure 3.22 The electrochemical performance and reaction mechanism analysis of Se/CMK-3 electrode in an aqueous system. a) The electrochemical stability of 1 M and 6.25 M aqueous electrolytes and the voltage range of conversion reaction between Se and CaSe. b) Cycling performance at 300 mA g^{-1} and the CV curve at a scan rate of 0.3 mV s^{-1} (inset). c) XPS Se 3d spectra at different electrochemical states.

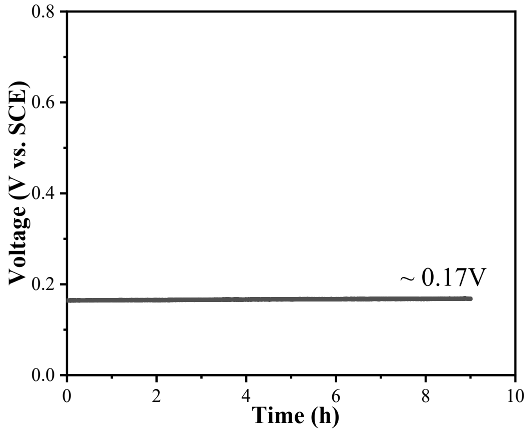

Figure 3.23 The open-circuit voltage of AC vs. SCE in aqueous electrolyte. It can be estimated to be approximately 3.28 V vs. Ca/Ca^{2+}.

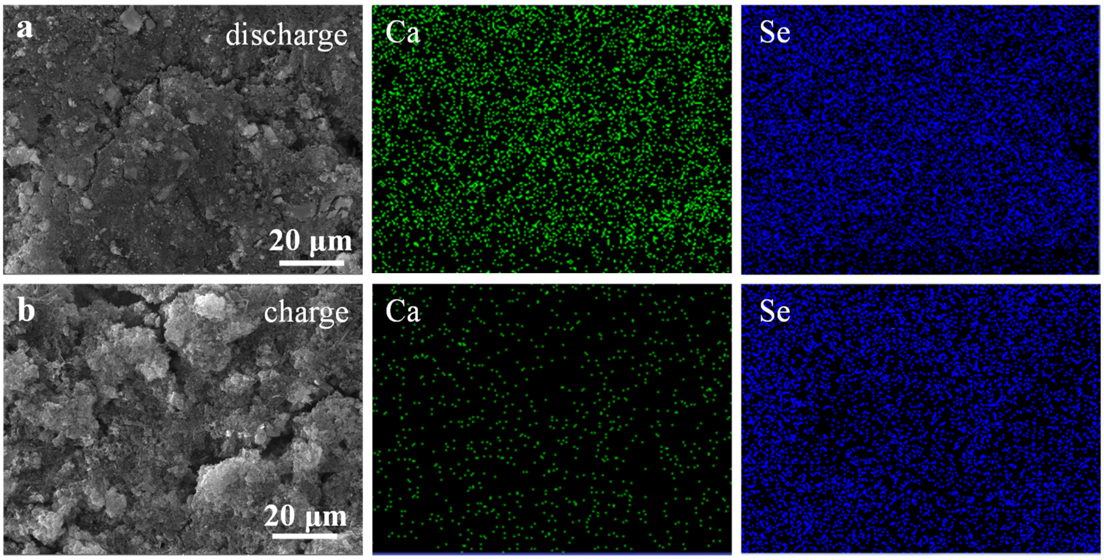

Figure 3.24 The SEM images and elemental mappings of Se/CMK-3 electrode at a) discharge state and b) charge state in aqueous system.

In order to certify the practicality of aqueous CIBs, a full cell with a $Ca_{0.3}[CuFe(CN)_6]_{0.66}\cdot 3.7H_2O$ ($Ca_{0.3}CuHCF$) cathode and a Se/CMK-3 anode is constructed and cycled in 6.25 M $Ca(TFSI)_2/H_2O$ electrolyte. Copper hexacyanoferrate (CuHCF) nanoparticles are synthesized by a facile co-precipitation method.[99] The SEM image and XRD pattern (Figure 3.25) reveal highly crystalline nanoparticles of CuHCF, consistent with previous reports.[99, 136] It delivers a specific capacity of 49 mAh g^{-1} at 100 mA g^{-1} in aqueous system (Figure 3.26). As shown in Figure 3.27, the GCD profiles of full cell have a plateau at about 1.4 V followed by a slope, giving rise to an average voltage of 1.1 V at 100 mA g^{-1}. After 50 cycles, the cell still delivers a specific capacity of 31 mAh g^{-1} based on the total mass of the active materials in the anode and cathode, corresponding to a specific energy of 34 Wh kg^{-1}. This value could be significantly boosted by exploring high-capacity and high-voltage cathodes in 6.25 M

$Ca(TFSI)_2/H_2O$ electrolyte, where a 2.3 V CIB is possible when coupling with a Se anode.

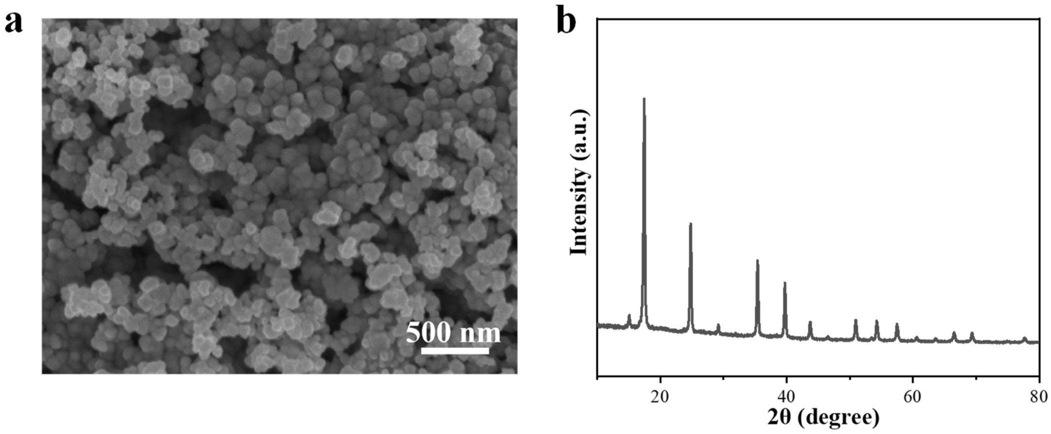

Figure 3.25 a) SEM image and b) XRD spectrum of CuHCF.

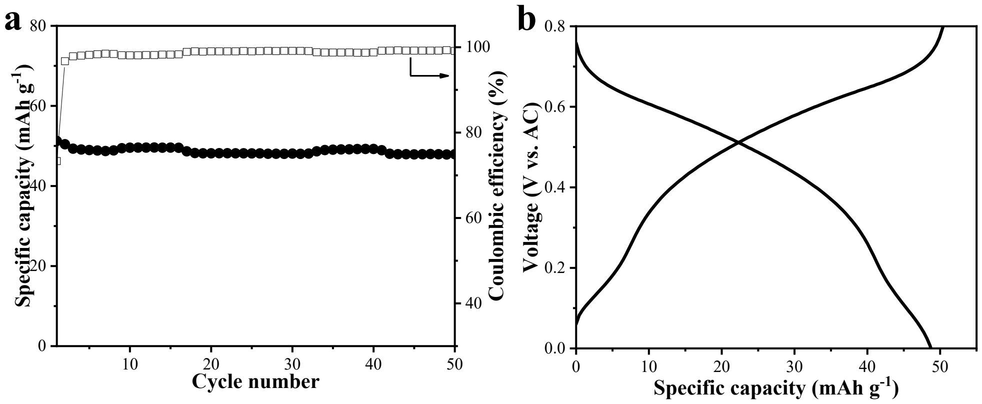

Figure 3.26 a) Cycling performance and b) GCD curves of CuHCF.

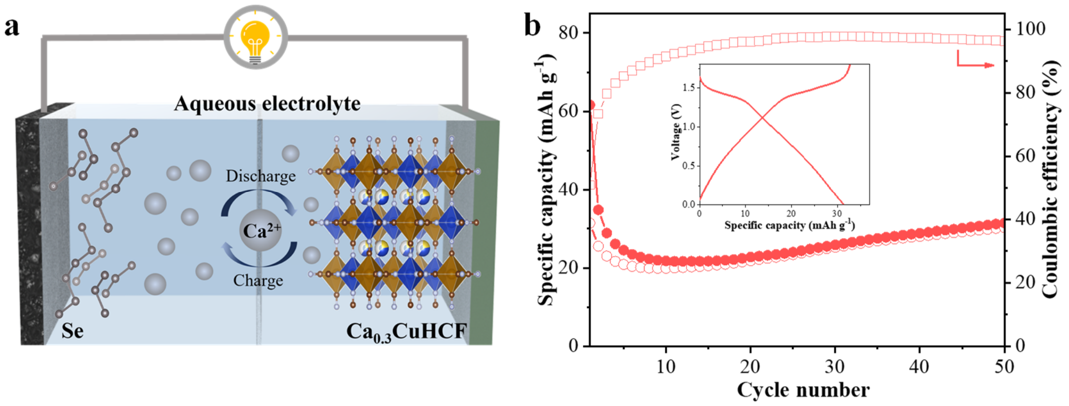

Figure 3.27 a) Schematic illustration of the aqueous full cell. b) The cycling performance and voltage profiles (inset) of $Ca_{0.3}CuHCF|Se/CMK-3$ battery at 100 mA g^{-1}. The capacity and current density are calculated based on the weight of both Se and $Ca_{0.3}CuHCF$ for the full cell.

3.3 Summary

We demonstrated a new conversion-type Se electrode for CIBs through complementary theoretical and experimental studies, which is compatible with both non-aqueous and aqueous electrolytes. In a non-aqueous system, the Se/CMK-3 electrode delivers a reversible capacity of 476 mAh g^{-1} at 50 mA g^{-1} with an average CE of 99.6%. The overall performance, considering the specific capacity and average voltage, is among the best compared with reported cathodes for CIBs. Mechanistic studies with SEM/EDS, XPS, UV-vis, and electrochemical methodologies reveal the stepwise conversion between Se^0 and Se^{2-}. Theoretical calculations indicate these intermediate phases most likely entail the $CaSe_4$ and Ca_2Se_5, whose detailed crystal structures have been unraveled for the first time. Furthermore, the Se/CMK-3 electrode also shows remarkable electrochemical activity in aqueous Ca electrolyte and exhibits a similar conversion mechanism to that in non-aqueous electrolytes. A 1.1 V-class aqueous CIB is demonstrated by coupling the Se/CMK-3 anode with a Cu-based Prussian blue cathode. This work presents an alternative direction in the exploration of high-capacity electrodes for both non-aqueous and aqueous CIBs.

Chapter 4. An advanced organic cathode for non-aqueous and aqueous calcium-based dual ion batteries

4.1 Introduction

In Chapter 3, we propose a high-capacity Se electrode and probe the reaction pathway in CIBs. The cyclic stability and operating voltage still require further improvement for building a practical CIB.

Ca-based dual ion batteries (CDIBs) employing an anion storage cathode are promising to circumvent the above issue since the anion insertion is characteristic of good reversibility, fast kinetics and high operating voltage.[171] Nevertheless, the anion insertion cathode has rarely been investigated in CDIBs systems except for graphite material. Tang's group demonstrates that the PF_6^- anion can be reversibly intercalated/de-intercalated into graphite cathode, giving an exceptional capacity of ~75 mAh g^{-1} for over 350 cycles.[32, 71, 98] The anion intercalation at high voltages (up to 5 V) in graphite cathode inevitably triggers the electrolyte decomposition, necessitating further improvements by designing stable cathode-electrolyte interphase. Organic compounds, such as PTPAn and polyaniline, are also attractive candidates for hosting anions. Their flexible framework allows reversible anion uptake at rapid kinetics without significant structural deformation.[172] Although PTPAn material has been applied as the cathode for alkali-metal batteries, a simple extrapolation from mono- to multiple-valence ion battery systems is not sufficient because of the distinct salt/solvent chemistry that also plays a crucial role.[173] This is evidenced by the brief comparison between Li and Ca systems (Figure 4.1). Furthermore, the detailed anion insertion chemistry in PTPAn remains largely unexplored.

Because of the poor reversibility of Ca metal and alloy anodes at this stage, graphite is almost the sole candidate accepting Ca^{2+} at an appropriate potential of 0.7 V with decent CE during cycling. Graphite anode is only possible through solvent co-intercalation, curbing the electrolytes to very limited candidates, such as G_4 and DMAc-derived ones.[37, 38] Considering the poor oxidation stability of DMAc, we focus on the G_4 solvent and investigate anion effect (i.e., BF_4^-, FSI^- and $TFSI^-$) on the electrochemical behavior in PTPAn cathode for building high-voltage and ultra-stable CDIBs. It is observed that electrochemical performance is highly related to anion types owing to distinct diffusion energy barriers and binding energies. The reversible redox process between C-N and positively charged $C=N^+$ during the charge/discharge process is responsible for the capturing/releasing of anions, as revealed by the complementary physicochemical characterizations and theoretical calculations. The graphite|PTPAn CDIB in $Ca(TFSI)_2$ electrolyte delivers a 2.45 V output voltage with a superior rate capability (50 C rate, 1 C=0.1 A g^{-1}) and long-term cycle stability (2000 cycles) at both 25 and 0 ^{o}C. Considering the appropriate redox potential of the PTPAn, we extend the study to the aqueous electrolytes by coupling with an organic anode, demonstrating the potential to build sustainable and high-safety aqueous CDIBs.

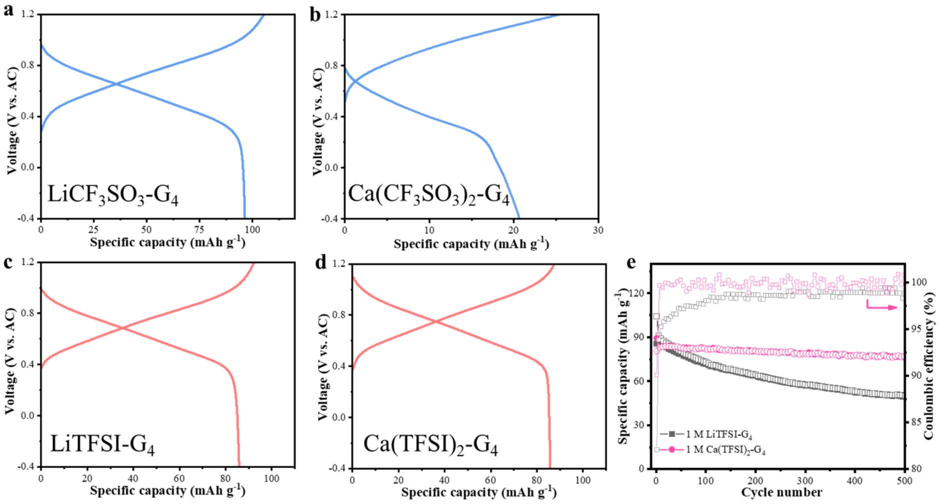

Figure 4.1 Voltage profiles of PTPAn in (a) 1 M $LiCF_3SO_3$-G_4, (b) 0.2 M $Ca(CF_3SO_3)_2$-G_4 (Here 0.2 M reaches the solubility limit of the Ca salt.), (c) 1 M LiTFSI-G_4 and (d) 1 M $Ca(TFSI)_2$-G_4. (e) Cycling performance of PTPAn in LiTFSI and $Ca(TFSI)_2$-based electrolytes. When $LiCF_3SO_3$ is employed as Li salt in G_4 solvent, PTPAn could deliver a reversible capacity of ~95 mAh g^{-1}. In contrast, PTPAn is incompatible with $Ca(CF_3SO_3)_2$, providing a capacity of merely 20 mAh g^{-1} with a large polarization. Such phenomenon may be due to the low dissociation degree of $Ca(CF_3SO_3)_2$ in the organic solvent caused by the strong interaction between Ca^{2+} and $CF_3SO_3^-$.[174, 175] On the contrary, PTPAn delivers comparable initial capacity when LiTFSI and $Ca(TFSI)_2$ are employed as salts in electrolytes, but it shows better cyclic stability in Ca-based system.

4.2 Results and discussion

4.2.1 The anion effect on the electrochemical performance of PTPAn

PTPAn is fabricated by the chemical oxidation polymerization of monomer TPA employing $FeCl_3$ as a Lewis acid catalyst in $CHCl_3$. The optimized quasi-2D PTPAn structures consist of TPA units that are linked with each other by para-substitution. In a TPA unit, three benzene rings are rotated in different planes, exhibiting a distorted structure instead of a flat 2D one, as revealed by the DFT structural relaxation with a conjugate gradient algorithm (Figure 4.2a). To further investigate the thermal stability of PTPAn system, the AIMD simulations with Nose´–Hoover thermostat for NVT ensemble are performed at 300 K with a time step of 2 fs and the total simulation time is set as 15 ps. No obvious structural reconstructions are noticed as the total energy of the system oscillates around the equilibrium values after the equilibrium time, indicating its stability at room temperature (Figure 4.2b). FTIR spectra detect a new peak at 819 cm^{-1} attributed to C-H out-of-plane vibration after the reaction, verifying the formation of 1,4-disubstituted benzene rings and the successful polymerization of TPA units (Figure 4.2c).[176] Raman spectroscopy is conducted to further examine the structure of PTPAn. The characteristic peaks of the mono-substituted rings of TPA at 1001 and 1033 cm^{-1} almost disappear after polymerization, indicating the formation of PTPAn (Figure 4.2d).[177] The polymer shows a porous structure consisting of microsized sheets (Figure 4.2e). XRD patterns with a broad peak at 18° (2θ) demonstrate the amorphous nature of as-synthesized PTPAn (Figure 4.2f), which is further confirmed by the electron diffraction pattern (Figure 4.2g, h).

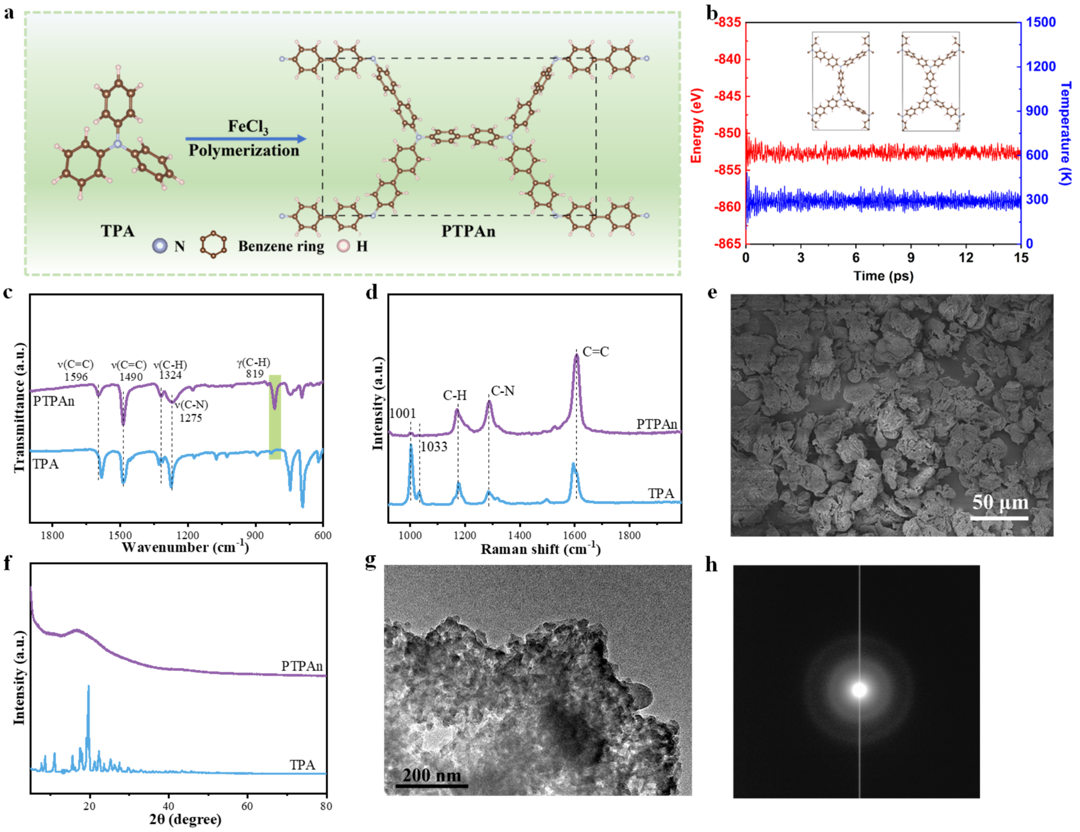

Figure 4.2 a) Schematic illustration of the polymerization process of TPA. b) Total temperature and energy as a function of time for PTPAn during the AIMD simulation (inset: the structure after 15 ps AIMD simulation. C, N, and H atoms are represented in brown, blue and pink, respectively). c) The FTIR spectra and d) Raman spectra of TPA and PTPAn. e) SEM image of the PTPAn powder. f) XRD spectra of TPA and PTPAn. g) TEM image and h) electron diffraction pattern of the PTPAn powder.

As an anion storage material, the anion categories would highly affect the storage behavior and electrochemical performance of the PTPAn. Three commercially available salts, i.e., $Ca(BF_4)_2$, $Ca(FSI)_2$ and $Ca(TFSI)_2$, are selected to investigate the anion effect because of their relatively high solubility that is essential to achieving high energy density in dual ion batteries. G_4 is selected as the solvent since the Ca^{2+}

intercalation in graphite anode is only possible with solvent co-intercalation under several special electrolytes, where the G_4-based one shows a wide electrochemical window for building high-voltage cells (Figure 4.3a).[37, 38] The performance of PTPAn in $Ca(BF_4)_2$, $Ca(FSI)_2$ and $Ca(TFSI)_2$ electrolytes are compared in Figure 4.3b. PTPAn delivers the best performance in $Ca(TFSI)_2$ electrolyte, i.e., capacity retention of 88% at 50 C (with respect to the value at 1 C), and 82% after 2000 cycles. By sharp contrast, $Ca(BF_4)_2$-based one only maintains 13% and 41% (after 300 cycles) under the same conditions (Figure 4.4-4.6). The voltage of AC counter electrode is calibrated by a Fc/Fc^+ redox couple in these electrolytes (Figure 4.7-4.9).[62]

The above observations prove the remarkable effect of anions and pose a question about which anion properties account for such a huge distinction. We first examine the electrolyte properties. The comparable ionic conductivities of three electrolytes indicate mass transfer has a negligible effect on the performance difference (Figure 4.3c, d). We then explore the diffusion difference of anions in PTPAn by measuring diffusion coefficients (galvanostatic intermittent titration technique (GITT)) and calculating diffusion energy barriers through DFT calculations (Figure 4.3e and 4.10). $TFSI^-$ anion delivers the highest diffusion coefficient and lowest energy barrier, which is possibly responsible for the superior rate performance of PTPAn in $Ca(TFSI)_2$-G_4 electrolyte. Besides the anion diffusion, the associating process between anions and PTPAn would also affect the kinetics. As shown in Figure 4.3f, the binding energies of $PTPAn^+{\cdot}TFSI^-$, $PTPAn^+{\cdot}FSI^-$, and $PTPAn^+{\cdot}BF_4^-$ are calculated to be -2.13, -2.32 and -3.71 eV, respectively. This indicates that the release of BF_4^- from the PTPAn is very tough compared with $TFSI^-$ and FSI^-, leading to poor cyclic stability.[178] In short, $TFSI^-$ anion enables the best performance owing to the fast diffusion process and low binding energy.

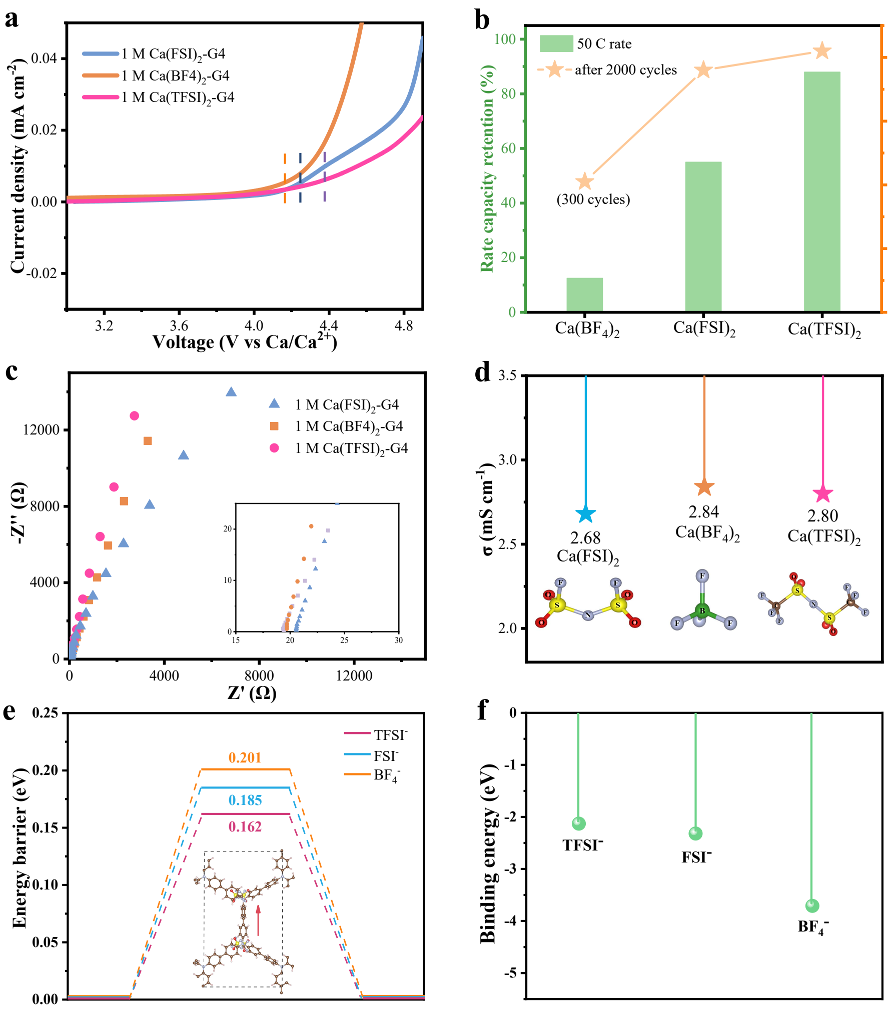

Figure 4.3 a) The LSV curves of three G_4-based electrolytes. The oxidation potential of $Ca(FSI)_2$, $Ca(BF_4)_2$ and $Ca(TFSI)_2$ electrolytes are 4.25, 4.25 and 4.35 V, respectively. b) The comparison on cycle life and rate performance of PTPAn in different electrolytes. c) The Nyquist plots of stainless-steel|stainless-steel cells and d) the comparison of ionic conductivity of three electrolytes. e) Calculated diffusion energy barriers of anions in PTPAn. f) Calculated binding energies between anions and PTPAn.

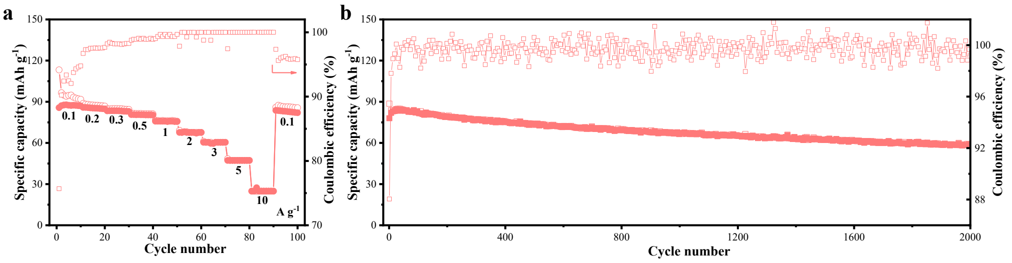

Figure 4.4 a) Rate performance and b) cycle stability of the PTPAn at 1 A g^{-1} in $Ca(FSI)_2$-G_4 electrolyte.

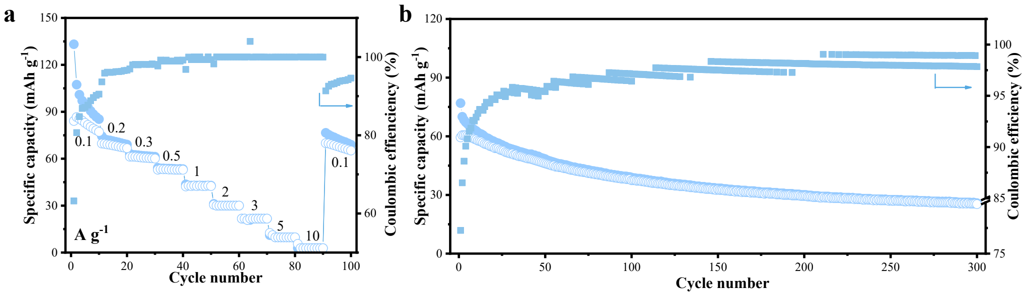

Figure 4.5 a) Rate performance and b) cycle stability of the PTPAn at 1 A g^{-1} in $Ca(BF_4)_2$-G_4 electrolyte.

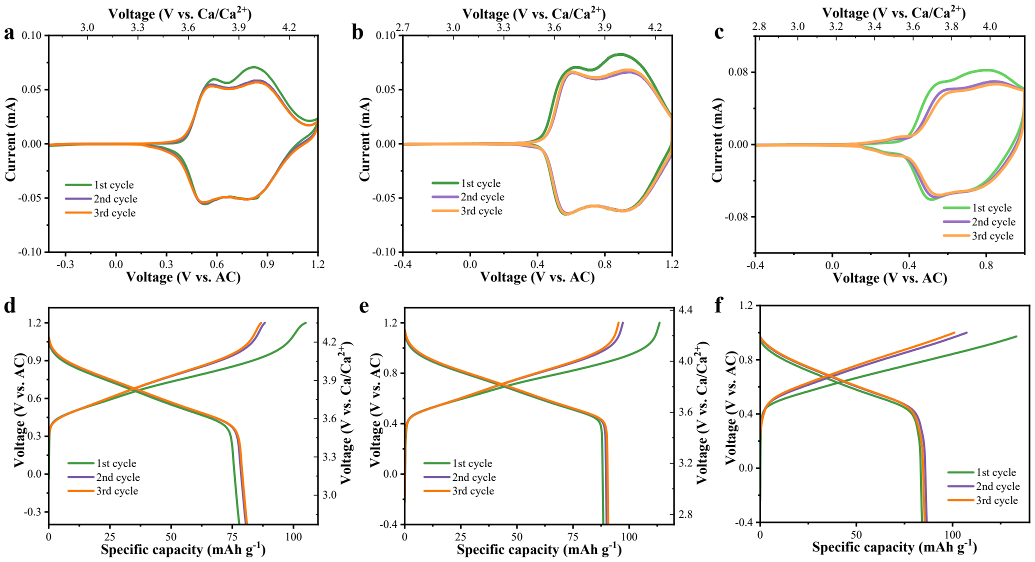

Figure 4.6 CV curves of PTPAn in a) $Ca(FSI)_2$, b) $Ca(TFSI)_2$ and c) $Ca(BF_4)_2$ electrolytes at 0.1 mV s^{-1}. GCD profiles of PTPAn in d) $Ca(FSI)_2$, e) $Ca(TFSI)_2$ and f) $Ca(BF_4)_2$ electrolytes at 0.1 A g^{-1}.

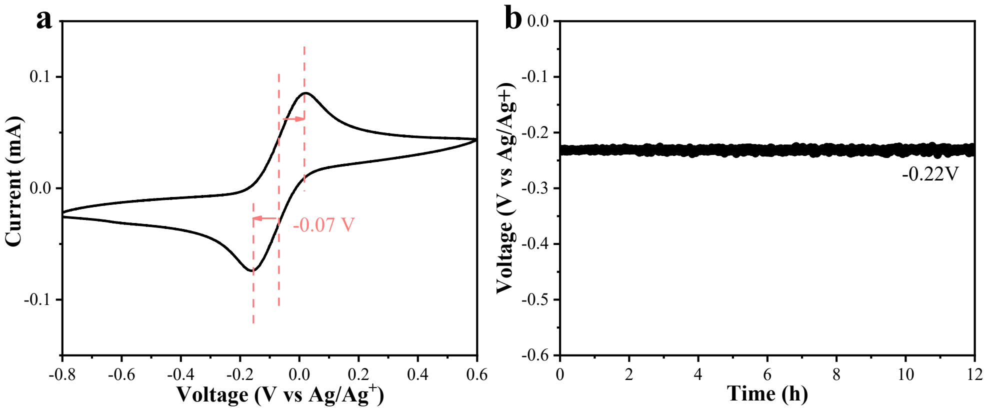

Figure 4.7 a) CV test of 5 mM ferrocene dissolved in 1 M Ca(TFSI)$_2$-G$_4$ electrolyte (the working and reference electrodes are Pt and Ag/Ag$^+$ (0.01 M AgNO$_3$ in 1 M Ca(TFSI)$_2$-G$_4$, respectively) at 10 mV s^{-1}. b) OCV of AC vs. Ag/Ag$^+$ reference electrode. The AC voltage can be estimated to be approximately 3.1 V vs. Ca/Ca^{2+} due to its OCV of -0.23 V.

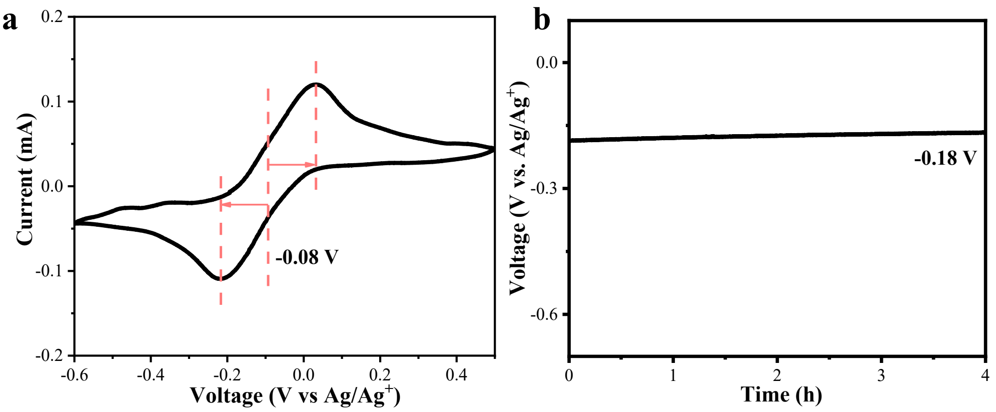

Figure 4.8 a) CV test of 5 mM ferrocene dissolved in 1 M Ca(FSI)$_2$-G$_4$ electrolyte (the working and reference electrodes are Pt and Ag/Ag$^+$ (0.01 M AgNO$_3$ in 1 M Ca(FSI)$_2$-G$_4$), respectively). The scan rate is 10 mV s^{-1}. b) OCV of AC vs. Ag/Ag$^+$ reference electrode. The AC voltage can be estimated to be approximately 3.17 V vs. Ca/Ca^{2+}.

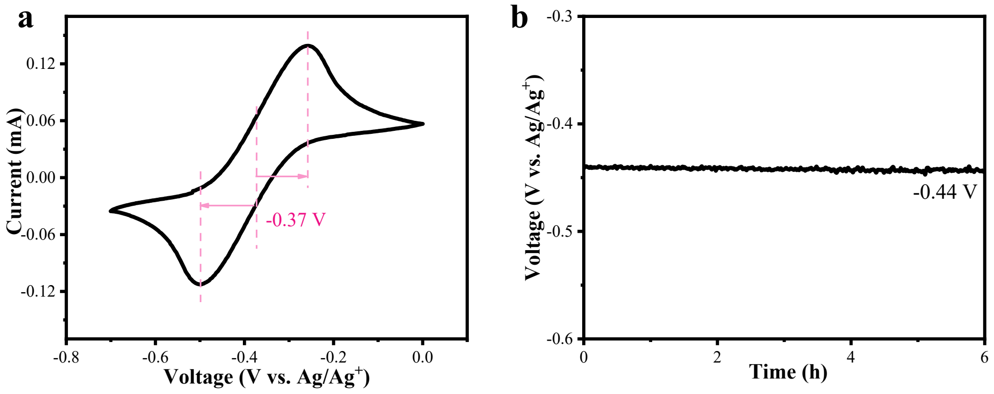

Figure 4.9 a) CV test of 5 mM ferrocene dissolved in 1 M $Ca(BF_4)_2$-G_4 electrolyte (the working and reference electrodes are Pt and Ag/Ag$^+$ (0.01 M $AgNO_3$ in 1 M $Ca(BF_4)_2$-G_4), respectively) at 10 mV s^{-1}. b) OCV of AC vs. Ag/Ag$^+$ reference electrode. The AC voltage can be estimated to be approximately 3.18 V vs. Ca/Ca^{2+}.

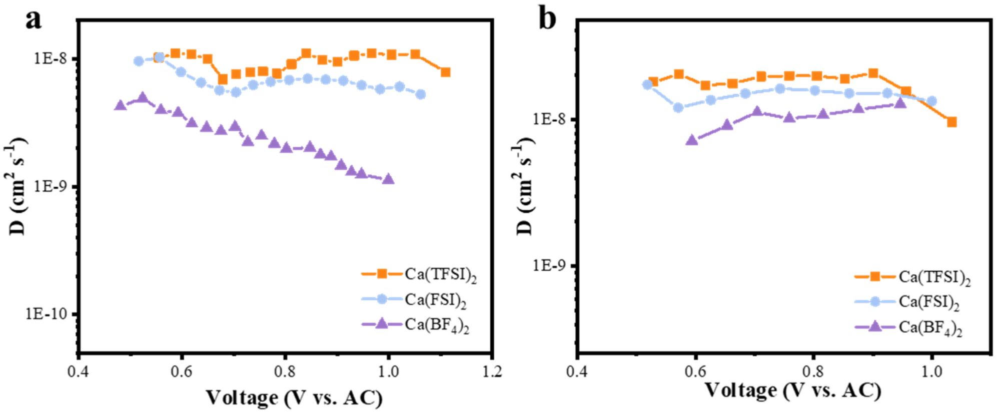

Figure 4.10 Diffusion coefficients of different anions in PTPAn during a) charge and b) discharge.

4.2.2 Electrochemical behavior of PTPAn in $Ca(TFSI)_2$-G_4 electrolyte

We then focus on $Ca(TFSI)_2$-G_4 electrolyte to systematically investigate the electrochemical behavior of PTPAn. The water content in the electrolyte is 41 ppm, as determined by the Karl-Fischer method. As shown in Figure 4.11a, the PTPAn cathode delivers a specific capacity of 88 mAh g^{-1} with an initial CE of 80% and rapid increase to 99%, indicating excellent reversibility. The slightly low initial CE should be due to the minor amount of electrolyte decomposition and irreversible $TFSI^-$ stored in PTPAn during the first cycle, as revealed by the S 2p XPS spectrum where a weak S signal presents in the fully discharged PTPAn (Figure 4.14b). Besides, other irreversible reactions may occur, including further electro-polymerization of the TPA oligomer.[179] The sloping voltage profiles of the PTPAn cathode exhibit an average discharge potential of 3.8 V vs. Ca/Ca^{2+} (Figure 4.11b). The rate performance of the PTPAn cathode is investigated by increasing the specific currents from 0.1 to an ultra-high value of 10 A g^{-1}, corresponding to about 100 C rate (Figure 4.11c). The discharge capacity remains almost the initial value without any loss from 0.1 to 1 A g^{-1}. When the specific current further increases to 2, 3, 5 and 10 A g^{-1}, the PTPAn delivers specific capacities of 86, 85, 77 and 55 mAh g^{-1}, respectively, suggesting a prominent rate performance and fast anion diffusion in the cathode.

The reaction kinetics of the PTPAn cathode is explored by CV measurement under different scan rates (v) from 0.2 to 1 mV s^{-1} (Figure 4.11d). The CV curves consist of two pairs of peaks at around 3.77/3.66 and 4.09/3.99 V vs. Ca/Ca^{2+}, corresponding to the $TFSI^-$ storage in the two N sites, which will be discussed later. The relationship between the peak current (i) and v is fitted with the formula of $i = av^b$, where a and b are constants for probing the reaction kinetics. A b value of around 0.5 reveals a diffusion-controlled process, while the b value approaching 1 signifies a pseudo-capacitive controlled behavior.[163] As shown in Figure 4.11e, the b values of all peaks are greater than 0.9, indicating a pseudo-capacitive characteristic that explains the fast diffusion of anions in the PTPAn cathode. The pseudo-capacitive contribution ratios of the PTPAn cathode increase from 93.6% to 97.0% with the scan rate rising from 0.2 to 1.0 mV s^{-1}, further reflecting that the pseudo-capacitive contribution holds the dominant position (Figure 4.11f). The long-term cyclic stability of the PTPAn cathode is verified under a large specific current of 1 A g^{-1} at 25 ^{o}C (Figure 4.11g). The electrode delivers a reversible capacity of 67 mAh g^{-1} after 2000 cycles, corresponding to a capacity retention of 82%, which is rarely achieved in other reported cathodes. It is a delight to find that a stable electrode/electrolyte interface is presented, as evidenced by the nearly unchanged interfacial resistance before and after cycling (Figure 4.11h).

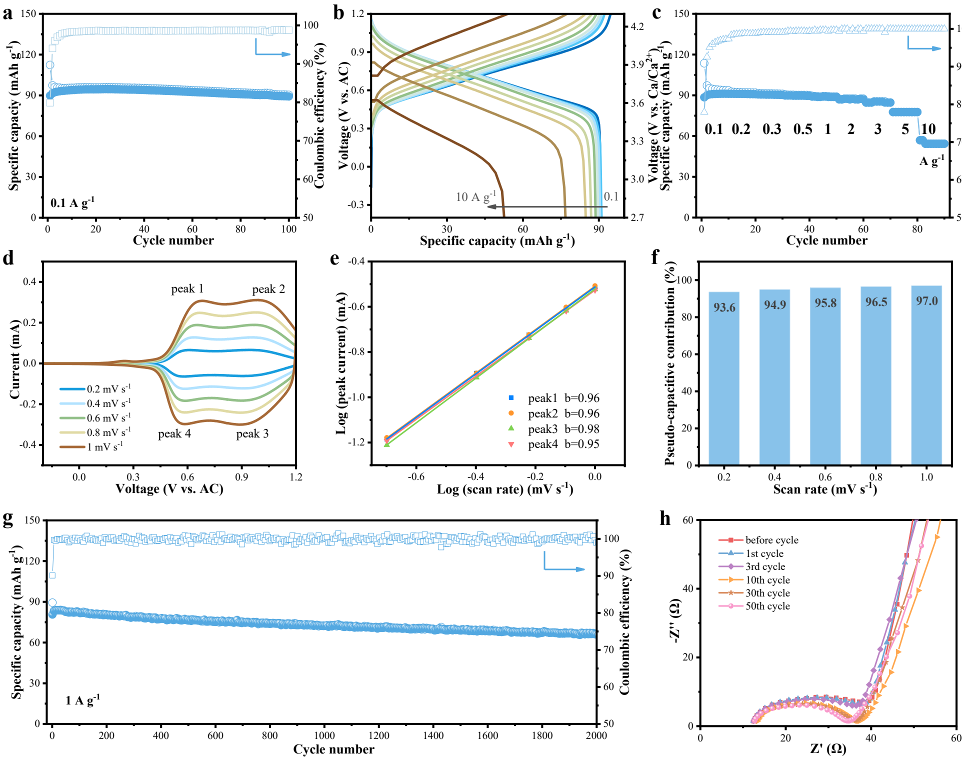

Figure 4.11 Electrochemical performance of PTPAn in Ca(TFSI)$_2$-G$_4$ electrolyte. a) Cycling performance at 0.1 A g^{-1}. b) Voltage profiles and c) rate performance under different specific currents. d) CV curves at various scan rates. e) The b-values fitted by the peak current and scan rate. f) The pseudo-capacitance contributions at multiple scan rates of the PTPAn cathode. g) Long-term cyclic stability at 25 °C. h) Nyquist plots of the PTPAn cathode under different cycles.

Realizing low-temperature operation for available inorganic cathodes remains challenging due to the sluggish kinetics caused by the low Ca^{2+} diffusion coefficient. On the contrary, the PTPAn cathode undergoes an anion-hosting reaction assuring fast reaction kinetics, which makes it possible for working at low temperatures. As shown in Figure 4.12a, the PTPAn cathode provides a comparable capacity and excellent stability at 0 °C as that at 25 °C. Excitingly, at -25 °C, it can still deliver a specific capacity of 80 mAh g^{-1} at 0.1 A g^{-1} and stably run for over 300 cycles. A superior cycling performance at 50 °C is also demonstrated, making the PTPAn a potential cathode for wide-temperature CDIBs. Figure 4.12b summarizes the performance of the state-of-the-art reported cathodes for Ca-based batteries, where the PTPAn cathode shows the best overall performance considering the cyclic stability, specific capacity, average voltage, and rate capability.

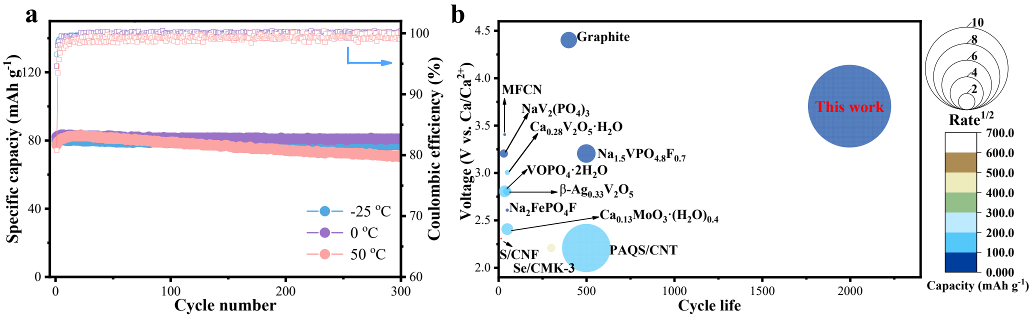

Figure 4.12 a) Long-term cyclic stability at -25, 0 and 50 °C. b) Comparison with reported cathodes in terms of cycle life, average discharge voltage, specific capacity and highest rate.

Considering the superior electrochemical performance of the PTPAn cathode, it is of great significance to investigate the underlying reaction mechanism. The electrostatic potential (ESP) distribution on a van der Waals surface can be used to estimate the active sites for electrochemical reactions. Based on Figure 4.13a, the ESP value at the N center exhibits the most positive distribution (isosurface level set as 55 eV/Å^3) in the whole system, which means that the nucleophiles are more likely to bind near the N center.[180] Ex-situ Raman spectra of the PTPAn cathode are collected at different discharge/charge states (Figure 4.13b). As shown in Figure 4.13c, three peaks at 1175, 1288 and 1606 cm^{-1} correspond to C-H bending vibration, C-N stretching and C=C ring stretching in the pristine PTPAn.[181] Upon charging, a new peak assigned to SO_2 asymmetric stretching in TFSI$^-$ anions appears at about 1320 cm^{-1}, which becomes more intense with the increase in the charging depth.[182] At the same time, the peak intensity at 1606 cm^{-1}, corresponding to C=C stretching of benzene ring, gradually decreases. A new peak located at 1570 cm^{-1} appears and grows with charging depth, which is associated with the formation of quinoid ring during charge process.[183] A reversible structural evolution is detected during discharging. The characteristic peak of TFSI$^-$ at 1320 cm^{-1} disappears and the peak at 1606 cm^{-1} recovers its original intensity when fully discharged owing to the release of TFSI$^-$. The observation is confirmed by ex-situ FTIR (Figure 4.13d). Specifically, increased intensities are detected for the new C=N$^+$ (1550 cm^{-1}) and SO_2 asymmetric vibration ($v_a SO_2$, 1349 cm^{-1}) during charging, revealing the formation of the charged C=N$^+$ and following combination with TFSI$^-$ in PTPAn.[184, 185] The characteristic peak of TFSI$^-$ almost vanish after fully discharging. These results imply a good reversibility of the PTPAn cathode. The existence of the reaction between TFSI$^-$ species and PTPAn is further proved by the solution-state and solid-state ^{19}F NMR spectroscopy, where the charged PTPAn cathode shows an obvious signal at about -79.2 ppm corresponding to TFSI$^-$ anion (Figure 4.14a).

We employ ex-situ XPS to further probe the redox chemistry of the PTPAn cathode at different electrochemical states. A peak at 400 eV corresponding to the C-N bond is detected in N 1s XPS spectrum of the initial PTPAn (Figure 4.13e). With continuous charging, a new peak with increased intensity is observed at 401.5 eV, assigned to the formation of the $TFSI^-/C=N^+$ compound. During discharging, this peak gradually becomes weaker and almost disappears due to the reduction of $C=N^+$ and the release of $TFSI^-$ from the PTPAn cathode. The S 2p and F 1s high-resolution spectra show a similar tendency, further confirming the $TFSI^-$ species in the PTPAn cathode (Figure 4.14). The $TFSI^-/C=N^+$ in N 1s and S 2p signals are also detected after surface etching for 100 s, indicating that the reaction not only occurs on the cathode surface (Figure 4.15). This observation agrees with the Brunauer-Emmett-Teller result indicating that PTPAn has a low surface area of 36 m^2 g^{-1}, making it hard to sustain a high capacity through surface reaction alone. The $TFSI^-$ capture/release could also be visualized by the elemental mapping of S, which is uniformly distributed on the charged electrode and almost disappears after discharging (Figure 4.16). To understand the detailed reaction pathway of the PTPAn, we calculate the reaction potential determined as the Gibbs free energy differences between captured anions and solvated anions. Based on our model, the theoretical voltages of the association between $TFSI^-$ anions and PTPAn are calculated to be 3.63 and 3.96 V, consistent with experimental GCD and dQ/dV curves (Figure 4.13f).

The reaction mechanism of the PTPAn cathode has been confirmed by the above theoretical calculation and experimental characterizations, which are based on the electron loss/acceptance of N active centers in the PTPAn structure (Figure 4.13g). $TFSI^-$ can be associated with the $C=N^+$ generated in PTPAn during the oxidation process and released in the following reduction process, accompanied by the reduction of C=N$^+$ back to C-N. The CV curves of the PTPAn deliver two pairs of peaks (Figure 4.11d). It is mainly associated with the formation of dimer by two TPA units in PTPAn. During the charging process, one of the TPA units first loses an electron to form a C=N$^+$. The neighboring TPA unit subsequently loses another electron at a higher potential owing to the conjugation effects, resulting in the two redox couples in the CV curves.[186, 187]

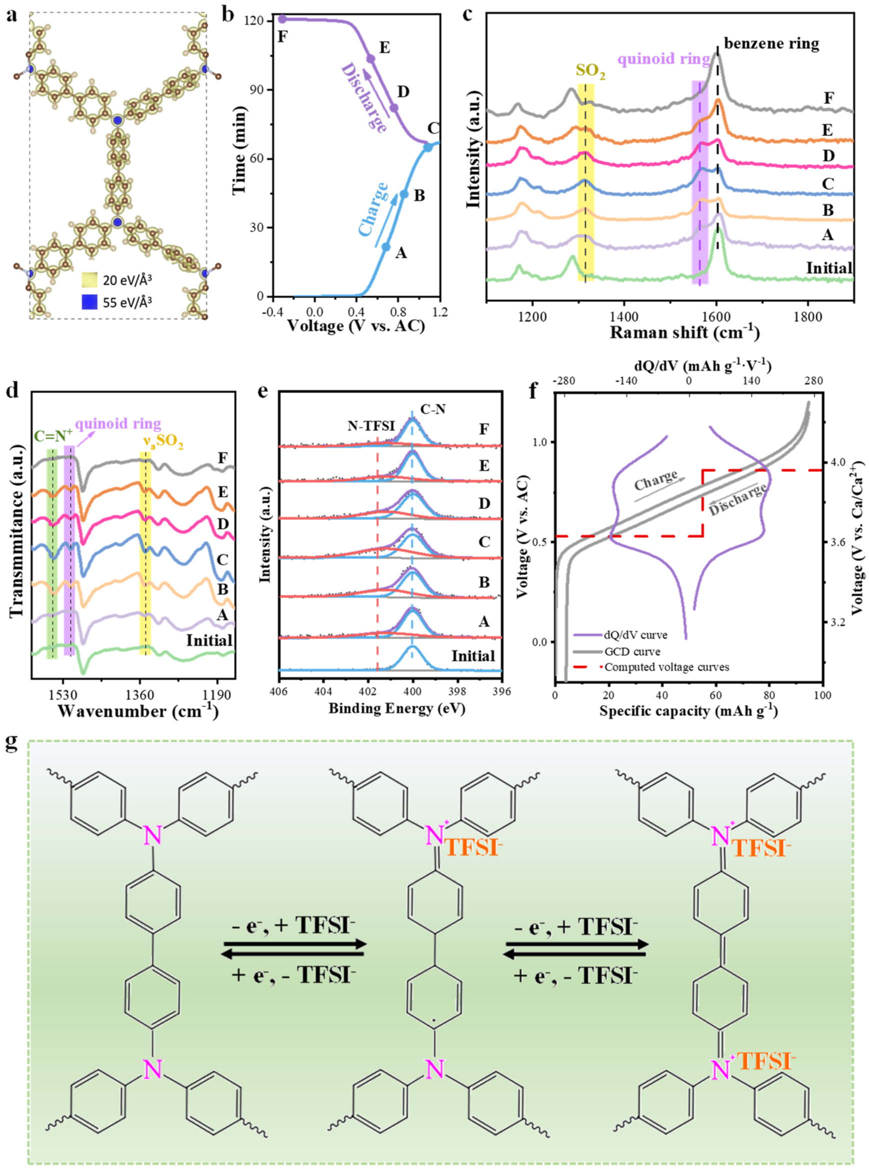

Figure 4.13 Reaction mechanism. a) Calculated ESP map of the PTPAn. Isosurface level: yellow (20 eV/Å^3), blue (55 eV/Å^3). b) The voltage profile in Ca(TFSI)$_2$-G$_4$ electrolyte. We mark the charge/discharge states at which the ex-situ FTIR patterns, Raman spectra and XPS patterns are collected. Ex-situ c) Raman spectra, d) FTIR spectra and e) N 1s XPS spectra at selected potentials. f) The calculated theoretical voltage, experimental GCD curve and dQ/dV curve of PTPAn with 1 M Ca(TFSI)$_2$-G$_4$ electrolyte. g) Reaction mechanism of PTPAn.

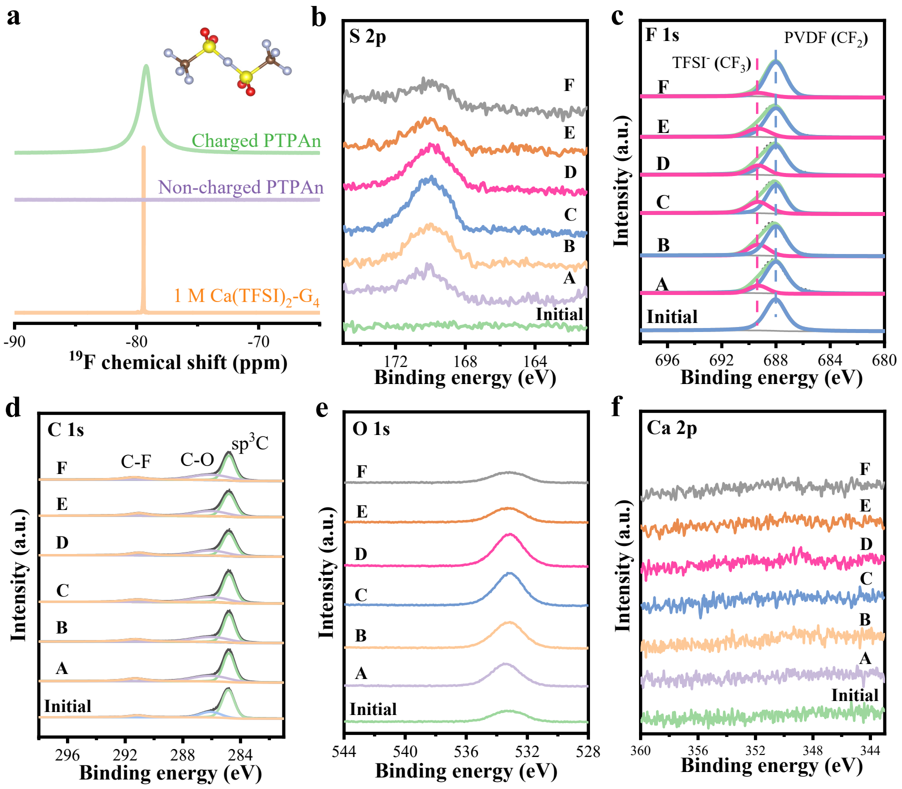

Figure 4.14 a) ^{19}F NMR spectra of non-charged, fully-charged PTPAn (washed with G_4 solvent), and 1 M $Ca(TFSI)_2$-G_4 electrolyte. Ex-situ b) S 2p c) F 1s d) C 1s e) O 1s and f) Ca 2p XPS spectra of the PTPAn cathode at different electrochemical states. The O 1s and F 1s spectra show a similar tendency. For the F 1s spectra, the initial peak at 688.0 eV corresponds to the PVDF in the pristine electrode. A new peak at 689.3 eV attributed to $TFSI^-$ anions appears and becomes intensive with continuous charging, which diminishes and almost disappears after discharging. The C 1s spectra of the electrode contain sp^{3}C, C-O and C-F peaks and do not change during the charging/discharging process. For the Ca 2p, there is no Ca signal in the electrode during charging/discharging. Therefore, the major activity would be the reversible $TFSI^-$ combination/extraction.

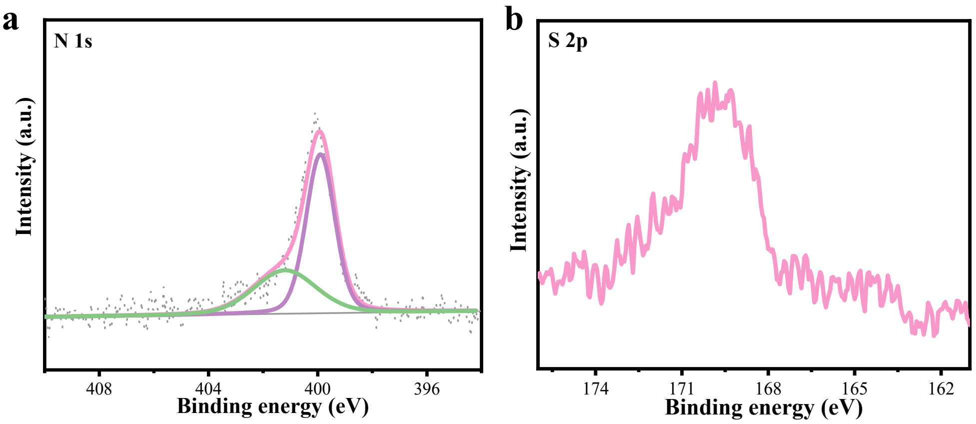

Figure 4.15 a) The N 1s and b) S 2p high-resolution XPS spectra of the charged PTPAn cathode after surface etching for 100 s.

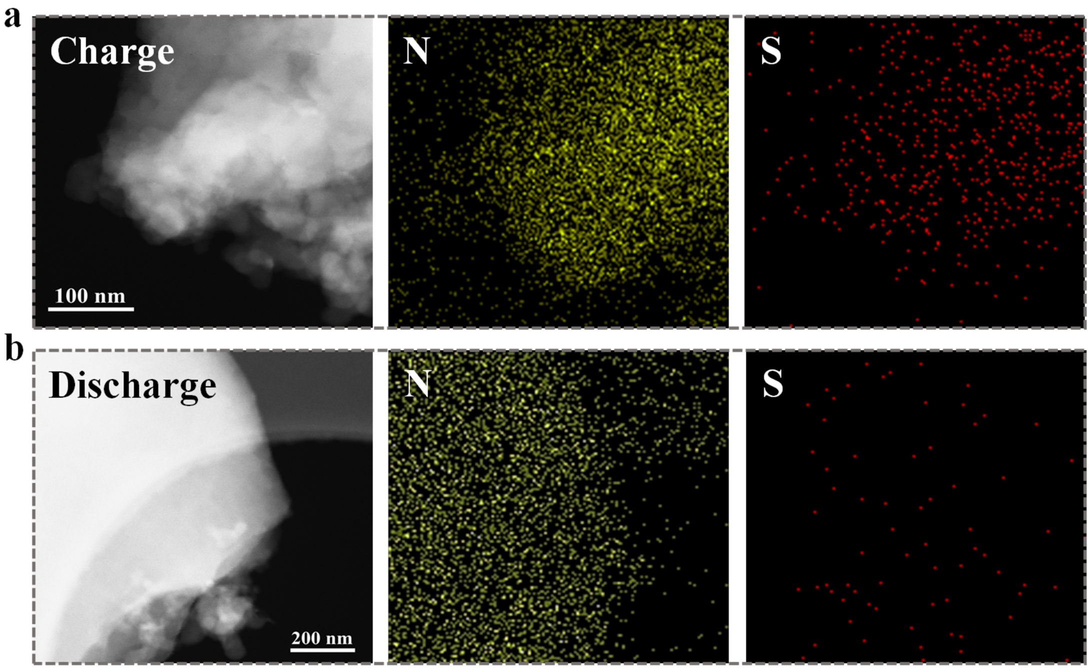

Figure 4.16 TEM images and corresponding EDS mappings of the PTPAn cathode after a) charge and b) discharge.

4.2.3 Construction of a full cell

To achieve a high-voltage battery system, a graphite|PTPAn CDIB is constructed due to the low potential (0.7 V vs. Ca/Ca^{2+}) of the graphite anode (Figure 4.17, 18a).[38] The voltage profiles of the PTPAn cathode, graphite anode and full cell are shown in Figure 4.18b. The full cell delivers an average voltage of 2.45 V with a reversible capacity of 72 mAh g^{-1} at 0.3 A g^{-1}. Besides, it presents a remarkable rate capability, as evidenced by high-capacity retention of 72% at 5 A g^{-1} (~50 C rate), corresponding to about a half-minute charge/discharge period (Figure 4.18c, d). Furthermore, such a full cell also exhibits excellent cycling performance at both 25 and 0 °C (Figure 4.18e), where reversible capacities of 44 and 40 mAh g^{-1} are achieved after 2000 cycles at a large specific current of 2 A g^{-1}, respectively. It is noted that there is a gradual capacity raising in the initial several cycles caused by the activation of the electrodes at 0 °C. The prominent performance is among the best compared to other full cells (Table 4.1), confirming the superiority of the graphite|PTPAn full cell with excellent rate capability and long cycle life.

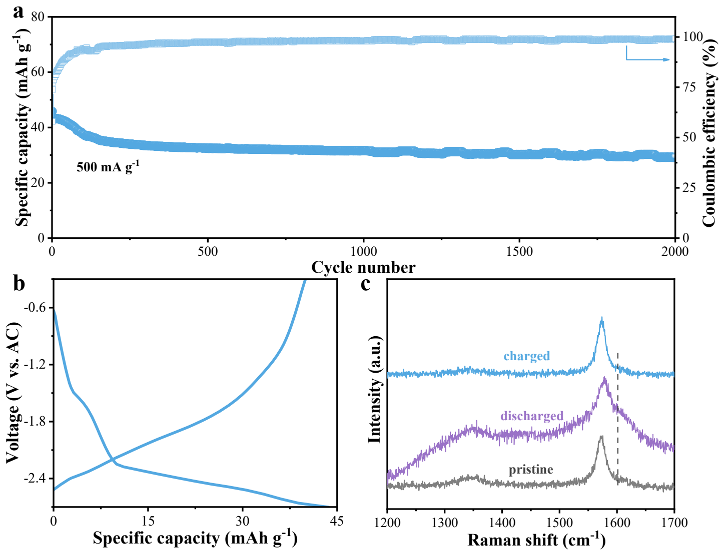

Figure 4.17 a) Cycling performance and b) corresponding voltage profiles of graphite at 0.5 A g^{-1} in Ca(TFSI)$_2$-G$_4$ electrolyte. c) Raman spectra of graphite at different electrochemical states.

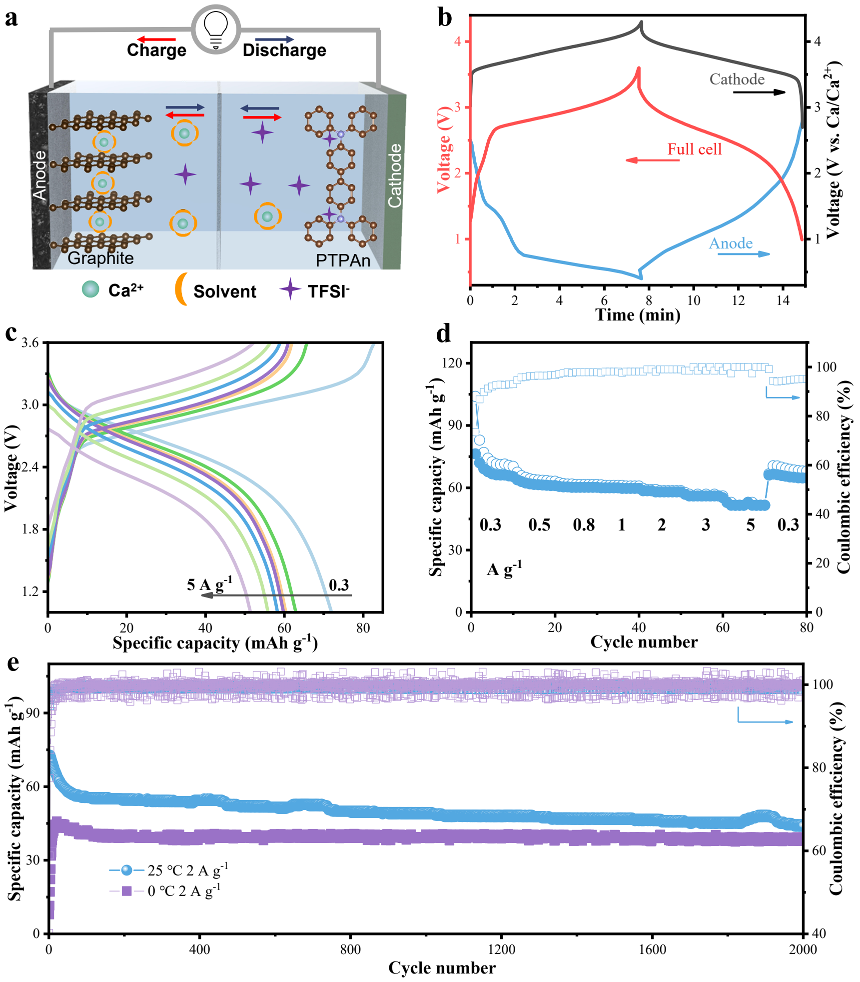

Figure 4.18 The graphite|PTPAn full cell in Ca(TFSI)$_2$-G$_4$ electrolyte. a) Schematic illustration of the full cell. b) Voltage profiles of the PTPAn, graphite vs. Ca/Ca^{2+} and the full cell. c) Voltage profiles and d) rate performance under different specific currents (0.3, 0.5, 0.8, 1, 2, 3 and 5 A g^{-1}). e) Cycling performance under 2 A g^{-1} at 25 and 0 °C. The capacities are based on the mass of the cathode and the N/P ratio is 1.1.

Table 4.1 Performance comparison with other calcium-based full cells.

Cell Type	Cell configuration (anode|cathode)	Electrolyte	Specific capacity (mAh g^{-1}@A g^{-1})	Cycle number	Rate performance (mAh g^{-1}/A g^{-1})
Calcium ion battery	Ca|N_1PVF_3[68]	0.5 M $Ca[B(hfip)_4]_2$/glyme	106@0.01	10	/
	Sn|MFCN[61]	0.2 M $Ca(PF_6)_2$ in EC/PC	80@-	35	/
	Ca|S[42]	0.25 M $Ca(B(hfip)_4)_2$/DME	760@-	15	/
Calcium-based dual ion battery	PTCDA/Graphite[71]	3.5 M $Ca(FSI)_2$ in EC/PC/DMC/EMC	75.4@0.1	350	38.5/0.3
	Sn|Graphite[32]	0.8 M $Ca(PF_6)_2$ in EC/PC/DMC/EMC	72@0.1	350	40/0.4
	MCMB|EG[98]	0.7 M $Ca(PF_6)_2$ in EC/DMC/EMC	66@0.2	300	55/0.33
	MCMB|KS6L[39]	0.5 M $[Ca:G_4]$ in IL	54@0.2	300	35/0.5
	Graphite|PTPAn	1 M $Ca(TFSI)_2$ in G_4	72@0.3	2000	52/5

4.2.4 Exploration in aqueous system

Considering the exceptional performance of the PTPAn cathode, we extend the research to the aqueous electrolytes for building high-safety aqueous Ca-based batteries, which attract rising attention recently.[97, 99, 107, 109] We first expand the ESW of the aqueous electrolyte to 2.2 V by using a high concentration electrolyte 6.25 M $Ca(TFSI)_2$-H_2O, which can satisfy the operation of the PTPAn cathode and PTCDI anode. The electrochemical behavior of the PTPAn is explored in half-cells with AC as the counter/reference electrode, which is calibrated to be ~3.28 V vs. Ca/Ca^{2+} using SCE in Chapter 3. As depicted in Figure 4.19a, the PTPAn cathode delivers similar discharge/charge profiles and comparable capacity (88 mAh g^{-1} at 0.3 A g^{-1}) with that in organic electrolytes, indicating the same reaction pathway in the two electrolytes. The PTPAn cathode provides appreciable specific capacities of 88, 86, 79, 70 and 54 mAh g^{-1} as specific current increases to 0.5, 1, 2, 3 and 5 A g^{-1}, respectively (Figure 4.19b). In addition, PTPAn also exhibits decent cyclic stability in aqueous electrolyte (Figure 4.20).

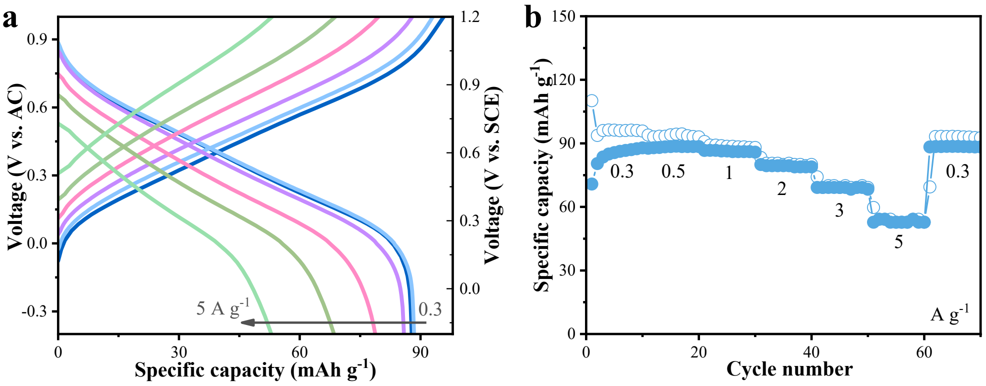

Figure 4.19 a) Voltage profiles and b) rate performance of PTPAn under different specific currents.

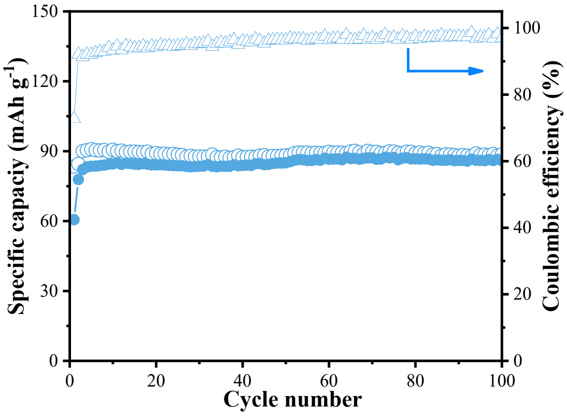

Figure 4.20 Cyclic performance of PTPAn cathode at 1 A g^{-1} in aqueous electrolyte.

To demonstrate its practical aspect, a PTCDI anode is employed to couple with the PTPAn cathode to fabricate an aqueous battery (Figure 4.21a). As shown in Figure 4.21b, the full cell provides a stable discharge capacity of 75 mAh g^{-1} with an output voltage of 0.75 V at a specific current of 0.1 A g^{-1}.

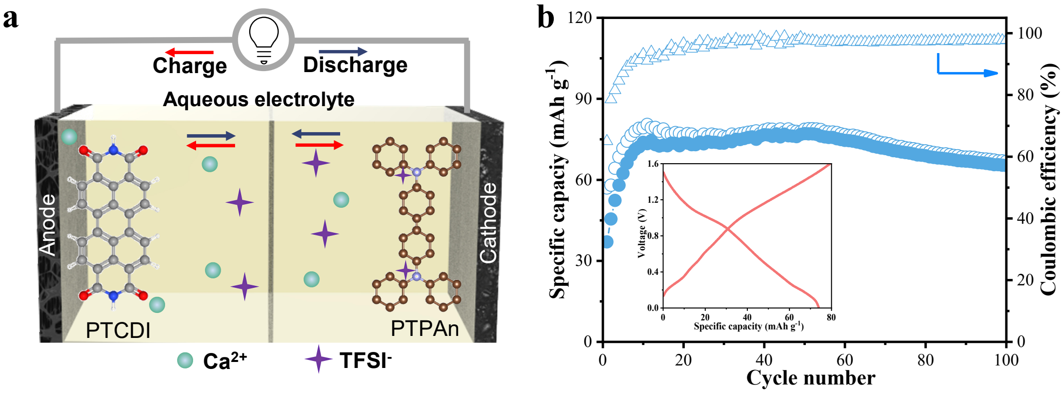

Figure 4.21 a) Schematic illustration of the PTCDI|PTPAn full cell. b) The cyclic performance and voltage profile (inset) of the full cell at 0.1 A g^{-1}.

4.3 Summary

In summary, an ultra-stable and high-rate CDIB is demonstrated with the assistance of an organic anion-hosting PTPAn cathode. Mechanistic studies with spectroscopic investigations and theoretical calculations confirm that the reaction mechanism of the PTPAn is based on the reversible redox process between C-N and C=N$^+$, accompanied by the combination/release of anions in the PTPAn. More importantly, the anion effect on the electrochemical performance of PTPAn are clarified. Owing to the rapid diffusion and moderate binding of TFSI$^-$ anion in/with PTPAn, Ca(TFSI)$_2$-G$_4$ electrolyte enables the best rate capability and cyclic stability, i.e., capacity retention of 88% at 50 C (with respect to the value at 1 C), and 82% after 2000 cycles. The assembled graphite|PTPAn full cell delivers a specific capacity of 72 mAh g^{-1} at 0.3 A g^{-1} with an output voltage of 2.45 V. It also provides an excellent rate capability (capacity retention of 72% at 5 A g^{-1} vs. the capacity at 0.3 A g^{-1}) and long cycle life (2000 cycles). Furthermore, the PTPAn cathode shows outstanding electrochemical performance in the aqueous electrolyte. A high-safety all-organic aqueous CDIB is demonstrated by coupling with a PTCDI anode. This work provides an alternative pathway toward high-rate and ultra-stable Ca-based batteries and a feasible direction to regulate the performance of CDIBs, which would also benefit other metal ion batteries relying on anion storage.

Chapter 5. Synergistic proton and Ca^{2+} insertion boosting aqueous calcium-ion batteries

5.1 Introduction

In Chapter 4, a PTCDI anode is employed to couple with PTPAn cathode and construct an aqueous full cell. It is also employed as a counter electrode in organic electrolyte.[25] We note that it shows a distinct electrochemical behavior in the organic and aqueous electrolytes, due possibly to the presence of H^+ in the latter.[188] It is worth noting that protons (H^+) could also serve as charge carriers in the aqueous system, as demonstrated in Zn-ion batteries.[189-193] Benefiting from the Grotthuss conduction mechanism, H^+ can move rapidly in aqueous electrolyte through the formation/breakage of the hydrogen bond.[194-197] Nevertheless, since the H^+ insertion may compete with the Ca^{2+}, whether H^+ charge carrier brings about a positive or negative impact on the cyclic stability and rate capability of CIBs remains unclear. Therefore, we adopt the PTCDI as a model electrode in this work to explore the H^+ insertion behavior and the impact on the capacity and stability of Ca^{2+} storage. Delightedly, we observe the simultaneous H^+ and Ca^{2+} insertion/extraction in aqueous electrolyte, leading to an increased specific capacity from 68 to 113 mAh g^{-1} and rate retention from 74% to 92% at a large current density of 2 A g^{-1}. Such an enhancement could be well extended to magnesium-ion batteries (MIBs), providing a new avenue for boosting the energy of aqueous divalent ion batteries.

5.2 Results and discussion

5.2.1 Electrochemical behavior of PTCDI in non-aqueous and aqueous electrolytes

The electrochemical performance of PTCDI is first evaluated in organic and aqueous CIBs. Figure 5.1a presents the charge/discharge curves of PTCDI in 1 M $Ca(TFSI)_2$-EC/PC and H_2O electrolytes at 0.2 A g^{-1}. The voltage of AC counter electrode is around ~3.05 V in organic electrolyte. In EC/PC-based electrolyte, PTCDI anode shows a sloping voltage profile with a specific capacity of 68 mAh g^{-1} and discharge average voltage of 2.38 V vs. Ca/Ca^{2+}, while a capacity of 113 mAh g^{-1} and 2.3 V average voltage are obtained in aqueous electrolyte. It is worth noting that PTCDI delivers distinct voltage profiles in two electrolytes, which is confirmed in the CV curves (Figure 5.2). Besides, a superior rate performance is realized in aqueous electrolyte. Specifically, the PTCDI anode delivers a 74% capacity of that at 0.2 A g^{-1} under a large current density of 2 A g^{-1} in non-aqueous electrolyte (Figure 5.1b). In comparison, it shows a much higher capacity retention of 92% under 2 A g^{-1} in aqueous electrolyte (Figure 5.1c). Even under a challenging current density of 20 A g^{-1}, it still sustains a decent discharge capacity of 84 mAh g^{-1} in 1 M $Ca(TFSI)_2$-H_2O electrolyte.

Such a tremendous disparity in the rate capability of PTCDI under different electrolytes may be ascribed to ionic diffusion kinetics. We calculate the ionic coefficients in the non-aqueous and aqueous electrolytes by the GITT.[198] Indeed, the diffusivity in aqueous electrolyte is an order of magnitude higher than that in organic counterpart (Figure 5.1d, 5.3). We also examine the cyclic stability of PTCDI at a current density of 1 A g^{-1} in these two electrolytes. Impressively, H_2O-based electrolyte enables a slight capacity decay after 3000 cycles with a capacity retention of 97%. It significantly outperforms the performance in the organic system, which shows a gradual capacity decline with 78% retention after 3000 cycles (Figure 5.1e). A capacity increase process is observed in the initial hundred cycles in organic electrolyte. It may relate to the large energy barrier and slow kinetics of Ca^{2+} insertion in PTCDI, requiring long activation cycles. On the contrary, such an activation process disappears in aqueous electrolyte. Moreover, the PTCDI anode provides comparable capacities and cyclic life at 0 °C as that at room temperature (Figure 5.4) because of the excellent kinetics.

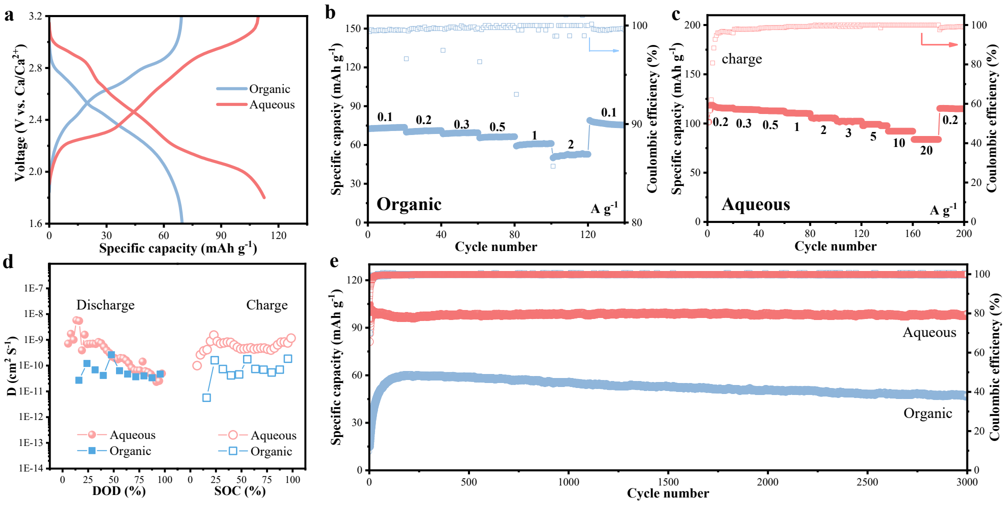

Figure 5.1 Electrochemical performance of PTCDI in CIBs. a) Voltage profiles in 1 M $Ca(TFSI)_2$-H_2O and 1 M $Ca(TFSI)_2$-EC/PC electrolytes. b) Rate performance in organic electrolyte. The cell is pre-cycled at 0.1 A g^{-1} for 100 cycles to fully activate the electrode. c) Rate performance in aqueous electrolyte without activation. d) Charger diffusivity and e) cyclic performance in organic and aqueous electrolytes at 1 A g^{-1}.

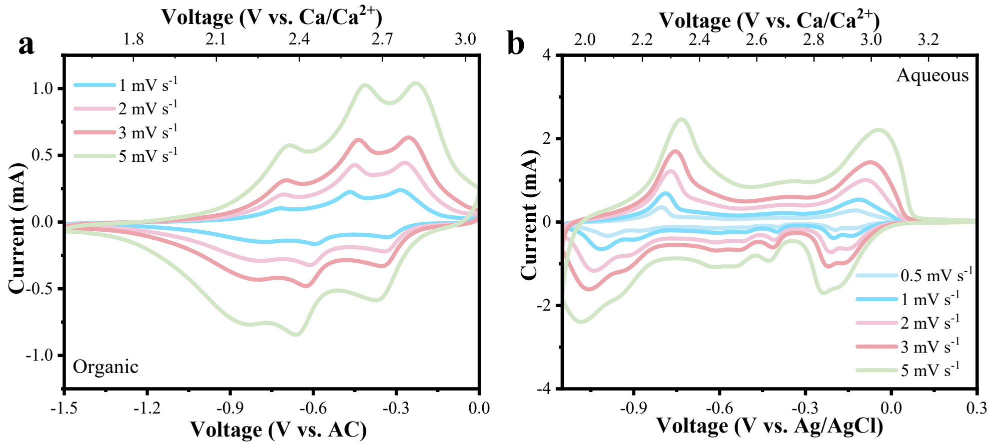

Figure 5.2 CV curves of PTCDI anode in a) organic and b) aqueous electrolytes at various scan rates.

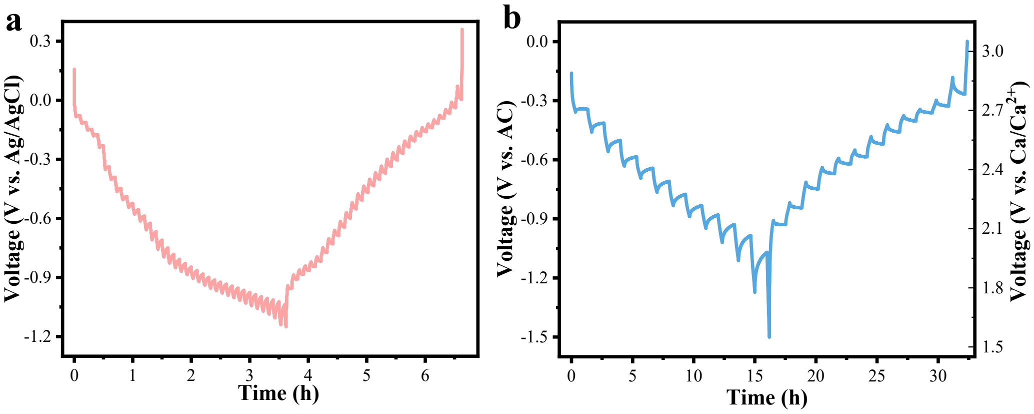

Figure 5.3 GITT curves of PTCDI anode in a) aqueous and b) organic Ca-based electrolytes.

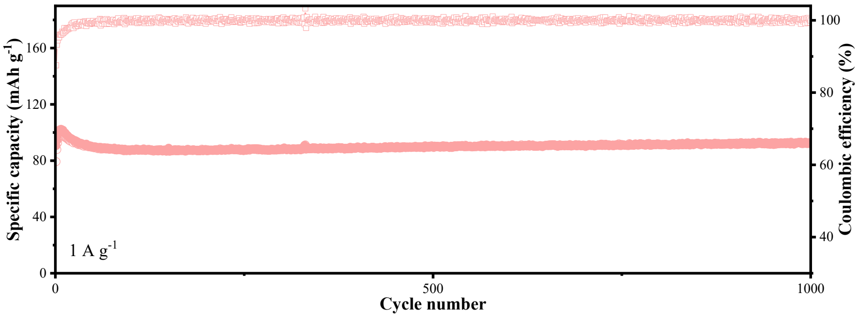

Figure 5.4 Cycling performance of PTCDI anode at 0 °C.

5.2.2 Synergistic H^+/Ca^{2+} co-storage mechanism and kinetics

Knowing PTCDI anode exhibits totally distinct electrochemical behavior and performance in the two electrolytes, we then explore the underlying mechanisms. For an aqueous system, protons can act as potential charge carriers due to their small size.[190, 191, 195] It is conjectured that the extra redox peaks of PTCDI anode originate from H^+ insertion in aqueous electrolyte. We collect the CV curves of PTCDI anode in the acid electrolyte (i.e., 0.1 M HTFSI in H_2O), without the presence of Ca^{2+}, to examine whether the H^+ insertion exists. As shown in Figure 5.5a, three reduction peaks at 0.06, -0.37 and -0.64 V vs. Ag/AgCl are obtained in the HTFSI solution, proving the capability of storing H^+ in PTCDI. Based on the Nernst equation, the CV curve in a pH=5.6 solution (the same pH value with 1 M $Ca(TFSI)_2$-H_2O) is obtained by shifting -0.27 V of the curve in HTFSI solution (Equation 5.1).

$$\triangle\varphi=0.059\lg\frac{[H^+]_1}{[H^+]_2}=0.059\lg\frac{10^{-1}}{10^{-5.6}}=0.27\ \text{V} \qquad \text{(Equation 5.1)}$$

The peak positions after shifting can partially overlap with the reduction peaks in $Ca(TFSI)_2$-H_2O electrolyte, suggesting the H^+ insertion in the PTCDI. H^+ insertion is further explored by ^1H solid-state NMR of the discharged PTCDI anode (Figure 5.5b). After discharging, an additional peak appears, indicating the insertion of H^+ into PTCDI during the discharge process.[199, 200]

Besides H^+ insertion in PTCDI, Ca^{2+} also involve in the charge storage process, as observed in Ca 2p XPS spectra under different states (Figure 5.6a). Ca signals appear after fully discharge and almost vanish after full charge. In addition, we examine the Ca^{2+} content in the sample by ICP-OES, which is used to calculate the capacity contribution from Ca^{2+} (Table 5.1 and Figure 5.5c). At the full discharge state, the capacity provided by H^+ is around 46 mAh g^{-1}. The above observations demonstrate simultaneous Ca^{2+} and H^+ insertion in the PTCDI anode under aqueous electrolyte, where H^+ storage contributes around 41% of the total capacity.

The reaction mechanisms of PTCDI during cycling are probed by ex-situ FTIR and XPS under selected states (Figure 5.6). The stretching vibration of carbonyl group at ~1672 cm^{-1} gradually weakens during discharge, while a new peak at ~1050 cm^{-1} assigned to $C\text{-}O^-$ is detected and becomes more intense.[201] During the following charge process, the peak of $C\text{-}O^-$ almost disappears and the C=O peak returns to its initial intensity (Figure 5.6d). This evolution indicates the reversible conversion reaction between C=O and $C\text{-}O^-$ is responsible for the charge storage. The observation is confirmed by O 1s XPS spectra (Figure 5.6b). The peak at 531.3 eV shifts to a higher binding energy of 532 eV after discharge and returns to its initial position after charge, indicating the highly reversible reduction/oxidation of C=O bond.

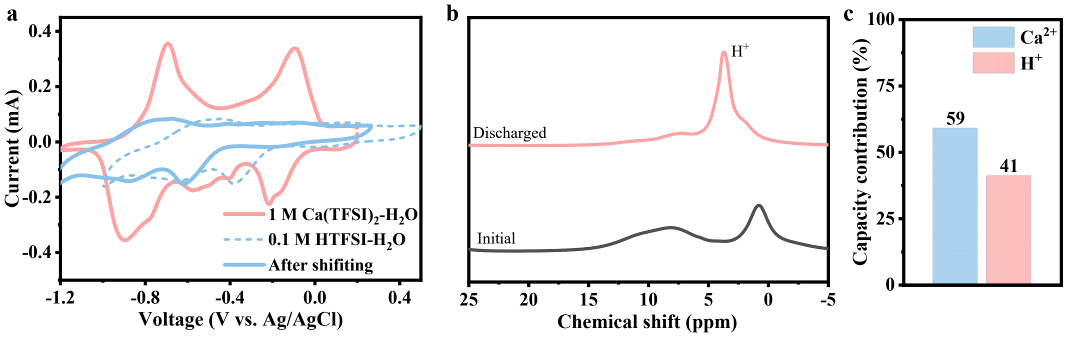

Figure 5.5 a) CV curves of PTCDI anode in 1 M $Ca(TFSI)_2\text{-}H_2O$ and 0.1 M HTFSI-H_2O at 1 mV s^{-1}. b) ^1H solid-state NMR spectra of pristine and discharged PTCDI. c) Calculated H^+/Ca^{2+} capacity contribution.

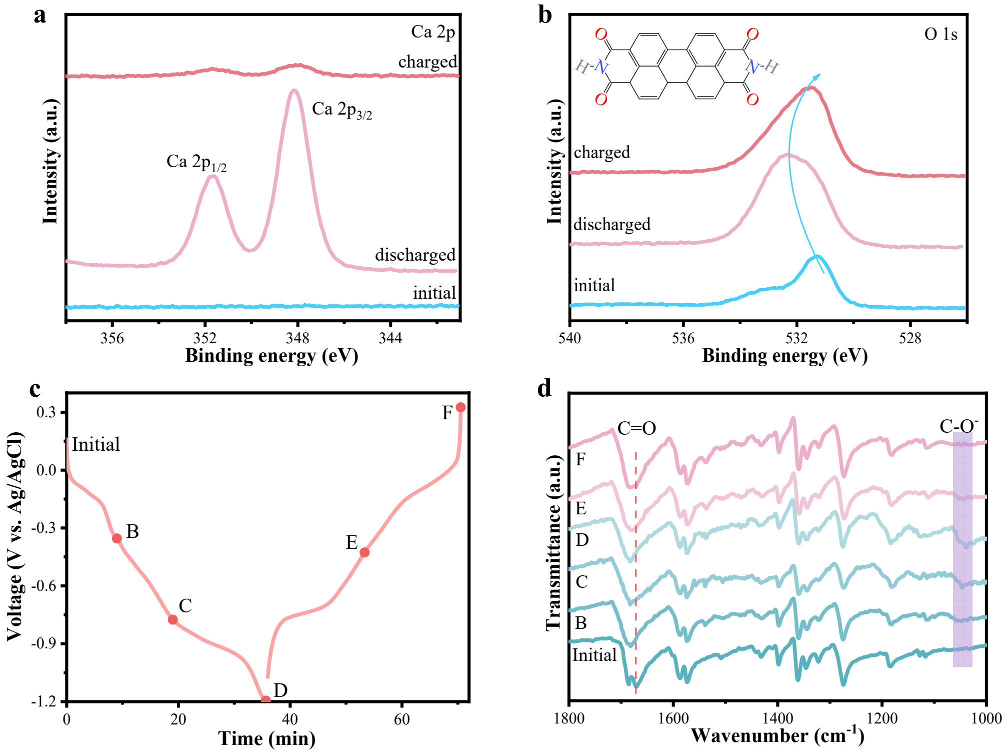

Figure 5.6 a) Ca 2p and b) O 1s XPS spectra of the PTCDI anode (Inset: structure of PTCDI). c) Voltage profiles of the PTCDI anode at 0.2 A g^{-1}. We mark the charge/discharge states at which the ex-situ FTIR patterns are collected. d) Ex-situ FTIR spectra.

Table 5.1 The Ca-content in PTCDI and calculated Ca^{2+}/H^+ contribution in aqueous CIBs using ICP-OES.

Electrolyte	Organic 1 M $Ca(TFSI)_2$-EC/PC	Aqueous 1 M $Ca(TFSI)_2$-H_2O
Sample	Fully discharge	Fully discharge
Ca content (%)	1.74	1.73
Discharge capacity (mAh g^{-1})	67	113
Ca^{2+} capacity contribution (mAh g^{-1})	67	67
Ca^{2+} capacity contribution (%)	100%	59%
H^+ capacity contribution (%)	0%	41%

DFT simulations are conducted to further elucidate the H^+/Ca^{2+} storage in PTCDI. Based on the electrostatic interaction, the more negative sites in ESP map stand for the electrophilic center and are highly active for cations uptake.[202] The ESP map of PTCDI is depicted in Figure 5.7. The C=O groups region colored in blue shows the minimal ESP values in PTCDI, suggesting that C=O bonds are potential electrophilic centers to store cations (H^+ or Ca^{2+}), consistent with the ex-situ FTIR and XPS observations.

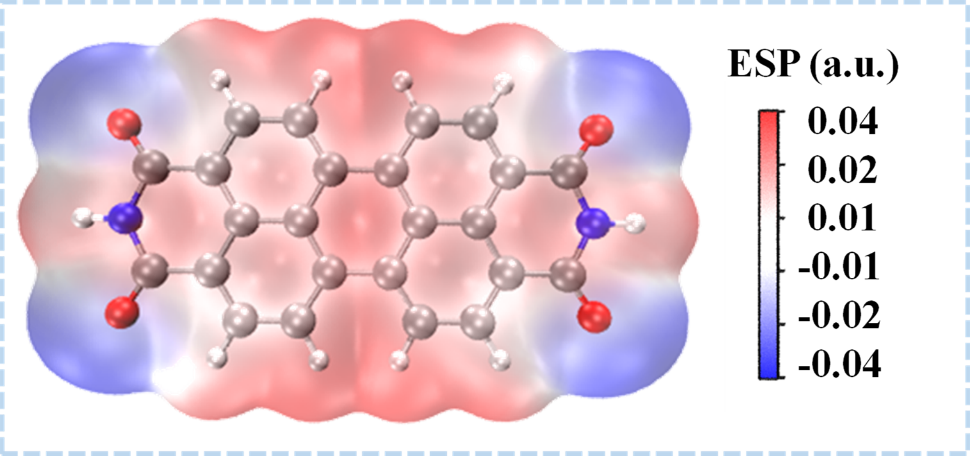

Figure 5.7 Calculated ESP map of PTCDI.

A systematic investigation is performed to calculate the binding energy (ΔE) of various possible geometrical configurations that uptake H^+ and Ca^{2+} step-by-step (Figure 5.8-11). The PTCDI incorporates one Ca^{2+} initially with the strongest binding strength of -4.20 eV in the two-electron reaction. It absorbs two H^+ in the subsequent reaction with ΔE values of -3.64 eV and -3.60 eV, respectively. It is concluded that PTCDI demonstrates a mixed H^+/Ca^{2+}-insertion process and results in the optimized insertion configuration in Figure 5.12.

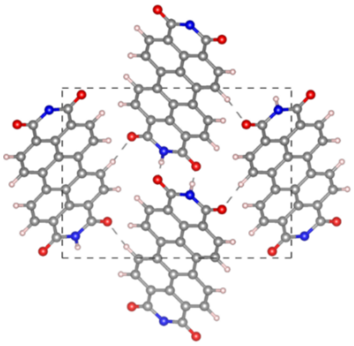

Figure 5.8 Optimized structure of PTCDI. C, N, H and O atoms are represented in grey, blue, pink, and red, respectively.

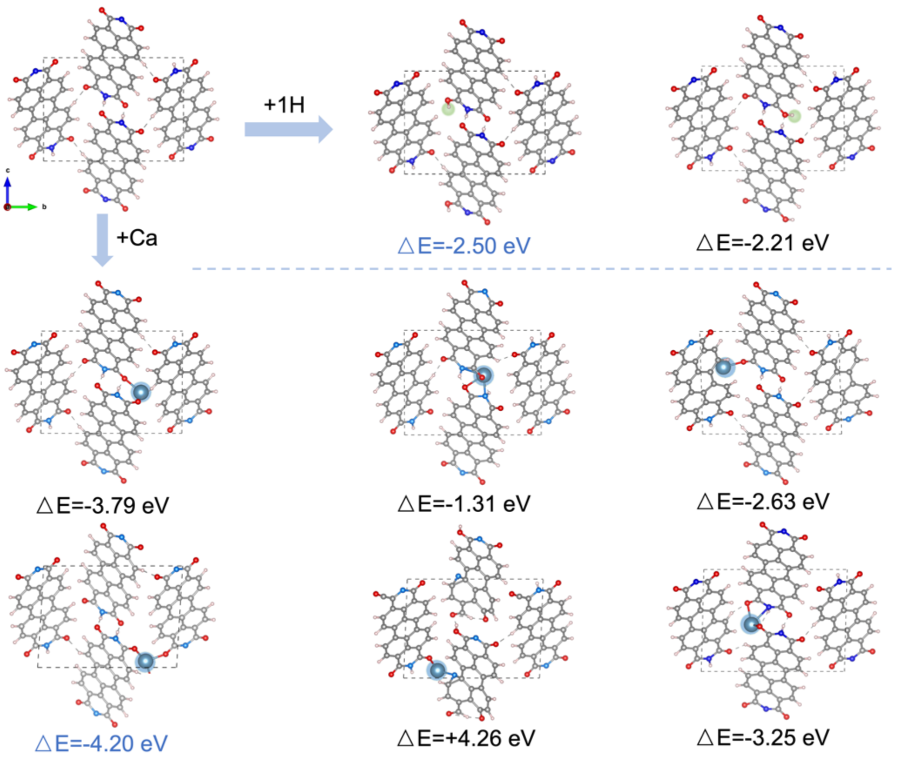

Figure 5.9 Possible geometrical configurations and calculated ΔE for unit cell of different PTCDI-H and PTCDI-Ca intercalation structures.

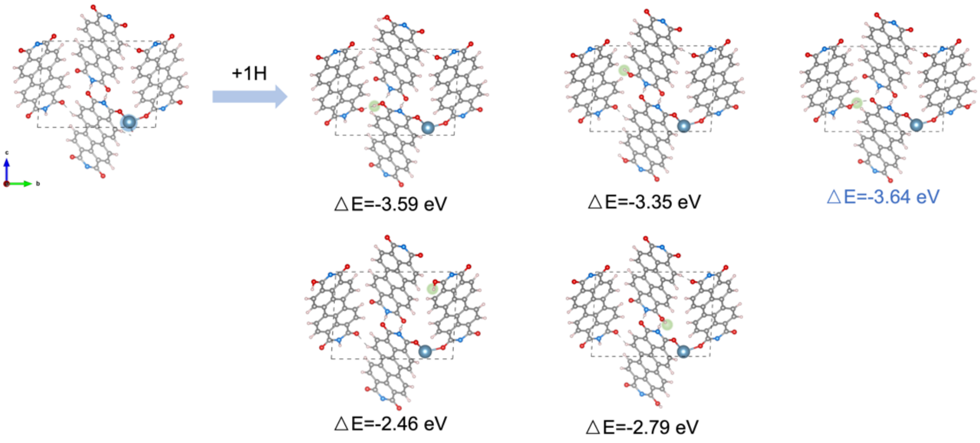

Figure 5.10 Possible geometrical configurations and calculated ΔE for unit cell of different PTCDI-Ca-H intercalation structures.

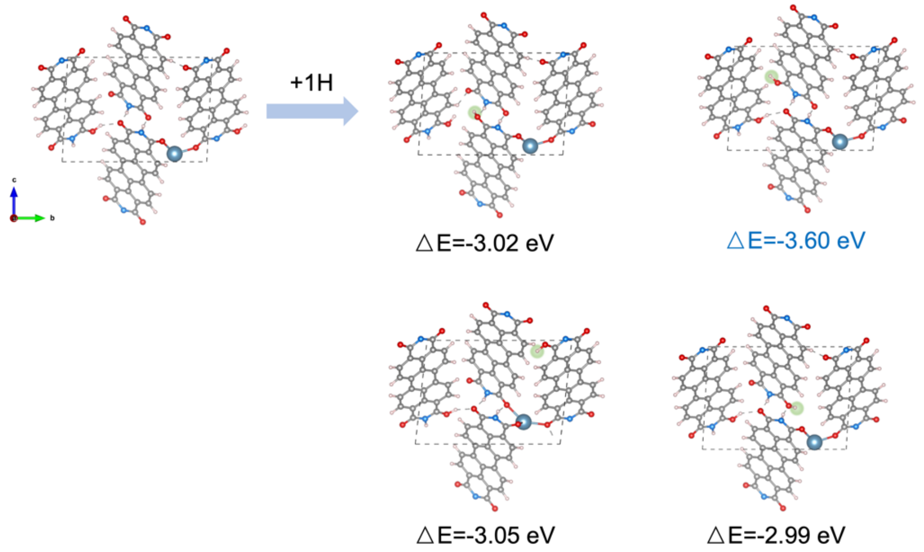

Figure 5.11 Possible geometrical configurations and calculated □E for unit cell of different PTCDI-Ca-2H intercalation structures.

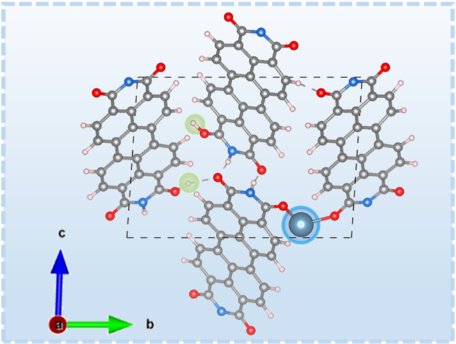

Figure 5.12 Preferable H^+/Ca^{2+}-PTCDI insertion configuration. The C, N, H, O and Ca atoms are represented in grey, blue, pink, red and cyan blue, respectively.

The charge density difference distributions of inserted ions (single Ca^{2+} and H^+/Ca^{2+}) at the most favorable insertion site are discussed to further understand the insertion mechanism. As shown in Figure 5.13a, the O-H and O-Ca bonds exhibit obviously charge transfer to the neighbor O-C bonds in PTCDI, indicating the strong interaction of H^+ and Ca^{2+} with the PTCDI. The investigation of Ca^{2+} diffusion is a crucial task as it is closely linked to the rate capability of batteries. CI-NEB method is employed to investigate the pathway of Ca^{2+} from one energetically most favorable insertion site to a neighboring stable site within the PTCDI crystal. As illustrated in Figure 5.13b, the energy barriers associated with Mg^{2+} diffusion is approximately 0.81 eV, whereas the co-insertion of H^+ can lower the energy barrier to 0.62 eV, thereby facilitating the diffusion of Ca^{2+} in the system. Figure 5.13c depicts the working mechanism of H^+ co-insertion to improve the electrochemical performance of PTCDI anode. In non-aqueous electrolyte, pure Ca^{2+} storage shows characteristics of low capacity, poor rate capability and long activation process due to sluggish diffusion kinetics. By contrast, the presence of H^+ co-insertion in the aqueous system brings about two benefits: i) rapid diffusion kinetics for superior rate capability; ii) a 41% capacity improvement. It is a delight to find that the H^+ insertion could contribute additional capacity while does not deteriorate the Ca^{2+} storage.

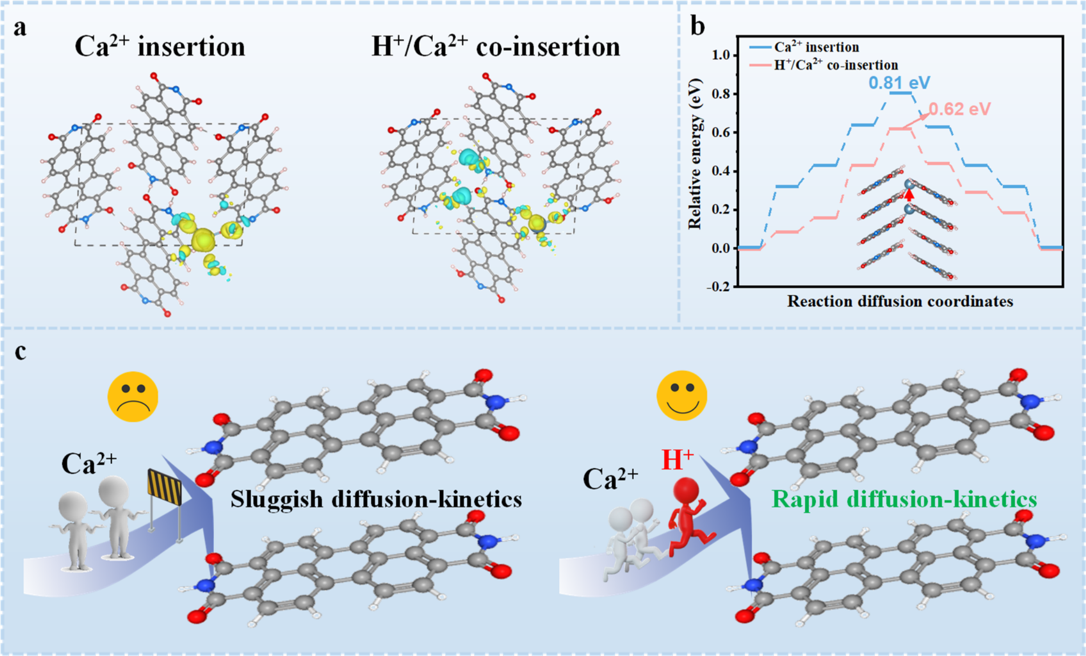

Figure 5.13 a) The charge density difference distributions after Ca^{2+} and H^+/Ca^{2+} insertion into the PTCDI, respectively. b) The diffusion energy barriers of Ca^{2+} in PTCDI and H^+ co-inserted PTCDI. Inset shows the diffusion pathway of Ca^{2+} confined within the channel of PTCDI. c) Schematic diagram of single Ca^{2+} and synergistic Ca^{2+} and H^+ diffusion in PTCDI anode.

5.2.3 Construction of an aqueous full cell

To demonstrate the practical application of PTCDI in aqueous system, a full battery is fabricated by coupling with a calciated copper hexacyanoferrate (Ca_xCuHCF) cathode. We first evaluate the performance of CuHCF in aqueous CIBs. The capacity decreases rapidly because of the dissolution of metal ions in 1 M, which can be suppressed by increasing the electrolyte concentration.[100] Thus the full cell is fabricated in 3 M aqueous electrolyte. The assembled battery delivers a specific capacity of 83 mAh g^{-1} with an output voltage of ~1.1 V (Figure 5.14a, b). Specific capacities of 80, 76, 72, 70, 63, 58 and 55 mAh g^{-1} are achieved at 0.5, 1, 2, 3, 5, 8 and 10 A g^{-1}, respectively, exhibiting a remarkable rate capability (Figure 5.14b). The full cell can stably run for 3000 cycles at 1 A g^{-1}, verifying long-term cyclic stability (Figure 5.14c).

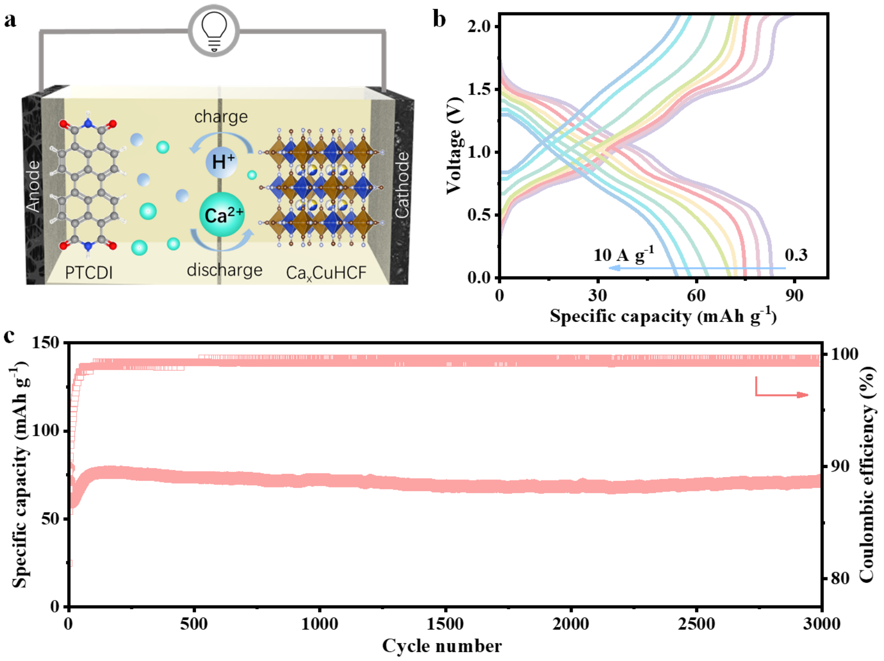

Figure 5.14 Aqueous Ca-ion full cell based on PTCDI anode. a) Schematic diagram of the PTCDI|Ca_xCuHCF full cell. b) Voltage profiles at a series of current densities. c) Cyclic performance under 1 A g^{-1}.

5.2.4 Exploration in Mg-ion system

We further extend the exploration to MIBs to investigate whether the H^+ co-insertion presents and the effect on Mg^{2+} storage. The voltage of AC electrode in Mg-based systems are calibrated to be ~2.6 and ~2.9 V vs. Mg/Mg^{2+} (Figure 5.15, 16). As shown in Figure 5.17a, it exhibits a similar phenomenon to that in CIBs: PTCDI delivers a much higher specific capacity in aqueous electrolyte than that in organic one, with different voltage plateaus. It also provides a superior rate capability and higher ionic diffusion coefficient in aqueous system than that in organic one (Figure 5.17b, c, d). In addition, PTCDI undergoes a 22% capacity decline in organic electrolyte, while aqueous electrolyte enables a 97% capacity retention after 1000 cycles (Figure 5.17e).

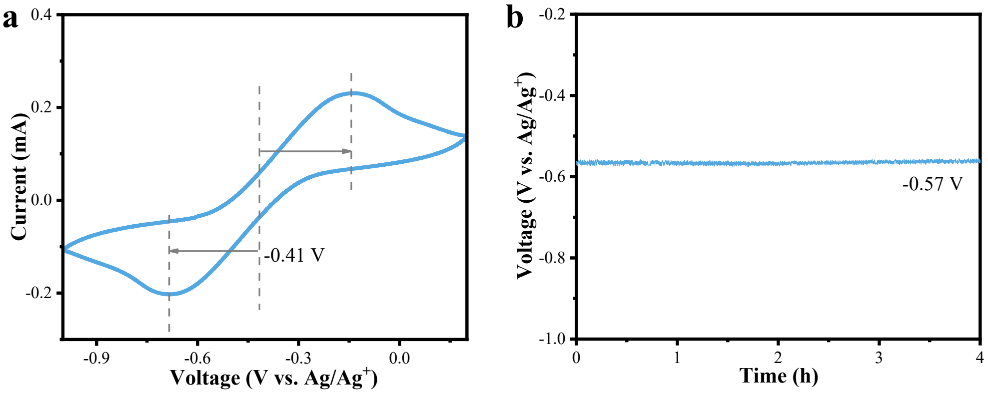

Figure 5.15 a) CV curve of 5 mM ferrocene in 1 M $Mg(TFSI)_2$-EC/PC electrolyte on a Pt working electrode, the reference electrode is Ag/Ag^+ containing 0.01 M $AgNO_3$ in 1 M $Mg(TFSI)_2$-EC/PC. b) OCV of AC vs. Ag/Ag^+ reference electrode. The OCV of AC is -0.57 V. The AC voltage can be estimated to be 2.6 V vs. Mg/Mg^{2+}.

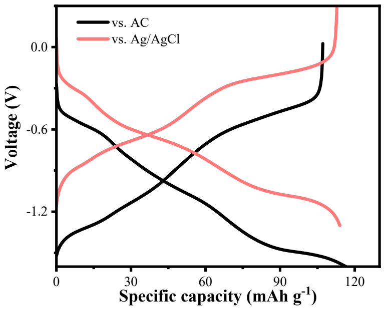

Figure 5.16 Voltage profiles of PTCDI anode where AC and Ag/AgCl act as reference electrodes. The voltage of AC vs. Ag/AgCl can be estimated to be ~0.3 V, thus the AC voltage vs. Mg/Mg^{2+} is determined to be ~2.9 V.

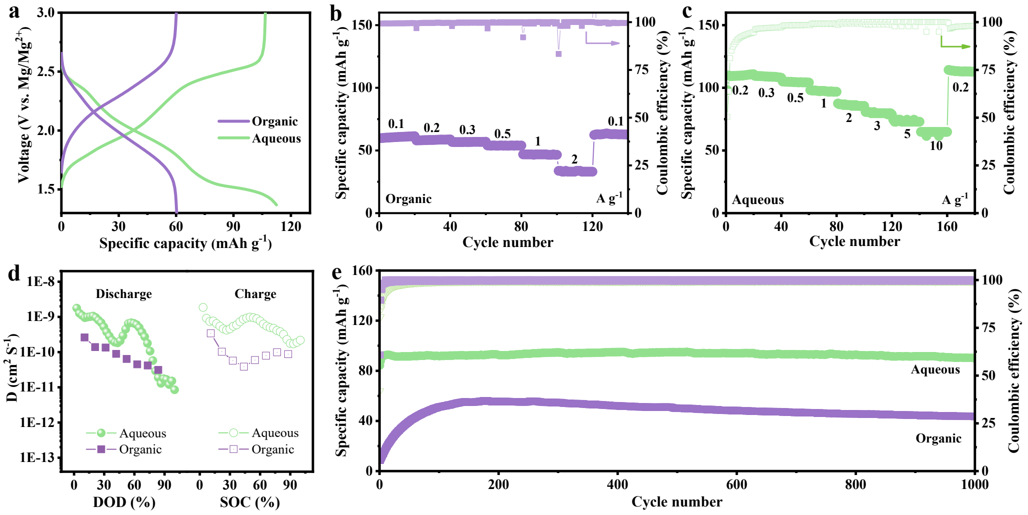

Figure 5.17 Electrochemical performance of PTCDI in MIBs. a) Voltage profiles in 1 M $Mg(TFSI)_2$-H_2O and 1 M $Mg(TFSI)_2$-EC/PC electrolytes. b) Rate performance in organic electrolyte. The cell is pre-cycled at 0.1 A g^{-1} for 100 cycles to activate the electrode. c) Rate performance in aqueous electrolyte without activation. d) Charger diffusivity and e) cyclic performance in organic and aqueous electrolytes at 1 A g^{-1}.

The CV curves in HTFSI-H_2O are collected to identify the protons storage in aqueous electrolyte. For a clear comparison, we down-shift the curve in HTFSI-H_2O solution to calibrate the potential caused by the pH difference between it and $Mg(TFSI)_2$-H_2O electrolyte. The location of the reduction peaks overlapped with that in 1 M $Mg(TFSI)_2$-H_2O, endorsing the H^+ storage (Figure 5.18a). As shown in Figure 5.18b, after discharging to -0.45 V (B point in Figure 5.18d), an additional weak peak at 4.2 ppm appears, indicating the insertion of H^+ into PTCDI at the early stage of the discharge process. The amount of H^+ increases after full discharge, as confirmed by the enhanced intensity of this peak. The capacity contribution from Mg^{2+} is determined to be 60% according to the Mg^{2+} content in the fully discharged sample measured by the

ICP-OES (Figure 5.18c and Table 5.2). Therefore, a 40% capacity (i.e., 43 mAh g^{-1}) is gained from H^+ insertion, which agrees well with the capacity difference between organic and aqueous electrolytes. Ex-situ FTIR reveals the reversible conversion between C=O and $C\text{-}O^-$ is responsible for the cation storage (Figure 5.18e).

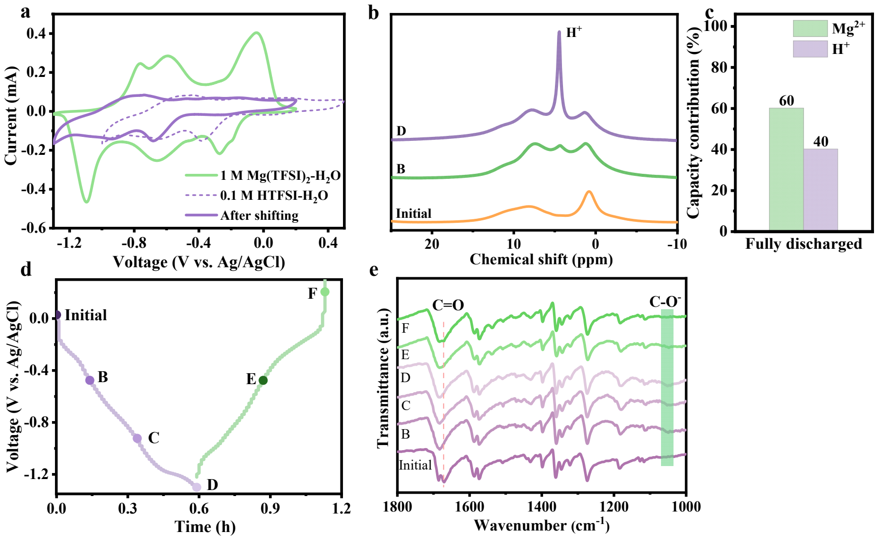

Figure 5.18 a) CV curves of PTCDI anode in 1 M $Mg(TFSI)_2\text{-}H_2O$ and 0.1 M HTFSI-H_2O at 1 mV s^{-1}. b) ^1H solid-state NMR spectra of pristine and discharged PTCDI. c) Calculated Mg^{2+} and H^+ contribution. d) GCD curves under 0.2 A g^{-1}. e) Ex-situ FTIR spectra at selected potentials.

Table 5.2 The Mg content in PTCDI anode at different electrochemical states and calculated Mg^{2+}/H^+ contribution using ICP-OES.

Electrolyte	Organic 1 M $Mg(TFSI)_2$-EC/PC	Aqueous 1 M $Mg(TFSI)_2\text{-}H_2O$
Sample	Fully discharge	Fully discharge
Mg content (%)	1.38	1.50
Discharge capacity (mAh g^{-1})	60	109

Mg^{2+} capacity contribution (mAh g^{-1})	60	65
Mg^{2+} capacity contribution (%)	100%	60%
H^+ capacity contribution (%)	0%	40%

The H^+/Mg^{2+} insertion pathway and kinetics are further explored by DFT simulations. As shown in Figure 5.19-21, PTCDI anode undergoes a similar reaction pathway in aqueous MIBs with that in CIBs. The diffusion energy barrier of Mg^{2+} in PTCDI is about 0.78 eV, which decreases to 0.61 eV when the H^+ co-insertion occurs (Figure 5.22). Therefore, the H^+/Mg^{2+} co-insertion leads to a fast ion diffusion kinetics. Finally, a PTCDI|Mg_xCuHCF full cell is also assembled to demonstrate the application potential. The cell delivers an average voltage of ~1.1 V, fast charge/discharge capability (75% capacity retention at 10 A g^{-1} vs. that at 0.3 A g^{-1}) and long cyclic life (2000 cycles) (Figure 5.23).

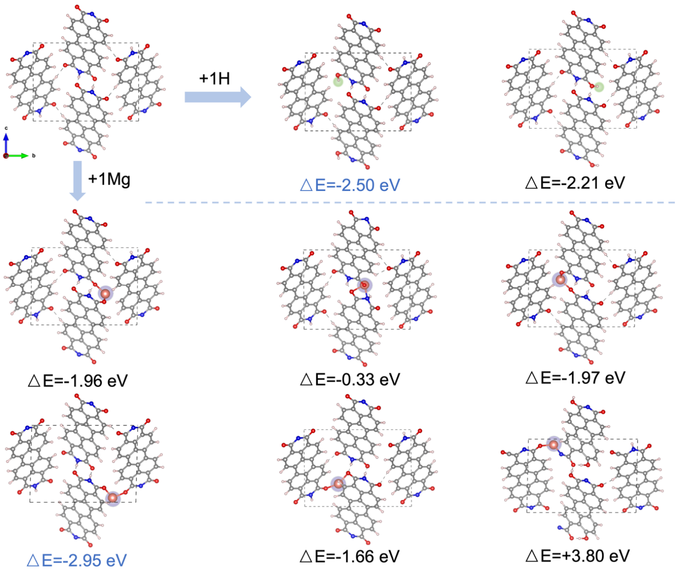

Figure 5.19 Possible geometrical configurations and calculated □E for unit cell of different PTCDI-H and PTCDI-Mg insertion structures.

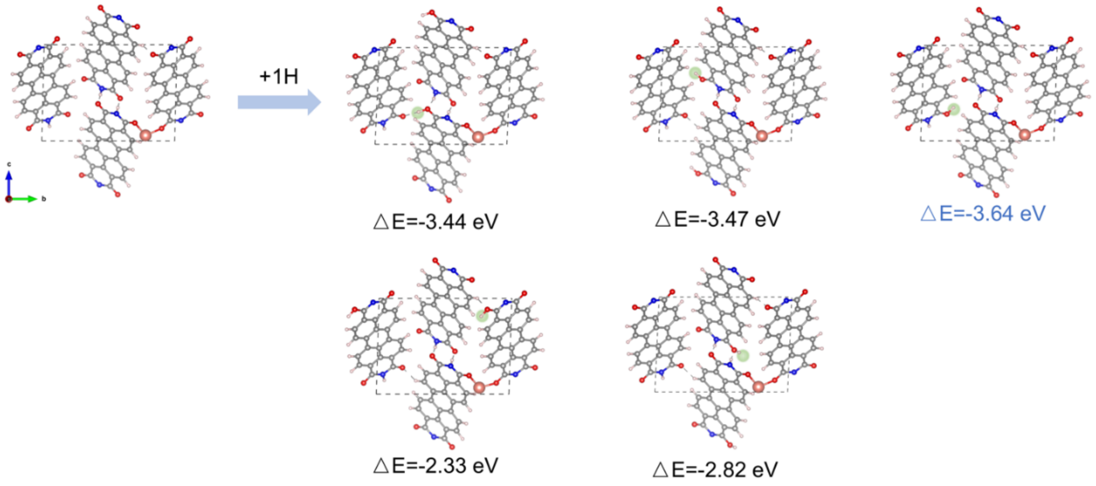

Figure 5.20 Possible geometrical configurations and calculated □E for unit cell of different PTCDI-Mg-H insertion structures.

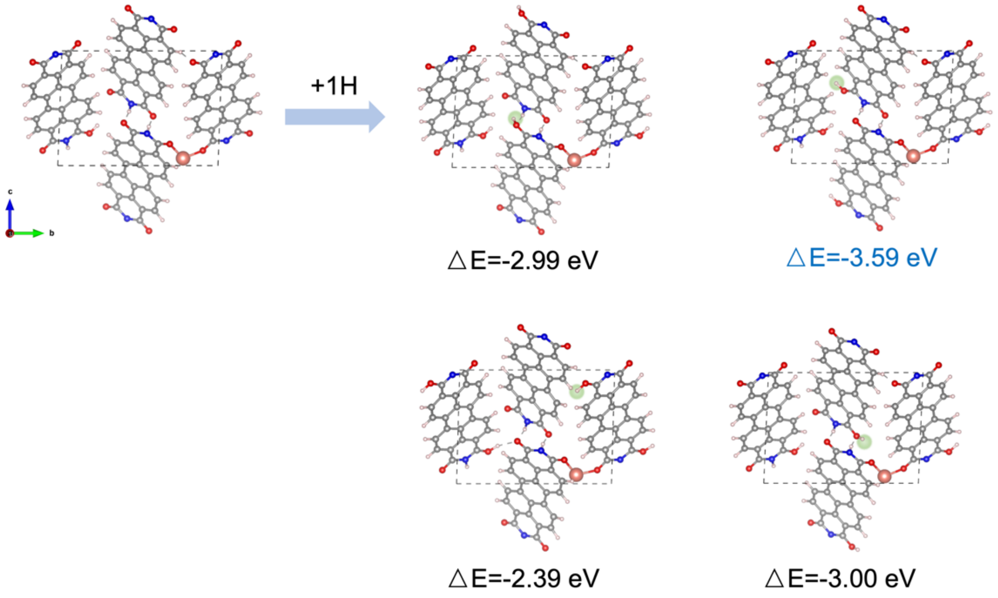

Figure 5.21 Possible geometrical configurations and calculated □E for unit cell of different PTCDI-Mg-2H insertion structures.

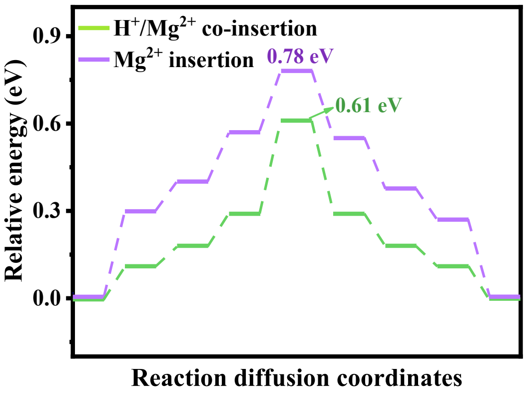

Figure 5.22 The diffusion energy barriers of Mg^{2+} in PTCDI and H^+ co-inserted PTCDI.

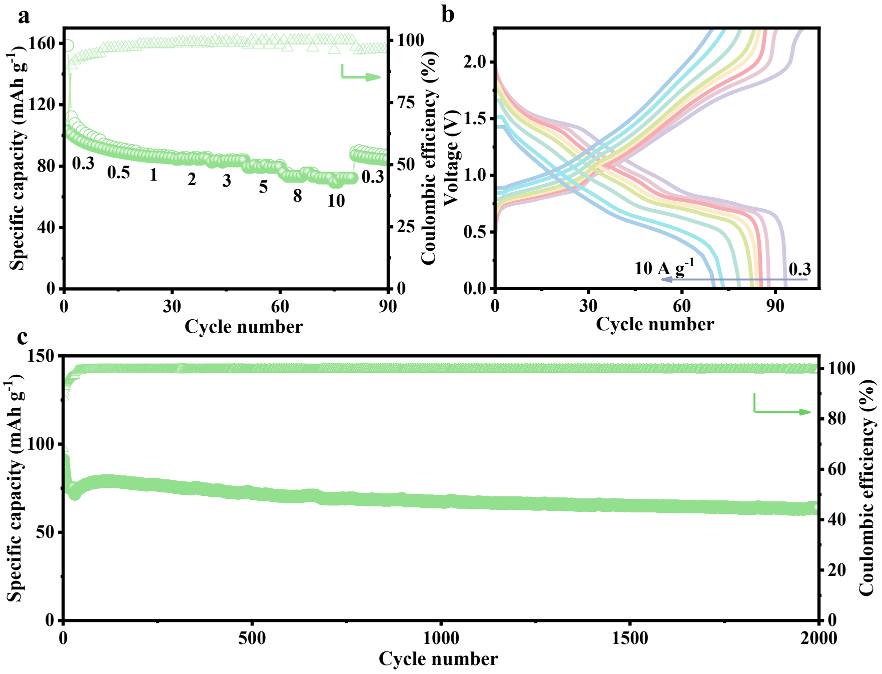

Figure 5.23 a) Rate performance and b) voltage profiles at a series of current densities of the Mg-ion full cell. c) Cyclic performance under 1 A g^{-1} after 0.3 A g^{-1} for 30 cycles.

5.3 Summary

In summary, we report a synergistic H^+ and Ca^{2+} storage enabling the advanced organic anode in aqueous CIBs. The co-insertion mechanism leads to a higher specific capacity of 113 mAh g^{-1} in aqueous electrolyte than in the organic counterpart, where Ca^{2+} acts as the only charge carrier. Furthermore, the proton insertion also benefits the diffusion kinetics to enable fast charging/discharging competence, as proved by electrochemical analysis and DFT calculations. By coupling with a PBA cathode, a high-safety aqueous full cell is demonstrated, which shows remarkable rate performance (66% capacity retention at 10 A g^{-1} vs. that at 0.3 A g^{-1}) and long-term cyclic stability (3000 cycles). Furthermore, this phenomenon can be extended to the Mg-based system, providing a high-rate and ultra-stable organic anode for aqueous MIBs. This work offers an alternative way to develop high-performance aqueous CIBs and MIBs taking advantage of H^+ co-insertion behavior.

Chapter 6. Conclusion and future work

This chapter offers a summary of the main results of this thesis and proposes an outlook for future work.

6.1 Conclusion

In this thesis, advanced electrode materials are investigated to understand the Ca-ion storage mechanism and correlate with electrolyte chemistry. Specifically, the charge storage pathways of Se, PTPAn and PTCDI electrode are explored by combined spectroscopic analysis and theoretical calculations. More importantly, the effects of electrolytes on the electrodes' electrochemical behavior are probed. The major findings reached from this thesis are highlighted as follows:

(1) A new conversion-type material, Se is proposed as a high-capacity electrode for non-aqueous and aqueous CIBs, which delivers a specific capacity of 476 mAh g^{-1} with an average voltage of 2.2 V vs. Ca/Ca^{2+}, offering a higher energy density than other reported cathode materials. A multi-step conversion process of $Se \rightarrow CaSe_4 \rightarrow Ca_2Se_5 \rightarrow CaSe$ is revealed. Surprisingly, such an electrode also shows good compatibility with aqueous electrolytes after expanding the electrochemical window by utilizing a 6.25 M $Ca(TFSI)_2/H_2O$ electrolyte. A high-safety aqueous CIB is demonstrated by coupling with a Cu-based PBA cathode.

(2) We probe the anion's effect on the electrochemical behavior of PTPAn to build reliable Ca-based dual ion batteries in both organic and aqueous electrolytes. The optimal electrolyte chemistry enables a high average potential of 3.8 V vs. Ca/Ca^{2+} with record-breaking rate capability (88 mAh g^{-1} and 55 mAh g^{-1}, respectively, at 1 C and

100 C rate), superior cyclic stability (82% capacity retention after 2000 cycles) and wide-temperature range operation (from -25 to 50 °C). A 2.45 V-class Ca full cell is fabricated by coupling such a cathode/electrolyte system with a graphite anode, delivering fast kinetics up to 50 C rate and long-term cyclic stability of 2000 cycles. Furthermore, PTPAn is highly compatible with $Ca(TFSI)_2/H_2O$ electrolytes.

(3) Employing the PTCDI anode as the model system, we systematically explore the charge storage behavior in non-aqueous and aqueous electrolytes. A synergistic Ca^{2+} and H^+ co-insertion to boost the reaction kinetics in aqueous electrolyte is proposed. The co-storage mechanism leads to an enhanced specific capacity from 68 to 113 mAh g^{-1} at 0.2 A g^{-1} and boosted rate capability from 74% to 92% capacity retention at 2 A g^{-1}. Furthermore, this phenomenon can be extended to MIBs, enabling high-power and ultra-stable organic anode for aqueous MIBs. Stable aqueous Mg-/Ca-ion full cells are demonstrated by coupling with a CuHCF cathode.

6.2 Future work

In this thesis, we develop advanced electrodes for non-aqueous and aqueous CIBs, revealing their reaction pathways and the effects of electrolyte chemistry. However, there still exists great challenges for the further development of CIBs. Two potential directions in future research are presented in the following:

(1) We achieve reversible Se electrode in non-aqueous and aqueous CIBs, however, it still exhibits an unsatisfactory cyclic stbility and rate capability. The reaction pathway and performance of Se are significantly influenced by electrolyte. Further efforts should

be made to explore the detailed impact of electrolyte composition on the performance of Se to construct a stable Ca-Se battery.

(2) We develop advanced organic PTPAn and PTCDI electrodes for non-aqueous and aqueous CIBs, which deliver excellent cycle stability and rate performance. However, organic materials still face challenge of low capacity. In the future study, organic electrodes with higher specific capacity should be developed.

References

1. Feng, X.; Ouyang, M.; Liu, X.; Lu, L.; Xia, Y.; He, X. Thermal runaway mechanism of lithium ion battery for electric vehicles: A review. *Energy Storage Mater.* **2018**, *10*, 246-267.
2. Lu, L.; Han, X.; Li, J.; Hua, J.; Ouyang, M. A review on the key issues for lithium-ion battery management in electric vehicles. *J. Power Sources* **2013**, *226*, 272-288.
3. Lisbona, D.; Snee, T. A review of hazards associated with primary lithium and lithium-ion batteries. *Process Saf. Environ. Prot.* **2011**, *89*, 434-442.
4. Grimaud, A. Batteries: Beyond intercalation and conversion. *Nat. Energy* **2017**, *2*, 17003.
5. Liu, Q.; Wang, H.; Jiang, C.; Tang, Y. Multi-ion strategies towards emerging rechargeable batteries with high performance. *Energy Storage Mater.* **2019**, *23*, 566-586.
6. Zhang, X. Y.; Lv, R. J.; Tang, W. J.; Li, G. J.; Wang, A. X.; Dong, A. P.; Liu, X. J.; Luo, J. Y. Challenges and opportunities for multivalent metal anodes in rechargeable batteries. *Adv. Funct. Mater.* **2020**, *30*, 2004187.
7. Liang, Y.; Dong, H.; Aurbach, D.; Yao, Y. Current status and future directions of multivalent metal-ion batteries. *Nat. Energy* **2020**, *5*, 646-656.
8. Xie, J.; Zhang, Q. Recent progress in multivalent metal (Mg, Zn, Ca, and Al) and metal-ion rechargeable batteries with organic materials as promising electrodes. *Small* **2019**, *15*, 1805061.

9. Arroyo-de Dompablo, M. E.; Ponrouch, A.; Johansson, P.; Palacin, M. R. Achievements, challenges, and prospects of calcium batteries. *Chem. Rev.* **2020**, *120*, 6331-6357.

10. Chen, C.; Shi, F.; Xu, Z.-L. Advanced electrode materials for nonaqueous calcium rechargeable batteries. *J. Mater. Chem. A* **2021**, *9*, 11908-11930.

11. Ta, K.; Zhang, R.; Shin, M.; Rooney, R. T.; Neumann, E. K.; Gewirth, A. A. Understanding ca electrodeposition and speciation processes in nonaqueous electrolytes for next-generation Ca-ion batteries. *ACS Appl. Mater. Interfaces* **2019**, *11*, 21536-21542.

12. Ji, B.; He, H.; Yao, W.; Tang, Y. Recent advances and perspectives on calcium-ion storage: Key materials and devices. *Adv. Mater.* **2021**, *33*, 2005501.

13. Stievano, L.; de Meatza, I.; Bitenc, J.; Cavallo, C.; Brutti, S.; Navarra, M. A. Emerging calcium batteries. *J. Power Sources* **2021**, *482*, 228875.

14. Hosein, I. D. The promise of calcium batteries: Open perspectives and fair comparisons. *ACS Energy Lett.* **2021**, *6*, 1560-1565.

15. Wang, D.; Gao, X.; Chen, Y.; Jin, L.; Kuss, C.; Bruce, P. G. Plating and stripping calcium in an organic electrolyte. *Nat. Mater.* **2018**, *17*, 16-20.

16. Jie, Y.; Tan, Y.; Li, L.; Han, Y.; Xu, S.; Zhao, Z.; Cao, R.; Ren, X.; Huang, F.; Lei, Z.; et al. Electrolyte solvation manipulation enables unprecedented room-temperature calcium-metal batteries. *Angew. Chem. Int. Ed.* **2020**, *59*, 12689-12693.

17. Li, Z.; Fuhr, O.; Fichtner, M.; Zhao-Karger, Z. Towards stable and efficient electrolytes for room-temperature rechargeable calcium batteries. *Energy Environ. Sci.* **2019**, *12*, 3496-3501.

18. Hahn, N. T.; Self, J.; Seguin, T. J.; Driscoll, D. M.; Rodriguez, M. A.; Balasubramanian, M.; Persson, K. A.; Zavadil, K. R. The critical role of configurational flexibility in facilitating reversible reactive metal deposition from borohydride solutions. *J. Mater. Chem. A* **2020**, *8*, 7235-7244.

19. Ponrouch, A.; Frontera, C.; Barde, F.; Palacin, M. R. Towards a calcium-based rechargeable battery. *Nat. Mater.* **2016**, *15*, 169-172.

20. Li, Z. Y.; Fuhr, O.; Fichtner, M.; Zhao-Karger, Z. Towards stable and efficient electrolytes for room-temperature rechargeable calcium batteries. *Energy Environ. Sci.* **2019**, *12*, 3496-3501.

21. Shyamsunder, A.; Blanc, L. E.; Assoud, A.; Nazar, L. F. Reversible calcium plating and stripping at room temperature using a borate salt. *ACS Energy Lett.* **2019**, *4*, 2271-2276.

22. Nielson, K. V.; Luo, J.; Liu, T. L. Optimizing calcium electrolytes by solvent manipulation for calcium batteries. *Batteries Supercaps* **2020**, *3*, 766-772.

23. Song, H.; Wang, C. Current status and challenges of calcium metal batteries. *Adv. Energy Sustain. Res.* **2022**, *3*, 2100192.

24. Kisu, K.; Kim, S.; Shinohara, T.; Zhao, K.; Zuttel, A.; Orimo, S. I. Monocarborane cluster as a stable fluorine-free calcium battery electrolyte. *Sci. Rep.* **2021**, *11*, 7563.

25. Hou, Z.; Zhou, R.; Yao, Y.; Min, Z.; Lu, Z.; Zhu, Y.; Tarascon, J. M.; Zhang, B. Correlation between electrolyte chemistry and solid electrolyte interphase for reversible ca metal anodes. *Angew. Chem. Int. Ed.* **2022**, *61*, 202214796.

26. Hou, Z.; Zhou, R.; Min, Z.; Lu, Z.; Zhang, B. Realizing wide-temperature reversible Ca metal anodes through a Ca^{2+}-conducting artificial layer. *ACS Energy Lett.* **2022**, *8*, 274-279.

27. Mu, P.; Dong, T.; Jiang, H.; Jiang, M.; Chen, Z.; Xu, H.; Zhang, H.; Cui, G. Crucial challenges and recent optimization progress of metal-sulfur battery electrolytes. *Energy Fuels* **2021**, *35*, 1966-1988.

28. Biria, S.; Pathreeker, S.; Genier, F. S.; Li, H.; Hosein, I. D. Plating and stripping calcium at room temperature in an ionic-liquid electrolyte. *ACS Appl. Energy Mater.* **2020**, *3*, 2310-2314.

29. Ponrouch, A.; Frontera, C.; Bardé, F.; Palacín, M. R. Towards a calcium-based rechargeable battery. *Nat. Mater.* **2016**, *15*, 169-172.

30. Ponrouch, A.; Tchitchekova, D.; Frontera, C.; Bardé, F.; Dompablo, M. E. A.-d.; Palacín, M. R. Assessing Si-based anodes for Ca-ion batteries: Electrochemical decalciation of $CaSi_2$. *Electrochem. Commun.* **2016**, *66*, 75-78.

31. Yao, Z. P.; Hegde, V. I.; Aspuru-Guzik, A.; Wolverton, C. Discovery of calcium-metal alloy anodes for reversible Ca-ion batteries. *Adv. Energy Mater.* **2019**, *9*, 1802994.

32. Wang, M.; Jiang, C.; Zhang, S.; Song, X.; Tang, Y.; Cheng, H. M. Reversible calcium alloying enables a practical room-temperature rechargeable calcium-ion battery with a high discharge voltage. *Nat. Chem.* **2018**, *10*, 667-672.

33. Wu, S.; Zhang, F.; Tang, Y. A novel calcium-ion battery based on dual-carbon configuration with high working voltage and long cycling life. *Adv. Sci.* **2018**, *5*, 1701082.

34. Zhao-Karger, Z.; Xiu, Y.; Li, Z.; Reupert, A.; Smok, T.; Fichtner, M. Calcium-tin alloys as anodes for rechargeable non-aqueous calcium-ion batteries at room temperature. *Nat. Commun.* **2022**, *13*, 3849.

35. Emery, N.; Hérold, C.; Lagrange, P. Structural study and crystal chemistry of the first stage calcium graphite intercalation compound. *J. Solid State Chem.* **2005**, *178*, 2947-2952.

36. Xu, W.; Lerner, M. M. A new and facile route using electride solutions to intercalate alkaline earth ions into graphite. *Chem. Mater.* **2018**, *30*, 6930-6935.

37. Park, J.; Xu, Z. L.; Yoon, G.; Park, S. K.; Wang, J.; Hyun, H.; Park, H.; Lim, J.; Ko, Y. J.; Yun, Y. S.; et al. Stable and high-power calcium-ion batteries enabled by calcium intercalation into graphite. *Adv. Mater.* **2020**, *32*, e1904411.

38. Richard Prabakar, S. J.; Ikhe, A. B.; Park, W. B.; Chung, K. C.; Park, H.; Kim, K. J.; Ahn, D.; Kwak, J. S.; Sohn, K. S.; Pyo, M. Graphite as a long-life Ca^{2+}-intercalation anode and its implementation for rocking-chair type calcium-ion batteries. *Adv. Sci.* **2019**, *6*, 1902129.

39. Prabakar, S. J. R.; Sohn, K. S.; Pyo, M. Ca^{2+}-based dual-carbon batteries in ternary ionic liquid electrolytes. *ACS Appl. Mater. Interfaces* **2020**, *12*, 16481-16489.

40. Farokh Niaei, A. H.; Hussain, T.; Hankel, M.; Searles, D. J. Hydrogenated defective graphene as an anode material for sodium and calcium ion batteries: A density functional theory study. *Carbon* **2018**, *136*, 73-84.

41. Yu, X. W.; Boyer, M. J.; Hwang, G. S.; Manthiram, A. Toward a reversible calcium-sulfur battery with a lithium-ion mediation approach. *Adv. Energy Mater.* **2019**, *9*, 1803794.

42. Li, Z.; Vinayan, B. P.; Diemant, T.; Behm, R. J.; Fichtner, M.; Zhao-Karger, Z. Rechargeable calcium-sulfur batteries enabled by an efficient borate-based electrolyte. *Small* **2020**, *16*, 2001806.

43. Scafuri, A.; Berthelot, R.; Pirnat, K.; Vizintin, A.; Bitenc, J.; Aquilanti, G.; Foix, D.; Dedryvere, R.; Arcon, I.; Dominko, R.; et al. Spectroscopic insights into the electrochemical mechanism of rechargeable calcium/sulfur batteries. *Chem. Mater.* **2020**, *32*, 8266-8275.

44. Ren, W.; Xiong, F.; Fan, Y.; Xiong, Y.; Jian, Z. Hierarchical copper sulfide porous nanocages for rechargeable multivalent-ion batteries. *ACS Appl. Mater. Interfaces* **2020**, *12*, 10471-10478.

45. Chae, M. S.; Kwak, H. H.; Hong, S. T. Calcium molybdenum bronze as a stable high-capacity cathode material for calcium-ion batteries. *ACS Appl. Energy Mater.* **2020**, *3*, 5107-5112.

46. Xu, X.; Duan, M.; Yue, Y.; Li, Q.; Zhang, X.; Wu, L.; Wu, P.; Song, B.; Mai, L. Bilayered $Mg_{0.25}V_2O_5 \cdot H_2O$ as a stable cathode for rechargeable Ca-ion batteries. *ACS Energy Lett.* **2019**, *4*, 1328-1335.

47. Tojo, T.; Tawa, H.; Oshida, N.; Inada, R.; Sakurai, Y. Electrochemical characterization of a layered α-MoO_3 as a new cathode material for calcium ion batteries. *J. Electroanal. Chem.* **2018**, *825*, 51-56.

48. Vo, T. N.; Kim, H.; Hur, J.; Choi, W.; Kim, I. T. Surfactant-assisted ammonium vanadium oxide as a superior cathode for calcium-ion batteries. *J. Mater. Chem. A* **2018**, *6*, 22645-22654.

49. Cabello, M.; Nacimiento, F.; Alcántara, R.; Lavela, P.; Pérez Vicente, C.; Tirado, J. L. Applicability of molybdite as an electrode material in calcium batteries: A structural study of layer-type Ca_xMoO_3. *Chem. Mater.* **2018**, *30*, 5853-5861.

50. Jeon, B.; Kwak, H. H.; Hong, S.-T. Bilayered $Ca_{0.28}V_2O_5 \cdot H_2O$: High-capacity cathode material for rechargeable Ca-ion batteries and its charge storage mechanism. *Chem. Mater.* **2022**, *34*, 1491-1498.

51. Hyoung, J.; Heo, J. W.; Jeon, B.; Hong, S.-T. Silver vanadium bronze, β-$Ag_{0.33}V_2O_5$: Crystal-water-free high-capacity cathode material for rechargeable Ca-ion batteries. *J. Mater. Chem. A* **2021**, *9*, 20776-20782.

52. Bervas, M.; Klein, L.; Amatucci, G. Vanadium oxide–propylene carbonate composite as a host for the intercalation of polyvalent cations. *Solid State Ion.* **2005**, *176*, 2735-2747.

53. Wang, J.; Wang, J.; Jiang, Y.; Xiong, F.; Tan, S.; Qiao, F.; Chen, J.; An, Q.; Mai, L. $CaV_6O_{16}\cdot 2.8H_2O$ with Ca^{2+} pillar and water lubrication as a high-rate and long-life cathode material for Ca-ion batteries. *Adv. Funct. Mater.* **2022**, *32*, 2113030.

54. Purbarani, M. E.; Hyoung, J.; Hong, S.-T. Crystal-water-free potassium vanadium bronze ($K_{0.5}V_2O_5$) as a cathode material for Ca-ion batteries. *ACS Appl. Energy Mater.* **2021**, *4*, 7487-7491.

55. Adil, M.; Sarkar, A.; Sau, S.; Muthuraj, D.; Mitra, S. Non-aqueous rechargeable calcium-ion batteries based on high voltage zirconium-doped ammonium vanadium oxide cathode. *J. Power Sources* **2022**, *541*, 231669.

56. Richard Prabakar, S. J.; Ikhe, A. B.; Park, W. B.; Ahn, D.; Sohn, K. S.; Pyo, M. Ultra-high capacity and cyclability of β-phase $Ca_{0.14}V_2O_5$ as a promising cathode in calcium-ion batteries. *Adv. Funct. Mater.* **2023**, *33*, 2301399.

57. Zuo, C.; Xiong, F.; Wang, J.; An, Y.; Zhang, L.; An, Q. MnO_2 polymorphs as cathode materials for rechargeable Ca-ion batteries. *Adv. Funct. Mater.* **2022**, *32*, 2202975.

58. Padigi, P.; Goncher, G.; Evans, D.; Solanki, R. Potassium barium hexacyanoferrate - a potential cathode material for rechargeable calcium ion batteries. *J. Power Sources* **2015**, *273*, 460-464.

59. Kuperman, N.; Padigi, P.; Goncher, G.; Evans, D.; Thiebes, J.; Solanki, R. High performance prussian blue cathode for nonaqueous Ca-ion intercalation battery. *J. Power Sources* **2017**, *342*, 414-418.

60. Tojo, T.; Sugiura, Y.; Inada, R.; Sakurai, Y. Reversible calcium ion batteries using a dehydrated prussian blue analogue cathode. *Electrochim. Acta* **2016**, *207*, 22-27.

61. Lipson, A. L.; Pan, B. F.; Lapidus, S. H.; Liao, C.; Vaughey, J. T.; Ingram, B. J. Rechargeable Ca-ion batteries: A new energy storage system. *Chem. Mater.* **2015**, *27*, 8442-8447.

62. Jeon, B.; Heo, J. W.; Hyoung, J.; Kwak, H. H.; Lee, D. M.; Hong, S. T. Reversible calcium-ion insertion in nasicon-type $NaV_2(PO_4)_3$. *Chem. Mater.* **2020**, *32*, 8772-8780.

63. Kim, S.; Yin, L.; Lee, M. H.; Parajuli, P.; Blanc, L.; Fister, T. T.; Park, H.; Kwon, B. J.; Ingram, B. J.; Zapol, P.; et al. High-voltage phosphate cathodes for rechargeable Ca-ion batteries. *ACS Energy Lett.* **2020**, *5*, 3203-3211.

64. Wang, J.; Tan, S.; Xiong, F.; Yu, R.; Wu, P.; Cui, L.; An, Q. $VOPO_4 \cdot 2H_2O$ as a new cathode material for rechargeable Ca-ion batteries. *Chem. Commun.* **2020**, *56*, 3805-3808.

65. Lipson, A. L.; Kim, S.; Pan, B.; Liao, C.; Fister, T. T.; Ingram, B. J. Calcium intercalation into layered fluorinated sodium iron phosphate. *J. Power Sources* **2017**, *369*, 133-137.

66. Prabakar, S. J. R.; Park, W.-B.; Seo, J. Y.; Singh, S. P.; Ahn, D.; Sohn, K.-S.; Pyo, M. Ultra-stable $Ti_2O(PO_4)_2(H_2O)$ as a viable new Ca^{2+} storage electrode material for calcium-ion batteries. *Energy Storage Mater.* **2021**, *43*, 85-96.

67. Xu, Z. L.; Park, J.; Wang, J.; Moon, H.; Yoon, G.; Lim, J.; Ko, Y. J.; Cho, S. P.; Lee, S. Y.; Kang, K. A new high-voltage calcium intercalation host for ultra-stable and high-power calcium rechargeable batteries. *Nat. Commun.* **2021**, *12*, 3369.

68. Chen, C. H.; Shi, F. Y.; Zhang, S. S.; Su, Y. Q.; Xu, Z. L. Ultrastable and high energy calcium rechargeable batteries enabled by calcium intercalation in a nasicon cathode. *Small* **2022**, *18*, 2107853.

69. Li, Z.; Vinayan, B. P.; Jankowski, P.; Njel, C.; Roy, A.; Vegge, T.; Maibach, J.; Lastra, J. M. G.; Fichtner, M.; Zhao-Karger, Z. Multi-electron reactions enabled by anion-based redox chemistry for high-energy multivalent rechargeable batteries. *Angew. Chem. Int. Ed.* **2020**, *59*, 11483-11490.

70. Zhang, S.; Zhu, Y.; Wang, D.; Li, C.; Han, Y.; Shi, Z.; Feng, S. Poly(anthraquinonyl sulfide)/CNT composites as high-rate-performance cathodes for nonaqueous rechargeable calcium-ion batteries. *Adv. Sci.* **2022**, *9*, 2200397.

71. Li, J.; Han, C. J.; Ou, X. W.; Tang, Y. B. Concentrated electrolyte for high-performance Ca-ion battery based on organic anode and graphite cathode. *Angew. Chem. Int. Ed.* **2022**, *61*, e202116668.

72. Kang, J. E.; Vo, T. N.; Ahn, S.-k.; Lee, S.-W.; Kim, I. T. Unique two-dimensional prussian blue nanoplates for high-performance sodium-ion battery cathode. *J. Alloys Compd.* **2023**, *939*, 168773.

73. Yi, H.; Qin, R.; Ding, S.; Wang, Y.; Li, S.; Zhao, Q.; Pan, F. Structure and properties of prussian blue analogues in energy storage and conversion applications. *Adv. Funct. Mater.* **2021**, *31*, 2006970.

74. Vo, T. N.; Hur, J.; Kim, I. T. Enabling high performance calcium-ion batteries from prussian blue and metal-organic compound materials. *ACS Sustain. Chem. Eng.* **2020**, *8*, 2596-2601.

75. Peng, J.; Zhang, W.; Liu, Q.; Wang, J.; Chou, S.; Liu, H.; Dou, S. Prussian blue analogues for sodium-ion batteries: Past, present, and future. *Adv. Mater.* **2022**, *34*, 2108384.

76. Lee, C.; Jeong, S.-K. A novel strategy to improve the electrochemical performance of a prussian blue analogue electrode for calcium-ion batteries. *Electrochemistry* **2018**, *86*, 134-137.

77. Shiga, T.; Kondo, H.; Kato, Y.; Inoue, M. Insertion of calcium ion into prussian blue analogue in nonaqueous solutions and its application to a rechargeable battery with dual carriers. *J. Phys. Chem. C* **2015**, *119*, 27946-27953.

78. Lipson, A. L.; Han, S.-D.; Kim, S.; Pan, B.; Sa, N.; Liao, C.; Fister, T. T.; Burrell, A. K.; Vaughey, J. T.; Ingram, B. J. Nickel hexacyanoferrate, a versatile intercalation host for divalent ions from nonaqueous electrolytes. *J. Power Sources* **2016**, *325*, 646-652.

79. Guo, S.-P.; Li, J.-C.; Xu, Q.-T.; Ma, Z.; Xue, H.-G. Recent achievements on polyanion-type compounds for sodium-ion batteries: Syntheses, crystal chemistry and electrochemical performance. *J. Power Sources* **2017**, *361*, 285-299.

80. Lan, Y.; Yao, W.; He, X.; Song, T.; Tang, Y. Mixed polyanionic compounds as positive electrodes for low-cost electrochemical energy storage. *Angew. Chem. Int. Ed.* **2020**, *59*, 9255-9262.

81. Yan, L.; Yang, W.; Yu, H.; Zhang, L.; Shu, J. Recent progress in rechargeable calcium-ion batteries for high-efficiency energy storage. *Energy Storage Mater.* **2023**, *60*, 102822.

82. Wang, J.; Tan, S.; Xiong, F.; Yu, R.; Wu, P.; Cui, L.; An, Q. $VOPO_4.2H_2O$ as a new cathode material for rechargeable Ca-ion batteries. *Chem. Commun.* **2020**, *56*, 3805-3808.

83. Hayashi, M.; Arai, H.; Ohtsuka, H.; Sakurai, Y. Electrochemical insertion/extraction of calcium ions using crystalline vanadium oxide. *Electrochem. Solid State Lett.* **2004**, *7*, A119-A121.

84. Zhang, X.; Xu, X.; Song, B.; Duan, M.; Meng, J.; Wang, X.; Xiao, Z.; Xu, L.; Mai, L. Towards a stable layered vanadium oxide cathode for high-capacity calcium batteries. *Small* **2022**, *18*, 2107174.

85. Black, A. P.; Frontera, C.; Torres, A.; Recio-Poo, M.; Rozier, P.; Forero-Saboya, J. D.; Fauth, F.; Urones-Garrote, E.; Arroyo-de Dompablo, M. E.; Palacín, M. R. Elucidation of the redox activity of $Ca_2MnO_{3.5}$ and CaV_2O_4 in calcium batteries using operando XRD: Charge compensation mechanism and reversibility. *Energy Storage Mater.* **2022**, *47*, 354-364.

86. Juran, T. R.; Young, J.; Smeu, M. Density functional theory modeling of MnO_2 polymorphs as cathodes for multivalent ion batteries. *J. Phys. Chem. C* **2018**, *122*, 8788-8795.

87. Kwon, B. J.; Yin, L.; Bartel, C. J.; Kumar, K.; Parajuli, P.; Gim, J.; Kim, S.; Wu, Y. A.; Klie, R. F.; Lapidus, S. H.; et al. Intercalation of Ca into a highly defective manganese oxide at room temperature. *Chem. Mater.* **2022**, *34*, 836-846.

88. Dompablo, M. E. A.-d.; Krich, C.; Nava-Avendaño, J.; Biškup, N.; Palacín, M. R.; Bardé, F. A joint computational and experimental evaluation of $CaMn_2O_4$

polymorphs as cathode materials for Ca ion batteries. *Chem. Mater.* **2016**, *28*, 6886-6893.

89. Pathreeker, S.; Reed, S.; Chando, P.; Hosein, I. D. A study of calcium ion intercalation in perovskite calcium manganese oxide. *J. Electroanal. Chem.* **2020**, *874*, 114453.

90. Cabello, M.; Nacimiento, F.; González, J. R.; Ortiz, G.; Alcántara, R.; Lavela, P.; Pérez-Vicente, C.; Tirado, J. L. Advancing towards a veritable calcium-ion battery: $CaCo_2O_4$ positive electrode material. *Electrochem. Commun.* **2016**, *67*, 59-64.

91. Park, H.; Zapol, P. Thermodynamic and kinetic properties of layered-$CaCo_2O_4$ for the Ca-ion batteries: A systematic first-principles study. *J. Mater. Chem. A* **2020**, *8*, 21700-21710.

92. See, K. A.; Gerbec, J. A.; Jun, Y.-S.; Wudl, F.; Stucky, G. D.; Seshadri, R. A high capacity calcium primary cell based on the Ca-S system. *Adv. Energy Mater.* **2013**, *3*, 1056-1061.

93. Zhou, D.; Tang, X.; Zhang, X.; Zhang, F.; Wu, J.; Kang, F.; Li, B.; Wang, G. Multi-ion strategy toward highly durable calcium/sodium-sulfur hybrid battery. *Nano Lett.* **2021**, *21*, 3548-3556.

94. Kisu, K.; Mohtadi, R.; Orimo, S. I. Calcium metal batteries with long cycle life using a hydride-based electrolyte and copper sulfide electrode. *Adv. Sci.* **2023**, *10*, 2301178.

95. Meng, Z.; Reupert, A.; Tang, Y.; Li, Z.; Karkera, G.; Wang, L.; Roy, A.; Diemant, T.; Fichtner, M.; Zhao-Karger, Z. Long-cycle-life calcium battery with a high-

capacity conversion cathode enabled by a Ca^{2+}/Li^{+} hybrid electrolyte. *ACS Appl. Mater. Interfaces* **2022**, *14*, 54616-54622.

96. Esser, B.; Dolhem, F.; Becuwe, M.; Poizot, P.; Vlad, A.; Brandell, D. A perspective on organic electrode materials and technologies for next generation batteries. *J. Power Sources* **2021**, *482*, 228814.
97. Chae, M. S.; Nimkar, A.; Shpigel, N.; Gofer, Y.; Aurbach, D. High performance aqueous and nonaqueous Ca-ion cathodes based on fused-ring aromatic carbonyl compounds. *ACS Energy Lett.* **2021**, *6*, 2659-2665.
98. Wu, S.; Zhang, F.; Tang, Y. A novel calcium-ion battery based on dual-carbon configuration with high working voltage and long cycling life. *Adv. Sci.* **2018**, *5*, 1701082.
99. Gheytani, S.; Liang, Y.; Wu, F.; Jing, Y.; Dong, H.; Rao, K. K.; Chi, X.; Fang, F.; Yao, Y. An aqueous Ca-ion battery. *Adv. Sci.* **2017**, *4*, 1700465.
100. Lee, C.; Jeong, S.-K. Modulating the hydration number of calcium ions by varying the electrolyte concentration: Electrochemical performance in a prussian blue electrode/aqueous electrolyte system for calcium-ion batteries. *Electrochim. Acta* **2018**, *265*, 430-436.
101. Du, C.-Y.; Zhang, Z.-H.; Li, X.-L.; Luo, R.-J.; Ma, C.; Bao, J.; Zeng, J.; Xu, X.; Wang, F.; Zhou, Y.-N. Enhancing structural and cycle stability of prussian blue cathode materials for calcium-ion batteries by introducing divalent Fe. *Chem. Eng. J.* **2023**, *451*, 138650.

102. Chae, M. S.; Heo, J. W.; Hyoung, J.; Hong, S. T. Double-sheet vanadium oxide as a cathode material for calcium-ion batteries. *ChemNanoMat* **2020**, *6*, 1049-1053.

103. Hyoung, J.; Heo, J. W.; Hong, S.-T. Investigation of electrochemical calcium-ion energy storage mechanism in potassium birnessite. *J. Power Sources* **2018**, *390*, 127-133.

104. Shi, Z. Y.; Wu, J. H.; Ni, M. Z.; Guo, Q. B.; Zan, F.; Xia, H. Superior performance of calcium birnessite by electrochemical conversion as cathode for aqueous calcium ion battery. *Mater. Res. Bull.* **2021**, *144*, 111475.

105. Dong, L. W.; Xu, R. G.; Wang, P. P.; Sun, S. C.; Li, Y.; Zhen, L.; Xu, C. Y. Layered potassium vanadate $K_2V_6O_{16}$ nanowires: A stable and high capacity cathode material for calcium-ion batteries. *J. Power Sources* **2020**, *479*, 228793.

106. Liu, L.; Wu, Y. C.; Rozier, P.; Taberna, P. L.; Simon, P. Ultrafast synthesis of calcium vanadate for superior aqueous calcium-ion battery. *Research* **2019**, 6585686.

107. Han, C.; Li, H.; Li, Y.; Zhu, J.; Zhi, C. Proton-assisted calcium-ion storage in aromatic organic molecular crystal with coplanar stacked structure. *Nat. Commun.* **2021**, *12*, 2400.

108. Li, L.; Zhang, G.; Deng, X.; Hao, J.; Zhao, X.; Li, H.; Han, C.; Li, B. A covalent organic framework for high-rate aqueous calcium-ion batteries. *J. Mater. Chem. A* **2022**, *10*, 20827-20836.

109. Tang, X.; Zhou, D.; Zhang, B.; Wang, S.; Li, P.; Liu, H.; Guo, X.; Jaumaux, P.; Gao, X.; Fu, Y.; et al. A universal strategy towards high-energy aqueous multivalent-ion batteries. *Nat. Commun.* **2021**, *12*, 2857.

110. Qin, Z. M.; Song, Y.; Liu, Y. Z.; Liu, X. X. Aqueous calcium-ion storage in amorphous molybdenum oxide. *Chem. Eng. J.* **2023**, *451*, 138681.

111. Suo, L.; Borodin, O.; Gao, T.; Olguin, M.; Ho, J.; Fan, X.; Luo, C.; Wang, C.; Xu, K. J. S. "Water-in-salt" electrolyte enables high-voltage aqueous lithium-ion chemistries. *Science* **2015**, *350*, 938-943.

112. Tong, Z. Q.; Kang, T. X.; Wan, Y. P.; Yang, R.; Wu, Y.; Shen, D.; Liu, S. A.; Tang, Y. B.; Lee, C. S. A Ca-ion electrochromic battery via a water-in-salt electrolyte. *Adv. Funct. Mater.* **2021**, *31*, 2104639.

113. Rastgoo-Deylami, M.; Chae, M. S.; Hong, S.-T. $H_2V_3O_8$ as a high energy cathode material for nonaqueous magnesium-ion batteries. *Chem. Mater.* **2018**, *30*, 7464-7472.

114. Blöchl, P. E. Projector augmented-wave method. *Phys. Rev. B* **1994**, *50*, 17953-17979.

115. Perdew, J. P.; Burke, K.; Ernzerhof, M. Generalized gradient approximation made simple. *Phys. Rev. Lett.* **1996**, *77*, 3865-3868.

116. Kresse, G.; Furthmüller, J. Efficiency of ab-initio total energy calculations for metals and semiconductors using a plane-wave basis set. *Comput. Mater. Sci.* **1996**, *6*, 15-50.

117. Kresse, G.; Furthmüller, J. Efficient iterative schemes for ab initio total-energy calculations using a plane-wave basis set. *Phys. Rev. B* **1996**, *54*, 11169.

118. Kresse, G.; Joubert, D. From ultrasoft pseudopotentials to the projector augmented-wave method. *Phys. Rev. B* **1999**, *59*, 1758.

119. Perdew, J. P.; Burke, K.; Ernzerhof, M. Generalized gradient approximation made simple. *Phys.Rev. Lett.* **1996**, *77*, 3865.

120. Grimme, S.; Antony, J.; Ehrlich, S.; Krieg, H. A consistent and accurate ab initio parametrization of density functional dispersion correction (DFT-D) for the 94 elements H-Pu. *J. Chem. Phys.* **2010**, *132*, 154104.

121. Henkelman, G.; Uberuaga, B. P.; Jónsson, H. A climbing image nudged elastic band method for finding saddle points and minimum energy paths. *J. Chem. Phys.* **2000**, *113*, 9901-9904.

122. Nosé, S. A unified formulation of the constant temperature molecular dynamics methods. *J. Chem. Phys.* **1984**, *81*, 511-519.

123. Neese, F. The orca program system. *Wiley Interdiscip. Rev.: Comput. Mol. Sci.* **2012**, *2*, 73-78.

124. Krishnan, R.; Binkley, J. S.; Seeger, R.; Pople, J. A. Self-consistent molecular orbital methods. XX. A basis set for correlated wave functions. *J. Chem. Phys.* **1980**, *72*, 650-654.

125. Hehre, W. J.; Ditchfield, R.; Pople, J. A. Self-consistent molecular orbital methods. XII. Further extensions of gaussian-type basis sets for use in molecular orbital studies of organic molecules. *J. Chem. Phys.* **1972**, *56*, 2257-2261.

126. Rassolov, V. A.; Pople, J. A.; Ratner, M. A.; Windus, T. L. 6-31G* basis set for atoms K through Zn. *J. Chem. Phys.* **1998**, *109*, 1223-1229.

127. Zhao, Y.; Truhlar, D. G. The M06 suite of density functionals for main group thermochemistry, thermochemical kinetics, noncovalent interactions, excited states, and transition elements: Two new functionals and systematic testing of four M06-class functionals and 12 other functionals. *Theor. Chem. Acc.* **2008**, *120*, 215-241.

128. Grimme, S.; Ehrlich, S.; Goerigk, L. Effect of the damping function in dispersion corrected density functional theory. *J. Comput. Chem.* **2011**, *32*, 1456-1465.

129. Weigend, F.; Ahlrichs, R. Balanced basis sets of split valence, triple zeta valence and quadruple zeta valence quality for H to Rn: Design and assessment of accuracy. *Phys. Chem. Chem. Phys.* **2005**, *7*, 3297-3305.

130. Barone, V.; Cossi, M. Quantum calculation of molecular energies and energy gradients in solution by a conductor solvent model. *J. Phys. Chem. A* **1998**, *102*, 1995-2001.

131. Kresse, G.; Furthmüller, J. Efficient iterative schemes for ab initio total-energy calculations using a plane-wave basis set. *Phys. Rev. B* **1996**, *54*, 11169-11186.

132. Kresse, G.; Joubert, D. From ultrasoft pseudopotentials to the projector augmented-wave method. *Phys. Rev. B* **1999**, *59*, 1758-1775.

133. Lee, C.; Jeong, Y.-T.; Nogales, P. M.; Song, H.-Y.; Kim, Y.; Yin, R.-Z.; Jeong, S.-K. Electrochemical intercalation of Ca^{2+} ions into TiS_2 in organic electrolytes at room temperature. *Electrochem. Commun.* **2019**, *98*, 115-118.

134. Wu, N.; Yao, W.; Song, X.; Zhang, G.; Chen, B.; Yang, J.; Tang, Y. Hybrid energy storage: A calcium-ion hybrid energy storage device with high capacity and long cycling life under room temperature. *Adv. Energy Mater.* **2019**, *9*, 1970052.

135. Chae, M. S.; Heo, J. W.; Hyoung, J.; Hong, S.-T. Double-sheet vanadium oxide as a cathode material for calcium-ion batteries. *ChemNanoMat* **2020**, *6*, 1049-1053.

136. Adil, M.; Sarkar, A.; Roy, A.; Panda, M. R.; Nagendra, A.; Mitra, S. Practical aqueous calcium-ion battery full-cells for future stationary storage. *ACS Appl. Mater. Interfaces* **2020**, *12*, 11489-11503.

137. Cang, R.; Zhao, C.; Ye, K.; Yin, J.; Zhu, K.; Yan, J.; Wang, G.; Cao, D. Aqueous calcium-ion battery based on a mesoporous organic anode and a manganite cathode with long cycling performance. *ChemSusChem* **2020**, *13*, 3911-3918.

138. Ye, X.; Ruan, J.; Pang, Y.; Yang, J.; Liu, Y.; Huang, Y.; Zheng, S. Enabling a stable room-temperature sodium-sulfur battery cathode by building heterostructures in multichannel carbon fibers. *ACS Nano* **2021**, *15*, 5639-5648.

139. Rojaee, R.; Shahbazian-Yassar, R. Two-dimensional materials to address the lithium battery challenges. *ACS Nano* **2020**, *14*, 2628-2658.

140. Ji, Y.; Liu-Théato, X.; Xiu, Y.; Indris, S.; Njel, C.; Maibach, J.; Ehrenberg, H.; Fichtner, M.; Zhao-Karger, Z. Magnesium-sulfur batteries: Polyoxometalate modified separator for performance enhancement of magnesium-sulfur batteries. *Adv. Funct. Mater.* **2021**, *31*, 2170189.

141. Qin, X.; Wu, J.; Xu, Z.-L.; Chong, W. G.; Huang, J.-Q.; Liang, G.; Li, B.; Kang, F.; Kim, J.-K. Electrosprayed multiscale porous carbon microspheres as sulfur hosts for long-life lithium-sulfur batteries. *Carbon* **2019**, *141*, 16-24.

142. Yang, C. P.; Xin, S.; Yin, Y. X.; Ye, H.; Zhang, J.; Guo, Y. G. An advanced selenium-carbon cathode for rechargeable lithium-selenium batteries. *Angew. Chem. Int. Ed.* **2013**, *52*, 8363-8367.

143. Liu, Q.; Deng, W.; Pan, Y.; Sun, C. F. Approaching the voltage and energy density limits of potassium-selenium battery chemistry in a concentrated ether-based electrolyte. *Chem. Sci.* **2020**, *11*, 6045-6052.

144. Ma, D.; Li, Y.; Yang, J.; Mi, H.; Luo, S.; Deng, L.; Yan, C.; Zhang, P.; Lin, Z.; Ren, X.; et al. Atomic layer deposition-enabled ultrastable freestanding carbon-selenium cathodes with high mass loading for sodium-selenium battery. *Nano Energy* **2018**, *43*, 317-325.

145. Yao, Y.; Chen, M.; Xu, R.; Zeng, S.; Yang, H.; Ye, S.; Liu, F.; Wu, X.; Yu, Y. Cnt interwoven nitrogen and oxygen dual-doped porous carbon nanosheets as free-standing electrodes for high-performance Na-Se and K-Se flexible batteries. *Adv. Mater.* **2018**, *30*, 1805234.

146. Zhang, T.; Cai, T.; Xing, W.; Li, T.; Liang, B.; Hu, H.; Zhao, L.; Li, X.; Yan, Z. A rechargeable 6-electron Al-Se battery with high energy density. *Energy Storage Mater.* **2021**, *41*, 667-676.

147. Yang, X.; Wang, J.; Wang, S.; Wang, H.; Tomanec, O.; Zhi, C.; Zboril, R.; Yu, D. Y. W.; Rogach, A. Vapor-infiltration approach toward selenium/reduced graphene

oxide composites enabling stable and high-capacity sodium storage. *ACS Nano* **2018**, *12*, 7397-7405.

148. Li, Q.; Liu, H.; Yao, Z.; Cheng, J.; Li, T.; Li, Y.; Wolverton, C.; Wu, J.; Dravid, V. P. Electrochemistry of selenium with sodium and lithium: Kinetics and reaction mechanism. *ACS Nano* **2016**, *10*, 8788-8795.
149. Sun, J.; Du, Z.; Liu, Y.; Ai, W.; Wang, K.; Wang, T.; Du, H.; Liu, L.; Huang, W. State-of-the-art and future challenges in high energy lithium-selenium batteries. *Adv. Mater.* **2021**, *33*, 2003845.
150. Abouimrane, A.; Dambournet, D.; Chapman, K. W.; Chupas, P. J.; Weng, W.; Amine, K. A new class of lithium and sodium rechargeable batteries based on selenium and selenium-sulfur as a positive electrode. *J. Am. Chem. Soc.* **2012**, *134*, 4505-4508.
151. Xu, R.; Yao, Y.; Wang, H.; Yuan, Y.; Wang, J.; Yang, H.; Jiang, Y.; Shi, P.; Wu, X.; Peng, Z.; et al. Unraveling the nature of excellent potassium storage in small-molecule Se@peapod-like n-doped carbon nanofibers. *Adv. Mater.* **2020**, *32*, 2003879.
152. Wang, H.; Jiang, Y.; Manthiram, A. Long cycle life, low self-discharge sodium-selenium batteries with high selenium loading and suppressed polyselenide shuttling. *Adv. Energy Mater.* **2017**, *8*, 1701953.
153. Yang, X.; Wang, H.; Yu, D. Y. W.; Rogach, A. L. Vacuum calcination induced conversion of selenium/carbon wires to tubes for high-performance sodium-selenium batteries. *Adv. Funct. Mater.* **2018**, *28*, 1706609.

154. Zhao, X.; Yin, L.; Zhang, T.; Zhang, M.; Fang, Z.; Wang, C.; Wei, Y.; Chen, G.; Zhang, D.; Sun, Z.; et al. Heteroatoms dual-doped hierarchical porous carbon-selenium composite for durable Li-Se and Na-Se batteries. *Nano Energy* **2018**, *49*, 137-146.

155. Hu, X.; Li, J.; Zhong, G.; Liu, Y.; Yuan, J.; Lei, S.; Zhan, H.; Wen, Z. Hierarchical multicavity nitrogen-doped carbon nanospheres as efficient polyselenide reservoir for fast and long-life sodium-selenium batteries. *Small* **2020**, *16*, 2005534.

156. Muruganantham, R.; Liu, W. R. A venture synthesis and fabrication of $BiVO_4$ as a highly stable anode material for Na-ion batteries. *Chemistryselect* **2017**, *2*, 8187-8195.

157. Hong, W.; Ge, P.; Jiang, Y.; Yang, L.; Tian, Y.; Zou, G.; Cao, X.; Hou, H.; Ji, X. Yolk-shell-structured bismuth@n-doped carbon anode for lithium-ion battery with high volumetric capacity. *ACS Appl. Mater. Interfaces* **2019**, *11*, 10829-10840.

158. Xiong, J. Y.; Cheng, G.; Li, G. F.; Qin, F.; Chen, R. Well-crystallized square-like 2D BiOCl nanoplates: Mannitol-assisted hydrothermal synthesis and improved visible-light-driven photocatalytic performance. *RSC Adv.* **2011**, *1*, 1542-1553.

159. Xu, X.; Xu, Y.; Xu, F.; Jiang, G.; Jian, J.; Yu, H.; Zhang, E.; Shchukin, D.; Kaskel, S.; Wang, H. Black $BiVO_4$: Size tailored synthesis, rich oxygen vacancies, and sodium storage performance. *J. Mater. Chem. A* **2020**, *8*, 1636-1645.

160. Yang, Z.; Zhu, K.; Dong, Z.; Jia, D.; Jiao, L. Stabilization of Li-Se batteries by wearing PAN protective clothing. *ACS Appl. Mater. Interfaces* **2019**, *11*, 40069-40077.

161. Zhang, Y.; Guo, Y.; Wang, B.; Wei, Y.; Jing, P.; Wu, H.; Dai, Z.; Wang, M.; Zhang, Y. An integrated hybrid interlayer for polysulfides/selenides regulation toward advanced Li-SeS_2 batteries. *Carbon* **2020**, *161*, 413-422.

162. Hu, N.; Lv, X.; Dai, Y.; Fan, L.; Xiong, D.; Li, X. SnO_2/reduced graphene oxide interlayer mitigating the shuttle effect of Li-S batteries. *ACS Appl. Mater. Interfaces* **2018**, *10*, 18665-18674.

163. Wang, J.; Polleux, J.; Lim, J.; Dunn, B. Pseudocapacitive contributions to electrochemical energy storage in TiO_2 (anatase) nanoparticles. *J. Phys. Chem. C* **2007**, *111*, 14925-14931.

164. Huang, J.-Q.; Chong, W. G.; Zhang, B.; Ma, X. Advances in multi-functional flexible interlayers for Li-S batteries and metal-based batteries. *Mater. Today Commun.* **2021**, *28*, 102566.

165. Zhao-Karger, Z.; Lin, X.-M.; Bonatto Minella, C.; Wang, D.; Diemant, T.; Behm, R. J.; Fichtner, M. Selenium and selenium-sulfur cathode materials for high-energy rechargeable magnesium batteries. *J. Power Sources* **2016**, *323*, 213-219.

166. Zhang, Y.; Wang, M.; Guo, Y.; Huang, L.; Wang, B.; Wei, Y.; Jing, P.; Zhang, Y.; Zhang, Y.; Wang, Q.; et al. A natural polymer captor for immobilizing polysulfide/polyselenide in working Li-SeS_2 batteries. *Nanomicro Lett.* **2021**, *13*, 104.

167. Babu, D. B.; Ramesha, K. Constraining polyselenide formation in ether based electrolytes through confinement of Se in microporous carbon matrix for Li-Se batteries. *Electrochim. Acta* **2016**, *219*, 295-304.

168. Jain, A.; Ong, S. P.; Hautier, G.; Chen, W.; Richards, W. D.; Dacek, S.; Cholia, S.; Gunter, D.; Skinner, D.; Ceder, G.; et al. Commentary: The materials project: A materials genome approach to accelerating materials innovation. *APL Mater.* **2013**, *1*, 011002.

169. Yang, C.; Suo, L.; Borodin, O.; Wang, F.; Sun, W.; Gao, T.; Fan, X.; Hou, S.; Ma, Z.; Amine, K.; et al. Unique aqueous Li-ion/sulfur chemistry with high energy density and reversibility. *Proc. Natl. Acad. Sci. U. S. A.* **2017**, *114*, 6197-6202.

170. Li, N.; Weng, Z.; Wang, Y.; Li, F.; Cheng, H.-M.; Zhou, H. An aqueous dissolved polysulfide cathode for lithium-sulfur batteries. *Energy Environ. Sci.* **2014**, *7*, 3307-3312.

171. Placke, T.; Heckmann, A.; Schmuch, R.; Meister, P.; Beltrop, K.; Winter, M. Perspective on performance, cost, and technical challenges for practical dual-ion batteries. *Joule* **2018**, *2*, 2528-2550.

172. Feng, J. K.; Cao, Y. L.; Ai, X. P.; Yang, H. X. Polytriphenylamine: A high power and high capacity cathode material for rechargeable lithium batteries. *J. Power Sources* **2008**, *177*, 199-204.

173. Xiu, Y.; Mauri, A.; Dinda, S.; Pramudya, Y.; Ding, Z.; Diemant, T.; Sarkar, A.; Wang, L.; Li, Z.; Wenzel, W.; et al. Anion storage chemistry of organic cathodes for high-energy and high-power density divalent metal batteries. *Angew. Chem. Int. Ed.* **2022**, *62*, e202212339.

174. Liu, S.; Shu, C. Z.; Yan, Y.; Ren, L. F.; Du, D. Y.; Zeng, T.; Wen, X. J.; Xu, H. Y.; Zhao, C.; Wang, X. X.; et al. Regulating solvation environment of Li ions via high

donor number anions for high-performance Li-metal batteries. *Chem. Eng. J.* **2022**, *450*, 138369.

175. Chu, H.; Noh, H.; Kim, Y. J.; Yuk, S.; Lee, J. H.; Lee, J.; Kwack, H.; Kim, Y.; Yang, D. K.; Kim, H. T. Achieving three-dimensional lithium sulfide growth in lithium-sulfur batteries using high-donor-number anions. *Nat. Commun.* **2019**, *10*, 188.
176. Chen, J.; Peng, Y.; Yin, Y.; Fang, Z.; Cao, Y.; Wang, Y.; Dong, X.; Xia, Y. A desolvation-free sodium dual-ion chemistry for high power density and extremely low temperature. *Angew. Chem. Int. Ed.* **2021**, *60*, 23858-23862.
177. Boyer, M. I.; Quillard, S.; Rebourt, E.; Louarn, G.; Buisson, J. P.; Monkman, A.; Lefrant, S. Vibrational analysis of polyaniline: A model compound approach. *J. Phys. Chem. B* **1998**, *102*, 7382-7392.
178. Luo, Y.; Zheng, F.; Liu, L.; Lei, K.; Hou, X.; Xu, G.; Meng, H.; Shi, J.; Li, F. A high-power aqueous zinc-organic radical battery with tunable operating voltage triggered by selected anions. *ChemSusChem* **2020**, *13*, 2239-2244.
179. Petr, A.; Kvarnström, C.; Dunsch, L.; Ivaska, A. Electrochemical synthesis of electroactive polytriphenylamine. *Synth. Met.* **2000**, *108*, 245-247.
180. Sjoberg, P.; Politzer, P. Use of the electrostatic potential at the molecular-surface to interpret and predict nucleophilic processes. *J. Phys. Chem.* **1990**, *94*, 3959-3961.
181. Kvarnström, C.; Petr, A.; Damlin, P.; Lindfors, T.; Ivaska, A.; Dunsch, L. Raman and FTIR spectroscopic characterization of electrochemically synthesized poly(triphenylamine), PTPA. *J. Solid State Electrochem.* **2002**, *6*, 505-512.

182. Mazeikiene, R.; Niaura, G.; Malinauskas, A. Poly(n-methylaniline) vs. Polyaniline: An extended pH range of polaron stability as revealed by Raman spectroelectrochemistry. *Spectrochim. Acta A Mol. Biomol. Spectrosc.* **2021**, *262*, 120140.

183. Baibarac, M.; Mihut, L.; Louarn, G.; Mevellec, J. Y.; Wery, J.; Lefrant, S.; Baltog, I. Interfacial chemical effect evidenced on SERS spectra of polyaniline thin films deposited on rough metallic supports. *J. Raman Spectrosc.* **1999**, *30*, 1105-1113.

184. Bitenc, J.; Vizintin, A.; Grdadolnik, J.; Dominko, R. Tracking electrochemical reactions inside organic electrodes by operando IR spectroscopy. *Energy Storage Mater.* **2019**, *21*, 347-353.

185. Xu, S.; Dai, H.; Zhu, S.; Wu, Y.; Sun, M.; Chen, Y.; Fan, K.; Zhang, C.; Wang, C.; Hu, W. A branched dihydrophenazine-based polymer as a cathode material to achieve dual-ion batteries with high energy and power density. *eScience* **2021**, *1*, 60-68.

186. Fan, L.; Liu, Q.; Xu, Z.; Lu, B. An organic cathode for potassium dual-ion full battery. *ACS Energy Lett.* **2017**, *2*, 1614-1620.

187. Qiu, X.; Wang, N.; Dong, X.; Xu, J.; Zhou, K.; Li, W.; Wang, Y. A high-voltage Zn-organic battery using a nonflammable organic electrolyte. *Angew. Chem. Int. Ed.* **2021**, *60*, 21025-21032.

188. Hou, Z.; Zhou, R.; Yao, Y.; Min, Z.; Lu, Z.; Zhu, Y.; Tarascon, J.-M.; Zhang, B. Correlation between electrolyte chemistry and solid electrolyte interphase for reversible Ca metal anodes. *Angew. Chem. Int. Ed.* **2022**, *61*, e202214796.

189. Deng, X. M.; Sarpong, J. K.; Zhang, G. B.; Hao, J.; Zhao, X.; Li, L. Y.; Li, H. F.; Han, C. P.; Li, B. H. Proton storage chemistry in aqueous zinc-organic batteries: A review. *Infomat* **2023**, *5*, 12382.

190. Zhu, K.; Wu, T.; Sun, S.; van den Bergh, W.; Stefik, M.; Huang, K. Synergistic H^+/Zn^{2+} dual ion insertion mechanism in high-capacity and ultra-stable hydrated VO_2 cathode for aqueous Zn-ion batteries. *Energy Storage Mater.* **2020**, *29*, 60-70.

191. Tie, Z.; Liu, L.; Deng, S.; Zhao, D.; Niu, Z. Proton insertion chemistry of a zinc-organic battery. *Angew. Chem. Int. Ed.* **2020**, *59*, 4920-4924.

192. Zhang, Y.; Zhao, C.; Li, Z.; Wang, Y.; Yan, L.; Ma, J.; Wang, Y. Synergistic co-reaction of Zn^{2+} and H^+ with carbonyl groups towards stable aqueous zinc-organic batteries. *Energy Storage Mater.* **2022**, *52*, 386-394.

193. Na, M.; Oh, Y.; Byon, H. R. Effects of Zn^{2+} and H^+ association with naphthalene diimide electrodes for aqueous Zn-ion batteries. *Chem. Mater.* **2020**, *32*, 6990-6997.

194. Sun, W.; Wang, F.; Hou, S.; Yang, C.; Fan, X.; Ma, Z.; Gao, T.; Han, F.; Hu, R.; Zhu, M.; et al. Zn/MnO_2 battery chemistry with H^+ and Zn^{2+} coinsertion. *J. Am. Chem. Soc.* **2017**, *139*, 9775-9778.

195. Wang, S.; Yuan, Z.; Zhang, X.; Bi, S.; Zhou, Z.; Tian, J.; Zhang, Q.; Niu, Z. Non-metal ion co-insertion chemistry in aqueous Zn/MnO_2 batteries. *Angew. Chem. Int. Ed.* **2021**, *60*, 7056-7060.

196. Zhou, L.; Liu, L.; Hao, Z.; Yan, Z.; Yu, X.-F.; Chu, P. K.; Zhang, K.; Chen, J. Opportunities and challenges for aqueous metal-proton batteries. *Matter* **2021**, *4*, 1252-1273.

197. Liu, Z.; Li, X.; He, J.; Wang, Q.; Zhu, D.; Yan, Y.; Chen, Y. Is proton a charge carrier for δ-MnO_2 cathode in aqueous rechargeable magnesium-ion batteries? *J. Energy Chem.* **2022**, *68*, 572-579.

198. Weppner, W.; Huggins, R. A. Determination of the kinetic parameters of mixed-conducting electrodes and application to the system Li_3Sb. *J. Electrochem. Soc.* **1977**, *124*, 1569.

199. Chen, X.; Hu, X.; Chen, Y.; Cao, X.; Huang, Y.; Zhang, H.; Liu, J.-H.; Wang, Y.; Chou, S.-L.; Cao, D. Ultrastable hydrated vanadium dioxide cathodes for high-performance aqueous zinc ion batteries with H^+/Zn^{2+} co-insertion mechanism. *J. Mater. Chem. A* **2022**, *10*, 22194-22204.

200. Wang, X.; Liu, Y.; Wei, Z.; Hong, J.; Liang, H.; Song, M.; Zhou, Y.; Huang, X. Mxene-boosted imine cathodes with extended conjugated structure for aqueous zinc-ion batteries. *Adv. Mater.* **2022**, *34*, 2206812.

201. Liu, K.-Z.; Jackson, M.; Sowa, M. G.; Ju, H.; Dixon, I. M. C.; Mantsch, H. H. Modification of the extracellular matrix following myocardial infarction monitored by FTIR spectroscopy. *BBA-Mol. Basis Dis.* **1996**, *1315*, 73-77.

202. Yue, F.; Tie, Z.; Deng, S.; Wang, S.; Yang, M.; Niu, Z. An ultralow temperature aqueous battery with proton chemistry. *Angew. Chem. Int. Ed.* **2021**, *60*, 13882-13886.